TECHNISCHE UNIVERSITÄT MÜNCHEN

Aus dem Institut für interventionelle und diagnostische Radiologie

Klinikum rechts der Isar

(Direktor: Univ.-Prof. Dr. E. J. Rummeny)

Optical Imaging allows *in vivo* tracking of theranostic liposomes to ovarian cancers

Lisa Ravarani

Vollständiger Abdruck der von der Fakultät für Medizin der Technischen Universität München zur Erlangung des akademischen Grades eines Doktors der Medizin genehmigten Dissertation.

Vorsitzender: Univ.-Prof. Dr. P. Henningsen

Prüfer der Dissertation: 1. Univ.-Prof. Dr. E. J. Rummeny
                            2. Priv.-Doz. Dr. R. Meier

Die Dissertation wurde am 27.05.2013 bei der Technischen Universität München eingereicht und durch die Fakultät für Medizin am 16.10.2013 angenommen.

Meiner Familie

Table of Contents

1.   Introduction

More than 20,000 women are diagnosed with ovarian cancer each year in the United States (Jemal *et al.*, 2009). The disease is still associated with a poor prognosis and an approximate 50% 5-year survival rate, which is due to non-specific early symptoms and an often advanced stage at the time of diagnosis (Cannistra, 2004). Though aggressive surgical debulking and standard taxane- or platinum-based chemotherapy lead to an initial response in the majority of patients, most of them ultimately relapse after a certain time interval (Katsumata *et al.*, 2009). Disease progression warrants the institution of second-line chemotherapy, including chemotherapy with anthracyclines like Doxorubicin or its liposome-based formulation Doxil® (Cannistra, 2002).

Many imaging modalities are currently deployed to improve the time of diagnosis of ovarian cancer, thus potentially leading to better therapeutic premises. Ultrasound examination is the most useful noninvasive diagnostic test if an adnexal mass is suspected. It is noninvasive and radiation free but it is operator-dependent, requiring a high level of skill and experience to acquire good-quality images and make accurate diagnoses. Magnetic resonance imaging (MRI) is an excellent imaging device when an adnexal mass is indeterminate on ultrasound (Shaaban, Rezvani, 2009). MRI provides high spatial resolution and is also radiation-free but the images obtained are less sensitive than those obtained with nuclear imaging, and data acquisition is expensive and long-winded (Barentsz, 1995). Moreover, in the case of solid tumors of the abdomen, computed tomography (CT) is often preferred due to less motion artifact. CT is usually more widely available, faster, less expensive, and may be less likely to require the person to be sedated or anesthetized. Another imaging modality, namely positron emission tomography (PET) is of great benefit as a diagnostic tool in ovarian cancer when there is an increase in serum tumor marker and previously performed imaging is inconclusive or negative. The benefit of PET is of high interest in the post-operative setting as disease surveillance modality (Basu *et al.*, 2009). CT and PET-CT demonstrate a high sensitivity and potential for whole-body evaluation, however, drawbacks include radiation exposure and high costs for

both modalities and a short isotope half-life for PET-CT (Grahek, Hassan-Sebbag, 2009).

Optical Imaging (OI), a technique based on the detection of fluorescence, is a relatively new imaging modality that encompasses numerous techniques and methods and has a large range of applications, including cancer research such as monitoring tumor growth, treatment, or the proliferation of metastatic disease. For example, breast cancer patients have been scanned using optical imaging, which may supplement mammography and MRI in breast cancer detection (Ntziachristos *et al.*, 2000). Moreover, anti-cancer therapies are tested through monitoring the efficiency of chemotherapy, cytokine or immunotherapy with OI (Licha, Olbrich, 2005). Major advantages in comparison to other imaging modalities consist of its relatively inexpensive and easy and rapid image generation. Moreover, it is noninvasive, radiation-free and has molecular sensitivity (Citrin *et al.*, 2004, Sutton *et al.*, 2008). Its major limiting factors continue to be the fairly limited penetration of light through tissue due to absorption or scattering and the relatively low spatial resolution, both impeding the breadth of clinical application (Licha, Olbrich, 2005).

Second-line therapeutic agents Doxorubicin or Doxil® are characterized by their intrinsic fluorescence properties (Cay *et al.*, 1997), thus enabling them to be detected by fluorescent imaging modalities, one of them being Optical Imaging. However, their fluorescence characteristics are in an unfavorable spectrum for *in vivo* optical imaging (Bremer *et al.*, 2003). A potential approach to nevertheless visualize Doxorubicin and its liposomal derivates with optical imaging, in order to monitor their accumulation in tumor tissue, is to co-encapsulate it with a near infrared (NIR) dye into a liposomal formulation and shift the imaging spectrum to higher, more favorable wavelengths for *in vivo* Optical Imaging (Bremer *et al.*, 2003). We developed a new formulation of liposomal Doxorubicin, which had been co-encapsulated with the near-infrared (NIR) dye ADS645WS. ADS645WS can be detected with standard OI scanners and thus allow *in vivo* tracking of associated drugs.

The purpose of this study was to diagnose the *in vivo* accumulation of the newly designed liposomal ADS645WS-Doxorubicin formulation in human ovarian cancer xenografts and to gain further insight into the longitudinal monitoring of *in vivo*

cytotoxic drug behavior and treatment response with Optical Imaging. Furthermore, fluorescent signals from Optical Imaging data were correlated with the tumor morphology as determined by histopathology.

2.   Background

2.1. Ovarian Cancer

2.1.1. Epidemiology and Pathogenesis

Ovarian cancer is the second most common gynecologic malignancy in North America and Northern Europe. It is the most common cause of death among women with gynecologic cancer and the fifth leading cause of cancer death in all women. Approximately 20.000 new cases are diagnosed each year in the United States (respectively 8000 in Germany) and 14.000 (respectively 6000) ovarian cancer-related deaths occur annually (Kiechle, 2006, Jemal *et al.*, 2009). The median age of patients with ovarian cancer is 60 years, and the average lifetime risk for women is about 1 in 70 (Whittemore *et al.*, 1992).

A strong family history of ovarian cancer is related to the presence of an inherited mutation in one of two genes, known as BRCA1 and BRCA2. This genetic predisposition is the most important risk factor, but is present in only approximately 5 percent of women presenting with ovarian cancer (Hennessy *et al.*, 2008)*.* Nulliparity is associated with an increased risk, whereas a periodic suppression of ovulation due to oral contraceptive use, pregnancy or lactation is associated with a reduced risk of ovarian cancer (*Table 1: risk factors for ovarian cancer)* (Whittemore *et al*., 1992, Carlson *et al*., 1994, Gotlieb *et al*., 2000, Ness *et al.*, 2002).

Risk factors for ovarian cancer		
Risk factors	**Relative risk**	**Lifetime probability (%)***
Familial ovarian cancer syndrome	unknown	30 to 50
Two or three relatives with ovarian cancer	4.6	5.5 (if 1st degree)
One relative (1st or 2nd degree) with ovarian cancer	3.1	3.7 (if 1st degree)
No risk factors	1.0	1.8
Past oral contraceptive use	0.65	0.8
Past pregnancy	0.5	0.6
Infertility	2.8	
Nulliparity	1.6	
Past breast feeding	0.81	
Tubal ligation	0.59	
* Indicates probability for ovarian cancer in a 50-year-old woman		

Table 1: *Risk factors for ovarian cancer: taken from uptodate.com and adapted from: (Whittemore et al., 1992, Carlson et al., 1994, Gotlieb et al., 2000, Ness et al., 2002)*

The pathogenetic mechanism(s) that explain the link between many of the risk factors and development of ovarian cancer have not been determined. Some of the main hypotheses that have been proposed are:

(1) Repeated ovulation results in repeated minor trauma to the ovarian epithelium, which, in turn, can lead to malignant transformation. Support for this hypothesis is derived from the observation that women with periodic suppression of ovulation have a lower incidence of ovarian cancer (Ilekis *et al.*, 1997).

(2) Persistent ovarian exposure to gonadotropins and elevated estradiol concentrations may be carcinogenic. This hypothesis is supported by the observation that experimentally induced ovarian tumors contain gonadotropin receptors and estrogen can stimulate cell proliferation in cells containing estrogen receptors (Schildkraut *et al.*, 1996).

(3) Recently, multiple genetic and epigenetic changes have been studied and some are evident in ovarian cancer. How such changes induce tumorigenesis is not yet

clear. Many oncogenes or tumor suppressor genes and several signaling pathways have been implicated in ovarian cancer. Aberrations in cell proliferation, apoptosis and autophagy and changes in cell adhesion and motility all contribute to disease development and metastasis (Bast *et al.*, 2009). Epigenetics have become intensely integrated in research focusing on understanding the development and progression of ovarian cancer. Indeed, their gradual accumulation is associated with advancing grade and stage of disease (Balch *et al.*, 2009).

There are numerous types of ovarian tumors and it is believed that they arise ultimately from one of the three ovarian components: (1) the surface epithelium derived from the coelomic epithelium, which account for the majority of cases; (2) the germ cells, which migrate to the ovary from the yolk sac and are pluripotent; and (3) the stroma of the ovary, including the sex cords, which are forerunners of the endocrine apparatus of the postnatal ovary. There is also a group of tumors that defy classification, and finally there are secondary or metastatic tumors to the ovary (*Table 2*: *WHO classification of ovarian neoplasms)* (Scully, 1987, Kumar *et al.*, 2010).

WHO Classification of ovarian neoplasms	
Surface epithelial-stromal tumors	**Sex cord-stromal tumors**
Serous tumors	Granulosa Tumors
Benign (cystadenoma)	Fibromas
Borderline tumors (serous borderline tumor)	Fibrothecomas
Malignant (serous adenocarcinoma)	Thecomas
Mucinous tumors, endocervical-like and intestinal type	Sertoli cell tumors
Benign (cystadenoma)	Leydig cell tumors
Borderline tumors (mucinous borderline tumor)	Sex cord tumor with annular tubules
Malignant (mucinous adenocarcinoma)	Gynandroblastoma
Endometrioid tumors	Steroid (lipid) cell tumors
Benign (cystadenoma)	**Germ cell tumors**
Borderline tumors (endometrioid borderline tumor)	Teratoma
Malignant (endometrioid adenocarcinoma)	Immature
Clear cell tumors	Mature
Benign	Solid
Borderline tumors	Cystic (dermoid cyst)
Malignant (clear cell adenocarcinoma)	Monodermal (e.g. struma ovarii, carcinoid)
Transitional cell tumors	Dysgerminoma
Brenner tumor	Yolk sac tumor (endodermal sinus tumor)
Brenner tumor of borderline malignancy	Mixed germ cell tumors
Malignant Brenner tumor	**Malignant, not otherwise specified**
Transitional cell carcinoma (non-Brenner type)	**Metastatic cancer from non-ovarian primary**
Epithelial-Stromal	Colonic, appendiceal
Adenocarcinoma	Gastric
Malignant mixed müllerian tumor	Breast

***Table 2**: WHO classification of ovarian neoplasms (adapted from Robbins and Cotrane: Pathologic Basis of disease (Kumar et al., 2010))*

2.1.2. Diagnosis

The symptoms and physical findings of ovarian cancer are nonspecific and can suggest the presence of upper abdominal disease, often leading to late diagnosis and thus advanced stage of disease. Affected women may report abdominal discomfort, due to increased abdominal pressure from ascites or involvement of the omentum. Occasionally patients with early-stage disease present with pelvic pain due to ovarian torsion but most patients with early-stage disease remain asymptomatic (Cannistra, 2004, Asadollahi *et al.*, 2010)

Ultrasound examination is the most useful noninvasive diagnostic test in women with an adnexal mass. The presence of sonographic features suggestive of malignancy helps in predicting the likelihood that a pelvic mass is malignant, but is not infallible, even when combined with other modalities, such as demographic information and biochemical data (Aslam *et al.*, 2000).

Therefore, if ovarian cancer is suspected on the basis of the physical examination and the results of ultrasonography, an exploratory laparotomy for definitive histologic diagnosis is usually required (Cannistra, 2004).

2.1.3. Treatment

Treatment of epithelial ovarian cancer is determined by the stage of disease at the time of diagnosis, as expressed by the International Federation of Gynecology and Obstetrics (FIGO)/TNM staging system. The initial management in women with ovarian cancer is almost always aggressive surgical resection even when advanced staged (Goff *et al.*, 2007, Asadollahi *et al.*, 2010)*.*

The majority of patients with epithelial ovarian cancer will then require postoperative adjuvant chemotherapy in attempt to eradicate residual disease (Trimbos *et al.*, 2003, Cannistra, 2004). In patients with early-stage disease with a high risk of relapse, intravenous administration of taxane- (such as paclitaxel and docetaxel) and platinum- (such as cisplatin and carboplatin) based adjuvant treatment is commonly considered while it is the current standard of postoperative care in patients with advanced ovarian cancer (Ozols *et al.*, 2002, Katsumata *et al.*, 2009). Although initial responses to chemotherapy are often good, disease recurrence continues to be a major problem for patients with advanced staged disease. A common sign of relapse is a rise in the serum CA-125 level and abnormalities on physical examination or Computed Tomography. Disease progression warrants the institution of second-line chemotherapy. The choices of agents to be considered, which are currently under investigation include liposomal doxorubicin, topotecan, oral etoposide or vinorelbine (Cannistra, 2002, Fung-Kee-Fung *et al.*, 2007).

The outlook for patients with epithelial ovarian cancer has clearly improved over the

past decade, largely as a result of taxane- and platinum-based first-line chemotherapy, as well as an increase in options for the management of recurrent disease. In addition, it is now commonplace to recognize familial syndromes and to implement risk-reduction strategies.

2.2. Cytotoxic agents

2.2.1. Anthracyclines

Anthracyclines are among the most active antineoplastic drugs developed to date, used both in the treatment of solid cancers, such as breast and ovarian cancer or sarcomas, and of hematologic cancers and are used extensively both as single agent- and in combination regimens; in adjuvant- as well as in metastatic settings. The mechanisms of action of the entire class of anthracyclines in tumor cells remain a matter of controversy. Mechanisms that have been suggested include: (1) induction of apoptosis in response to topoisomerase II inhibition (Skladanowski, Konopa, 1993), (2) initiation of DNA damage via inhibition of topoisomerase II (Gruber *et al.*, 2005), (3) high affinity binding to DNA through intercalation, with consequent blockade of the synthesis of DNA and RNA, and DNA strand scission (Graves, Krugh, 1983), (4) binding to cellular membranes to alter fluidity and ion transport (Richardson, Johnson, 1997) and (5) generation of semiquinone free radicals and oxygen free radicals through an enzyme-mediated reductive process (Chu, Sartorelli, 2003, Abraham *et al.*, 2005, Takemura, Fujiwara, 2007).

Over the course of the past three decades, much research effort has been devoted in developing a "better anthracycline" which has resulted in the synthesis of some 2000 analogues. However, none of these agents appear to have any advantage over Doxorubicin or its liposomal formulation (Weiss, 1992, Richardson, Johnson, 1997, Takemura, Fujiwara, 2007).

2.2.1.1.   Doxorubicin

Clinical use

Doxorubicin (DOX), introduced around 1970, is the best-known and most widely used member of the anthracycline antibiotic group of anticancer agents (Abraham *et al.*, 2005). It is widely used in the treatment of acute lymphoblastic and myeloblastic leukemia, Hodgkin's and Non-Hodgkin's lymphoma (Takemura, Fujiwara, 2007) as well as in the treatment of breast and ovarian cancer (Vermorken, 2003).
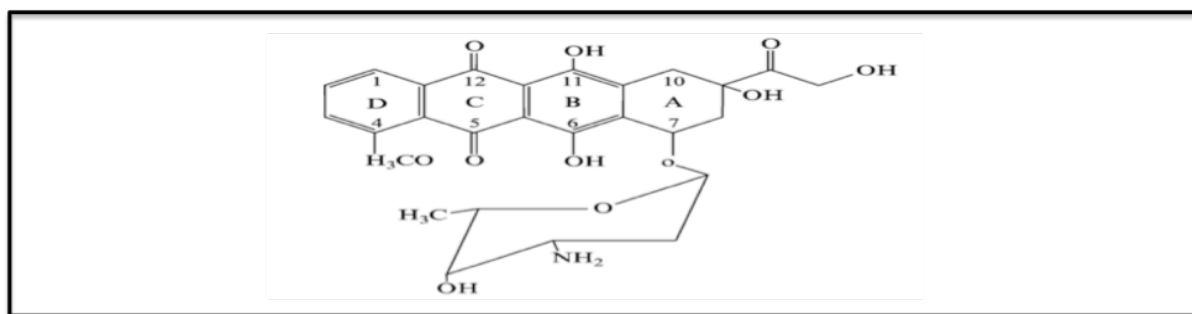
Figure 1*: Doxorubicin (taken from (Abraham et al., 2005))*

Description

Doxorubicin is a cytotoxic anthracycline antibiotic isolated from cultures of the pigment-producing *Streptomyces peucetinus* var. *caesius* (Takemura, Fujiwara, 2007) and consists of a naphtacenequinone nucleus linked through a glycoside bond at ring atom 7 to an amino sugar, daunosamine ($C_{21}H_{18}O_9$). Chemically, Doxorubicin hydrochloride is: 5,12-Naphtacenedione, 10-[(3-amino-2,3,6-trideoxy-α-L-lyxo-hexopyranosyl)oxy]-7,8,9,10-tetrahydro-6,8,11-trihydroxy-8-(hydroxylacetyl)-1-methoxy-,hydrochloride (8S-cis) (Bouma *et al.*, 1986, Fiallo *et al.*, 1998). Doxorubicin hydrochloride typically exists as a hygroscopic crystalline powder composed of orange-red thin needles. It has a melting point of 229-331°C and absorption maximums (in methanol) of 233, 252, 88, 479, 496 and 529nm due to the dihydroxyanthraquinone chromophore (Budavari, 2000). Any variation of groups on the chromophore will lead to changes in the absorption spectrum. The spectrum depends on pH, binding ions and their concentration or drug concentration (Abraham *et al.*, 2005). Doxorubicin is documented to appear orange at pH 7, violet at pH 11 and blue at pH 13 (Fiallo *et al.*, 1999). Doxorubicin has a well-documented

autofluorescence, with an excitation wavelength of 480nm and an emission cut-off of 550nm (Cay *et al.*, 1997)*.

Mechanism of action

As described above, Doxorubicin, like all anthracyclines, has a wide range of different mechanisms of action (Graves, Krugh, 1983, Skladanowski, Konopa, 1993, Richardson, Johnson, 1997, Abraham *et al.*, 2005, Gruber *et al.*, 2005, Takemura, Fujiwara, 2007).

Pharmacokinetics

The initial distribution half-life of approximately 5 minutes after intravenous injection suggests rapid tissue uptake of Doxorubicin. Binding of Doxorubicin and its major metabolite, Doxorubicinol, to plasma proteins is about 75% and is independent of plasma concentration of Doxorubicin up to 1,1µg/mL. Doxorubicin is not known to cross the blood brain barrier. Studies have been performed, where Doxorubicin or Doxorubicinol have been detected in the milk of lactating patients. The relative exposure of Doxorubicinol, i.e., the ratio between the area under the curve (AUC) of Doxorubicinol and the AUC of Doxorubicin, compared to Doxorubicin ranges between 0,4 and 0,6.

Plasma clearance is predominantly by metabolism and biliary excretion. The clearance of Doxorubicin and Doxorubicinol was reduced in patients with impaired hepatic function, leading to the necessity of reducing the administered dose according to the levels of serum bilirubin, ALT and AST. No dose adaptation is required when the patient is suffering from renal impairment (Gustafson *et al.*, 2002)*.

Toxicity

Similar to other anticancer drugs targeting proliferating cell populations, Doxorubicin affects a variety of organ systems.

Gastrointestinal and hepatic effects including nausea, vomiting and diarrhea as well as a rise in bilirubin and increase in liver transaminases have been widely reported as side-effects in clinical studies of the anthracyclines (Richardson, Johnson, 1997). Oral mucositis is also common in patients receiving anthracyclines. Doxorubicin and its major metabolite, Doxorubicinol, are excreted in detectable amounts in parotid

saliva, exposing the mucosa of the upper gastrointestinal tract to drug (Bressolle *et al.*, 1992).

The cardiovascular system shows both acute and chronic effects after Doxorubicin administration. Its, generally reversible and clinically manageable, acute effects include arrhythmias, hypotension and various electrocardiography changes, whereas the chronic changes often lead to irreversible cardiomyopathy with congestive heart failure (Takemura, Fujiwara, 2007). Doxorubicin's cardiotoxic effects are clearly related to the total administered cumulative dose, leading to congestive heart failure in 4% to 36% of treated patients at cumulative dosages ranging from 450-550mg/m^2 to over 600 mg/m^2 respectively (Abraham *et al.*, 2005, Takemura, Fujiwara, 2007). The pathogenic mechanism of Doxorubicin-induced cardiomyopathy remains unclear, but seems to be different from the mechanism underlying its anti-tumor activity. Numerous mechanisms have been proposed, suggesting oxidative stress, suppression of gene expression or apoptosis among many, which seem responsible for the cardiotoxicity. Due to the very high morbidity and mortality rate of Doxorubicin treatment, a lifelong monitoring of cardiac functions is necessary in treated patients (Abraham *et al.*, 2005, Takemura, Fujiwara, 2007).

The typical acute dose-limiting toxicity, similar to that of other antineoplastic agents is that of high myelosupression. A dose-dependent, reversible leukopenia and/or granulocytopenia (neutropenia) are the predominant manifestations of Doxorubicin's hematologic toxicity, potentially leading to neutropenic fever, infections, sepsis/septicemia, septic shock, hemorrhage and tissue hypoxia and thus requiring careful monitoring over the course of the chemotherapeutic treatment (Gabizon, 1994, Richardson, Johnson, 1997, Takemura, Fujiwara, 2007).

In addition, the occurrence of secondary leukemia (AML or MDS) after anthracycline regimens, including Doxorubicin, has been described as common especially in combination with radiotherapy or patients heavily pretreated with other cytotoxic drugs (Smith, 2003).

Dosing and administration

The most commonly used dose schedule when used as a single agent is 60 to 75 mg/m^2 as a single intravenous injection administered at 21-day intervals. The lower dosage should be given to patients with inadequate marrow reserves due to old age, or prior therapy, or neoplastic marrow infiltration. Various dose modifications due to drug interaction or medical condition of the patient are necessary. It is recommended that Doxorubicin be slowly administered into the tubing of a freely running intravenous infusion of Sodium Chloride Injection, USP, or 5% Dextrose Injection, USP.

2.2.1.2.   Doxil®/Caelyx®

Clinical use

In order to improve Doxorubicin's chemotherapeutic activity and, at the same time, reduce its toxicity profile, many research groups have put efforts into the development of a liposome formulation of Doxorubicin. Two formulations that have received clinical approval are Doxil® (United States) and Caelyx® (Canada and Europe). They are pegylated liposome formulations; formulations of Doxorubicin in poly(ethylene glycol)-coated (stealth®) liposomes with a prolonged circulation time and unique toxicity profile. They are currently approved for the treatment of AIDS-related Kaposi's sarcoma and recurrent ovarian cancer in North America and in Europe as well as for metastatic breast cancer in Europe. In addition, Doxil® is also being tested in other solid tumors and in myeloma (Gabizon, 2001, Sharpe *et al.*, 2002, Abraham *et al.*, 2005).
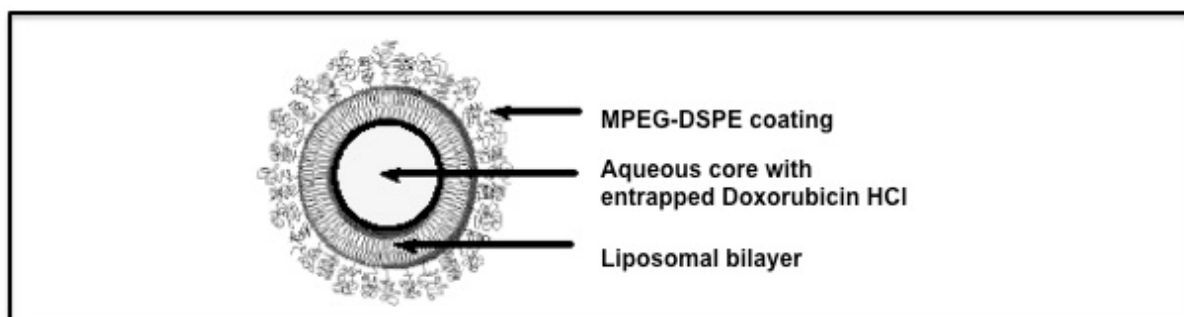

Figure 2*: Liposomal composition of STEALTH® liposome (adapted from (Abraham et al., 2005))*

Description

Doxil® consists of a liquid suspension of single lamellar vesicles with an approximate mean size of 100nm. The liposomal formulation is composed of hydrogenated soy phosphatidylcholine (HSPC), cholesterol (Chol) and N-(carbonyl-methoxypolyethylene glycol 2000)-1,2-distearoyl-sn-glycero3- phosphoethanolamine sodium salt (MPEG-DSPE) (55:40:5 molar ratio) (Working, Dayan, 1996, Gabizon *et al.*, 2003). The coating of liposomes with polyethylene glycol (PEG), a synthetic hydrophilic polymer, led to a major breakthrough in prolonging circulation time (Woodle, Lasic, 1992). These PEG-coated liposomes are referred to as sterically stabilized or STEALTH® liposomes. The total lipid content of Doxil® is approximately 16mg/mL and the Doxorubicin concentration is 2mg/mL.

Mechanism of action

Slow rates of drug release and long circulation times allow Doxil® to extravasate into diseased tissues through the "enhanced permeability and retention" or EPR effect (Hashizume *et al.*, 2000, Maeda *et al.*, 2000). Consequently, Doxil®, or liposomes with similar properties, mediate accumulation of encapsulated drugs in solid tumors, which has lead to improved therapeutic activity in comparison to free (non-encapsulated) drugs (Papahadjopoulos *et al.*, 1991, Gabizon, 1992).

Pharmacokinetics

Many variables, such as the composition of the lipid bilayer and of the liposomal water compartment, the liposome diameter, the properties of the drug, drug release rates, the nature of the interaction between the drug and the lipid vesicle compartment as well as the circulation half-life play an important role in determining the therapeutic activity and toxicity of liposomal drug delivery systems in animal models of cancer. Small diameters and long circulation half-lives allow liposomal drugs to accumulate in tissues with increased vascular permeability (e.g. tumor tissue), but only if liposomes retain their drug load over several hours to days will high drug concentrations accumulate in tumor tissue (Drummond *et al.*, 1999, Gabizon *et al.*, 2003). Due to the attachment of polyethylene-glycol polymers to a lipid anchor, the uptake by the reticulo-endothelial system is reduced. As a result, an extended circulation time and a reduced volume of distribution characterize the

pharmacokinetic profile. Analysis of tissue distribution shows increased accumulation of pegylated Doxorubicin into various implanted tumors and human tumor xenografts in comparison to the free drug (Gabizon *et al.*, 2003).

Toxicity

Compared to conventionally administered Doxorubicin, liposome formulations show reduced cardiac toxicity (Berry *et al.*, 1998, Waterhouse *et al.*, 2001). Doxil® has a low incidence of myelosuppression and its dose-limiting toxicities are mucocutaneous reactions such as stomatitis and palmar-plantar erythrodysesthesia (PPE), which develops primarily on the hands and feet and can lead to severe pain and blistering desquamation (Uziely *et al.*, 1995, Ranson *et al.*, 1997).

Dosing and administration

Doxil® should be administered intravenously at a dose of 50 mg/m2 (Doxorubicin HCl equivalent) at an initial rate of 1 mg/min to minimize the risk of infusion reactions. If no infusion-related side effects are observed, the rate of infusion can be increased to complete administration of the drug over one hour. The patient should be dosed once every 4 weeks, for as long as the patient does not progress, shows no evidence of cardiotoxicity, and continues to tolerate treatment. A minimum of 4 courses is recommended because median time to response in clinical trials was 4 months. To manage adverse events such as PPE, stomatitis, or hematologic toxicity, the doses may be delayed or reduced. Pretreatment with or concomitant use of antiemetics should be considered.

To conclude, the application of drug delivery vectors to cancer chemotherapy represents an important ongoing effort to improve the selectivity and efficacy of antineoplastic drugs. The use of liposomes as drug carriers for chemotherapeutic agents, proposed originally by Gregoriadis in 1981 (Gregoriadis, 1981), and currently under investigation by several research groups, offers a powerful means of manipulating drug distribution to improve antitumor efficacy and reduce toxicity.

2.3. Liposomal formulations

2.3.1. Liposomes and their range of clinical deployment

The pioneering observation of Alec Bangham about 40 years ago that phospholipids can form closed bilayered structures in aqueous solutions lead to the continuous development of a wide range of liposomal formulations becoming pharmaceutical carriers of choice for numerous practical applications as well as diagnostic resources in various medical fields (Torchilin, 2005). Many opportunities in a clinical environment erupt from the different therapeutic and diagnostic possibilities liposomes can offer. Different targets can be aimed at when using liposomes in a variety of therapeutic and diagnostic designs. The FDA-approval of several liposomal drugs over the past decade is a breakthrough in pharmaceutical research.

Different liposomal formulations may be used in a variety of clinical applications, such as their use as therapeutic delivery agents, as vehicles for diagnostic imaging or the combination of the two (then called theranostic liposomes).

As therapeutic drug delivery agents, liposomal drug carriers offer multiple opportunities to improve tumor therapy through various mechanisms. Liposomes may provide a slow-release vehicle to achieve pharmacokinetic characteristics increasing the therapeutic index, act as long circulating nanoparticles that can extravasate in the hyperpermeable regions of tumor vasculature or help in formulation of poorly soluble therapeutic agents, all of which will be described below (Straubinger *et al.*, 2004). For effective chemotherapy, therapeutic agents need to be selectively delivered to their target sites to assure a maximum efficacy and a reduced amount of toxicity, common to all cytotoxic drugs. In addition to drug delivery, lipid carrier systems have recently been used in gene delivery systems for gene therapy (Hashida *et al.*, 2001). Moreover, liposomal proteins may be used in various therapeutic designs. Heeremans et al. showed that a fourfold lower dose of liposomal tissue plasminogen activator was needed in rabbits with jugular vein thrombosis in comparison to those receiving the native enzyme in order to provide the same degree of lysis (Heeremans *et al.*, 1995). The encapsulation of peptides into liposomes for therapeutic reasons has been the aim of various animal studies. Thus, liposomal entrapment of insulin

purposely exploits liposomal delivery to the liver, prolongs insulin action in the body and enhances the oral absorption of insulin leading to a lasting lowering of glucose levels in animal models (Kisel *et al.*, 2001).

As diagnostic agents, liposomes have also achieved an important role, for example in Magnetic Resonance imaging (MRI), where paramagnetic liposomes have been synthesized by binding chelates such as Gadolinium-DTPA to amphiphilic moieties incorporated directly into the lipid bilayer or by directly covalently linking paramagnetic chelates to the liposome membrane surface (Unger *et al.*, 1988). These liposomes could be used in a variety of diagnostic imaging applications in the fields of neoplastic therapy tracking (Erdogan *et al.*, 2006), angiogenesis (Mulder *et al.*, 2006), blood-pool imaging (Weissig *et al.*, 2000), or cell-tracking (Bulte *et al.*, 1993).

As previously described, liposomes are used in a variety of clinical applications and experimental designs in therapeutic and diagnostic applications. The combination of these two, resulting in a theranostic liposome, a combined contrast agent and therapeutic delivery vehicle, appears to be a very promising method of treatment, therapeutic response assessment and diagnostic resource in various clinical fields. For example, an approximately linear concordance of intralesional MRI T1 measurement and tissue Doxorubicin concentration has been demonstrated following the administration of Doxorubicin and $MnSO_4$ encapsulated in thermosensitive liposomes in an *in vivo* fibrosarcoma rat model, validating the use of paramagnetic liposomes as both diagnostic imaging agent and drug delivery vehicle (Viglianti *et al.*, 2006). Moreover, another study suggested the monitoring of the delivery of Doxorubicin using Gd-DTPA-BMA encapsulated liposomes, demonstrating a significant contrast enhancement the hours following intravenous injection of the formulation in a rat osteogenic sarcoma model (Rubesova *et al.*, 2002).

2.3.2. General structure of liposomes

Liposomes are spherical vesicles formed from one or more lipid membranes composed of amphiphilic molecules such as phospholipids and cholesterol. In an aqueous solution, these amphiphiles spontaneously align to form bilayered

membranes with the hydrophilic ends positioned at the membrane surfaces and the hydrophobic ends directed internally. Liposomes usually have an aqueous phase core that may be exploited to carry and protect hydrophilic imaging agents or drugs. Likewise, hydrophobic drugs or imaging agents can be directly incorporated into the lipid membrane of the liposome. Liposomes are usually formed using phospholipids with mixed lipid chains, from pure components such as dioleolyphosphatidylethanolamine, or some combination of the two (Ulrich, 2002).

2.3.3. Pharmacokinetics and biodistribution

The properties that determine the clearance and drug retention of liposomal formulations have continued to be understood, making it possible to engineer liposomal drugs with more advanced and rational strategies to develop therapeutics with activities that are optimal for both the encapsulated agent and its specific therapeutic application. The vast wealth of knowledge regarding the biophysical and pharmacological properties of liposomal carrier systems results in them being one of the most mature and well understood drug delivery systems (Drummond *et al.*, 2008). There is a wide range of factors, which will influence the pharmacokinetics and biodistribution of liposomal formulations. The clearance of a liposome-associated drug from the blood is dependent on a) the rate of clearance of the liposomal carrier, b) the rate of dissociation of the drug from its liposomal carrier and c) the rate of clearance and metabolism of the free drug upon its release.

2.3.3.1. Pharmacokinetics and biodistribution of the liposomal carrier

Many variables affect this balance, such as the membrane composition and charge of the liposome, the particle size, the ligand-conjugation in targeted formulations or the drug to be encapsulated. Moreover, the dose, the dosing schedule and the route of administration may all vary the pharmacokinetics of the liposomal carrier. For example, the inclusion of cholesterol results in a decreased binding of plasma opsonins responsible for rapid clearance from the circulation, through stabilization of the liposomal phospholipid membranes (Chobanian *et al.*, 1979). Fluidity of the membrane also plays an important role. Thus, liposomes containing saturated phospholipids displayed a longer circulation time in comparison to unsaturated ones.

Hydrogenated sphingomyelin and cholesterol were shown to improve the circulation time for both the nanocarrier an its encapsulated drug (Johnston *et al.*, 2007). Pegylated liposomes represent an important advance in liposome technology, significantly increasing the variety of lipid compositions in the construction of liposomes, thus allowing for a wider range of drugs to be encapsulated, according to their various characteristics (Drummond *et al.*, 1999). They seem to display less heterogeneity in their pharmacokinetic parameters compared to non-pegylated liposomes (Mross *et al.*, 2004).

Charged lipids also affect liposomal clearance, which is generally increased by high concentrations of either cationic or anionic lipids into the liposomal membrane. Anionic lipids lead to an increased accumulation of liposomes in the liver or the spleen (Drummond *et al.*, 1999), while cationic lipids enhance the uptake in angiogenic blood vessels supporting tumors or in the blood brain barrier (Campbell *et al.*, 2002). Poorly designed cationic liposomes may be very polymorphic and aggregate rapidly in the serum, thus leading to accumulation in the capillaries of the lung (McLean *et al.*, 1997). Charge will also play a role in the stability of the encapsulation of various therapeutic agents.

The role of the particle size in liposomes is well studied. Generally the clearance rate will increase with the increasing size of a liposomal carrier. Liposomes of approximately 100-120nm demonstrate optimum accumulation in many solid tumors (Drummond *et al.*, 2008). Liposomes smaller in size (40-80nm) may show longer circulation times and an increased ability to extravasate, thus allowing a better accumulation in solid tumors. But due to higher clearance from the tumor as well, they seem to be less efficient in therapeutic designs (Drummond *et al.*, 1999, Allen *et al.*, 2006). Moreover, they are inherently instable and accumulate to a higher extent in hepatocytes (Litzinger *et al.*, 1994).

To increase the liposomal-, and consequently the entrapped drug accumulation in the desired tissues and organs, the use of targeted liposomes with surface-attached ligands (such as the use of Fab's or scFvs on the liposome surface in immunoliposomes), capable of recognizing and binding to cells of interest has been suggested in numerous studies (Noble *et al.*, 2004, Sapra *et al.*, 2005).

2.3.3.2. Pharmacokinetics and biodistribution of the liposomal carrier and its encapsulated drug

The efficiency by which the encapsulated drug is retained within - and subsequently released from its liposomal carrier exercises a great effect on the resulting pharmacokinetics. The rate of *in vivo* drug release influences the clearance from the blood, the biodistribution and thus the activity of the drug at its site of action and its observed toxicities (Allen *et al.*, 2006).

Therapeutic agents usually incorporated into liposomal carriers can grossly be divided into five groups: (1) water insoluble hydrophobic drugs, (2) amphiphatic weak bases, (3) amphiphatic weak acids, (4) highly water and membrane impermeable small molecular weight drugs and (5) polyions such as nucleic acids (Drummond *et al.*, 2008). The most commonly studied and easily engineered group is that of the amphiphatic weak bases, including many of the campothecins, vinca alkaloids and the anthracyline group. Even within a given class of drugs, pharmacokinetic values may vary greatly. Thus, Vincristine, Vinorelbine or Vinblastine, all members of the vinca alkaloids, display very different release rates *in vitro* and *in vivo* (Zhigaltsev *et al.*, 2005).

Drug encapsulation methods are important in determining the *in vivo* stability of the different formulations. There is a wide range of incorporation methods varying from passive integration to gradient-controlled active loading. The most widely used technique employs transmembrane gradients and trapping agents to efficiently load and subsequently stabilize therapeutic agents in the liposomal lumen (Lasic *et al.*, 1995).

It is generally assumed that encapsulation and delivery of liposomal formulations result in site-specific delivery of the therapeutic agent to the site of disease. Indeed, drugs retained in long circulating nanocarriers benefit from site-specific accumulation in the pathological sites such as tumors due to a discontinuous or otherwise more permeable microvasculature and a nonfunctioning lymphatic system. This "enhanced permeability and retention" effect will, as described earlier, lead to an altered

biodistribution for the nanocarrier-associated drug accumulating at the site of disease, and a lower concentration accumulating in healthy tissues at potential sites of toxicity (Torchilin, 2005, Drummond *et al.*, 2008).

2.3.4. Different liposomal formulations

Many different cytotoxic drugs are used for encapsulation in liposomal carriers. Vincristine was tested for antitumor efficacy in a human mammary tumor model and proved increasing antitumor activity at first but was less active in its highly stable formulation (Johnston *et al.*, 2006). Moreover, Cisplatin, a hydrophilic drug with low membrane permeability was encapsulated into a liposome using direct entrapment methods. Unfortunately, its release from the liposome was so slow that no therapeutic efficiency could be demonstrated (Zamboni *et al.*, 2004). Drummond et al. have reported a new loading technique to encapsulate Irinotecan (CPT-11) with unprecedented drug loading efficiency and *in vivo* drug retention (Drummond *et al.*, 2006). Finally pegylated Doxorubicin (Doxil®) is a liposomal formulation approved by the FDA for treatment of Kaposi sarcoma or ovarian cancer (Gabizon, 2001).

Recently, triggered delivery of liposomal therapeutics, either through a stimulus-induced increase in delivery of the liposomal carrier itself to the target site or as a result of increased drug release from the carrier has become an important point of interest for numerous studies (Drummond *et al.*, 2008). As described above, ligand targeted liposomes, such as immunoliposomes allow for promising results in cancer studies (Mamot *et al.*, 2005). Thermosensitive liposomes have been investigated in connection with Doxorubicin. As the liposomal carrier enters the locally heated tumor, Doxorubicin is rapidly released intravascular when exposed to mild hyperthermia (39-42°C), exposing the tumor tissue to very high concentrations of drug (Needham, Dewhirst, 2001). Finally, various studies target the metabolic milieu of cancerous tissue. pH-sensitive lipids are integrated into the liposomal membrane, leading to its destabilization and release of its contents once in a mildly acidic environment of solid tumors (Yatvin *et al.*, 1980).

Due to their composition and size, liposomal carriers are versatile vehicles for both diagnostic and therapeutic agent delivery. They are readily modified to alter

membrane stability and to impart additional characteristics such as thermal or pH sensitivity. In addition, surface modification with peptides or antibodies can impart selective cell targeting useful for both diagnostic imaging and drug or gene delivery. Proven increased efficacy and safety of liposome encapsulated chemotherapeutic agents such as Doxorubicin suggests a role for combined, thernanostic liposomal agents, that can be used for diagnosis, staging, therapy and response assessment.

2.4. The Enhanced Permeability and Retention effect (EPR-effect)

Most solid tumors possess unique pathophysiological characteristics that are not observed in normal tissues or organs. Extensive angiogenesis and hence hypervasculature, leading to a defective - "leaky" - vascular architecture initiated by the tumor cells to enable a rapid tumor growth, was first described by Maeda et al. (Matsumura, Maeda, 1986). In addition to the disorganised tumour vasculature and the abnormally large fenestrations in the endothelium, tumor tissue features an impaired lymphatic system with a decreased lymphatic clearance (Jain, 1994). Moreover, tumor cells seem to produce a significantly increased number of permeability mediators to sustain an adequate supply of nutrients and oxygen for rapid tumor growth (Lopez-Davila *et al.*, 2012). This phenomenon is known as the enhanced permeability and retention (EPR) effect. When designing a nanocarrier, the above-mentioned properties promote the accumulation of the carrier and its contents in solid tumor tissues rather than normal tissues, leading to an improved efficacy/toxicity profile in comparison to the free contents (Torchilin, 2007).
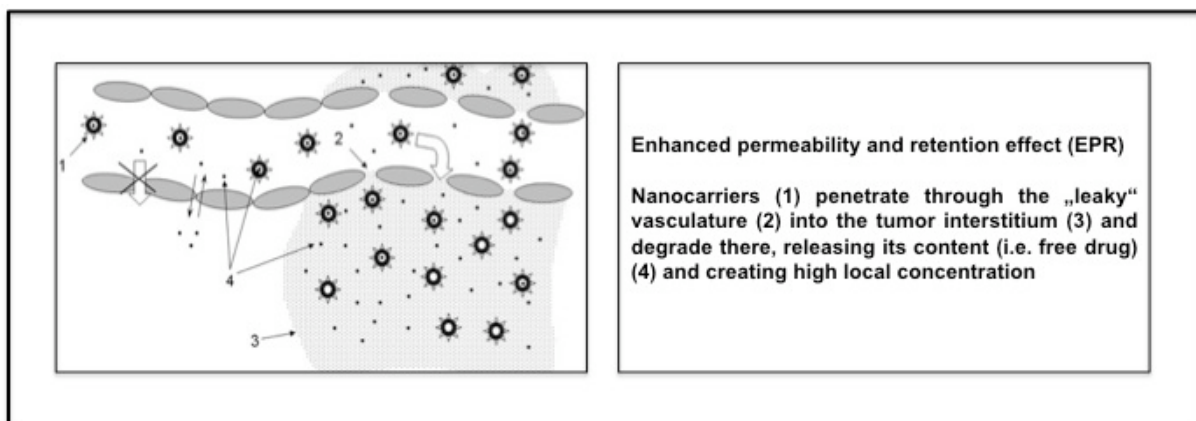

Enhanced permeability and retention effect (EPR)

Nanocarriers (1) penetrate through the „leaky" vasculature (2) into the tumor interstitium (3) and degrade there, releasing its content (i.e. free drug) (4) and creating high local concentration

Figure 3: *Enhanced permeability and retention effect (adapted from (Torchilin, 2007))*

2.5. Optical Imaging

2.5.1. Physical principles

Light is a form of energy that results from excitation of electrons and comes in units called "photons". There are different ways to excite electrons. Examples of light include generation through thermal energy (sunlight or electric light bulbs), through chemical reaction such as bioluminescence (fireflies or jellyfish) or through light itself, which can excite electrons, leading to the generation of fluorescence. The visible spectrum of photon wavelengths ranges from 400nm (violet) to 700nm (red). Light exists at wavelengths above (infrared) and below (ultraviolet) the visible spectrum, but the human eye is unable to see those wavelengths (Hassan, Klaunberg, 2004).

The typical techniques of Optical Imaging widely performed today are bioluminescence and fluorescence imaging (Choy *et al.*, 2003).

Bioluminescence is the generation of light through an enzymatic reaction. The reaction in which luciferase oxidizes its substrate, luciferin, in the presence of ATP and oxygen, is associated with the emission of a photon (emission spectra: 400–620 nm). Bioluminescent imaging is a technique to evaluate genetically modified cells that perform this enzymatic reaction. Different luciferase genes have been isolated from various organisms such as fireflies or jellyfish. The bioluminescent reaction leading to light emission does not require exogenous light sources, making for the biggest difference in comparison to fluorescent signal generation (Choy *et al.*, 2003, Citrin, Camphausen, 2004).

In fluorescence imaging, the tissue of interest is illuminated with an excitation frequency of light that results in the emission of photons from intrinsic or extrinsic probes within the tissue. When a fluorescence molecule (fluorophore) absorbs a photon, electrons in its outer shell are excited and lifted from the ground state to an excited state (S1'). Electrons rapidly relax to the lowest vibrational, thermally equilibrated excited level (S1). This process, which is called internal conversion, is usually complete prior to emission. Upon return to the initial ground state (S0) they

release energy, which is detected as fluorescence (Hassan, Klaunberg, 2004, Weisser, 2004, Lakowicz, 2010).

The emitted photon has less energy and consequently a longer wavelength than the initially absorbed photon, leading to a color shift. Planck's constant determines the wavelength of the released photon, which depends on the energy released by an electron as it returns to its ground state. The difference between the absorbed and emitted wavelength is called Stokes shift (Hassan, Klaunberg, 2004).
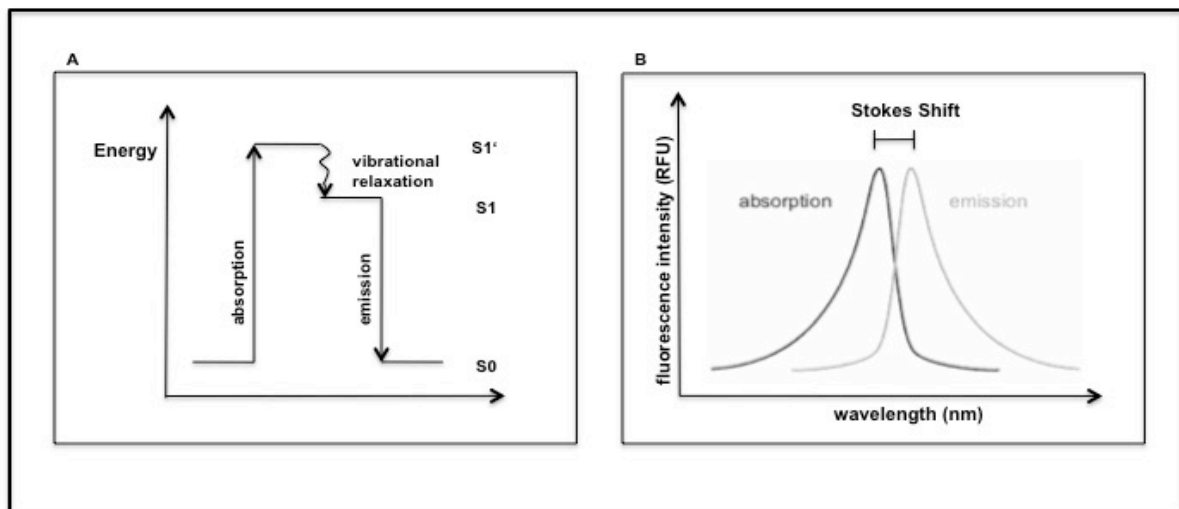

Figure 4: *(A) fluorescent principle for Optical Imaging (adapted from (Weisser, 2004)); (B) Stokes shift in fluorescent imaging (adapted from (Lakowicz, 2010)) (x-axis: wavelength (nm); y-axis: fluorescence intensity (RFU))*

The basic principle of OI involves a similar technique to that underlying the acquisition of a "photograph," thus employing an external light source that excites a fluorescent molecule (fluorophore) and a detector, which captures the molecule's emission as it is resolved by an appropriate filter (Hassan, Klaunberg, 2004, Sutton *et al.*, 2008).

The excitation light source is usually a monochromatic laser. Lasers deliver excitation light at high intensities and offer a narrow, well-defined and adjustable light source at various wavelength bandwidths ranging from the deep red to near-infrared spectral windows (Ntziachristos *et al.*, 2003, Sutton *et al.*, 2008). Using a fiber-optic bundle, the laser output is delivered to a filter wheel assembly (Rice *et al.*, 2001).

Filter selection depends on the type of imaging to be performed and requires careful selection to block out undesired wavelengths of light while maximizing detected signal from the fluorophore of interest (Choy *et al.*, 2003).

The hallmark of an optical imaging system is the cooled back-thinned and back-illuminated integrating charge-coupled device (CCD) camera. CCD cameras offer high quantum efficiency, low noise levels and high spatial resolution (Choy G et al, 2003). CCD cameras consist of thin silicon crystals sheets. These silicon-based cameras have a high sensitivity to light, thus allowing them to detect light in the visible to near-infrared range. CCD cameras convert photons at wavelengths between 400 and 1000 nm that strike a CCD pixel with energy of just 2–3 eV into electrons. The CCD chip (1024 x 1024 pixel) is very temperature sensitive, through cooling the CCD to -90°C, dark current as source of noise is reduced to insignificant levels (Choy *et al.*, 2003, Massoud, Gambhir, 2003).

A fluorophore is a naturally occurring or specially designed molecule. Fluorophores for OI should ideally fulfill some criteria in order to be suitable for *in vivo* optical imaging diagnostics. A desirable contrast agent is one that is small in size, exudes a bright signal (dependent upon the quantum yield and extinction coefficient), maintains photostability, possesses pH insensitivity, has a low background signal with prominent contrast-to-noise enhancement, should not dilute with cell division nor transfer to other cells and enables long-term cell tracking (long circulating half-life). The agent should be biocompatible and possess a tolerable toxicity profile (Sutton *et al.*, 2008; Bremer *et al.*, 2003).

The number of available fluorescent agents is very broad and can grossly be divided into endogenous (intrinsic) and exogenous (extrinsic) probes. Two common intrinsic fluorescent probes are green fluorescent protein (GFP) and red fluorescent protein (DsRed). The domain of exogenous fluorescent probes encompasses both organic an inorganic hybrids comprising fluorescent dyes, colloidal quantum dots (inorganic fluorophores comprised of colloidal semiconductor cores surrounded by chemical coating) or bifunctional labels (which can be detected by two imaging modalities). The fluorescent dyes can further be subdivided into targeted and non-targeted

fluorochromes. For the targeted fluorophores, there are simple targeting-, cross-linking- or enzyme activable "smart" probes (Weissleder *et al.*, 1999, Tung, 2004).

The non-targeted probes comprise hundreds of commercially available near-infrared fluorochromes. Compared to GFP or DsRed (which emit at wavelengths below or close to 600nm), fluorophores based on NIR dyes (emission wavelengths 650-700nm) can traverse tissue very efficiently as the absorption by water and hemoglobin is relatively low ("diagnostic window"). As light travels through tissue, photons interact with organelles by absorption and scattering. Especially signals below 600nm are highly attenuated via absorption by hemoglobin, which absorbs light in the blue-green region of the spectrum. Scatter is the reflection of light due to various components of tissue, changing the linear path of propagating light within tissue (Bremer *et al.*, 2003, Choy *et al.*, 2003). Additionally, tissue is characterized by autofluorescence since low amounts of fluorophores, which absorb light and emit signals at higher wavelengths, are present in all tissues (flavins, collagen or elastin are known fluorophores) (Bremer *et al.*, 2003). Thus, as depth penetration at lower wavelengths is a major limiting factor for *in vivo* imaging, ideal fluorophores should emit at wavelengths in this "diagnostic window" where interference signals are lowest. Cyanine dyes represent one of the most prominent categories of optical imaging agents, due to high extinction coefficients with the desired absorption and emission ranges throughout the visible to the NIR-range. Cyanine 5.5 (Cy5.5) or Indocyanine green (ICG) are prominent examples of such non-specific NIR fluorochromes, which have been subject to intense research endeavors over the past years (Licha *et al.*, 2000, Bornhop *et al.*, 2001).

2.5.2. ADS Near-infrared dyes

ADS645WS ($C_{33}H_{41}N_2O_6S_2Na$) (American Dye Source Inc., Québec, CA) is a non-targeted, hydrophilic, anionic, cyanine laser dye with a molecular weight of 648,82g/mol and excitation/emission maximums of 641/661 nm respectively (American Dye Source Product Information).
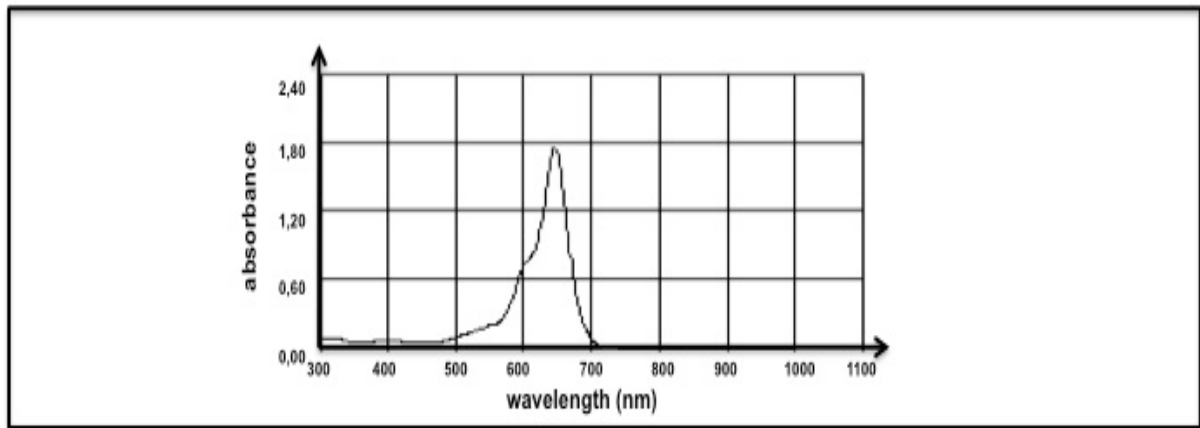
Figure 5: *Absorption spectrum of ADS645WS: $C_{33}H_{41}N_2O_6S_2Na$ (American Dye Source Inc., Laser dyes; Product Information)*

2.5.3. Applications of Optical Imaging in Cancer research

Optical Imaging encompasses numerous techniques and methods and has a large range of applications. Major advantages in comparison to other imaging modalities consist of its relatively inexpensive and rapid image generation. Moreover, it is noninvasive, has molecular sensitivity and relinquishes from ionizing radiation (Citrin, Camphausen, 2004, Sutton *et al.*, 2008).

The major limiting factors are the physical properties of imaged structures that continue to affect the penetration of light through absorption or scattering. Thus, the resulting fluorescent signals are dependent on the proximity of the contrast agent to the surface and the deployment of the "diagnostic imaging window" in the near-infrared spectrum (Licha, Olbrich, 2005).

New technological advances are helping to overcome the above-described limitations, allowing for better signal-to-noise ratio or improvement of the data produced.

There are numerous applications of OI in cancer research such as monitoring tumor growth, treatment, or the proliferation of metastatic disease. Numerous studies have demonstrated the capability to non-invasively monitor tumor cell proliferation in various animal models (Edinger *et al.*, 1999, Sweeney *et al.*, 1999) or tested anti-cancer therapies through monitoring the efficiency of chemotherapy, cytokine or

immunotherapy (Licha, Olbrich, 2005). Drug trafficking and kinetics have also been studied through the *in vivo* observation of the anti-angiogenic peptide endostatin, conjugated with Cy5.5, which was injected into tumor bearing mice (Citrin *et al.*, 2004). Moreover, a study lead by Bremer et al. showed that different proteases, such as matrix-metalloproteinases (involved in enzymatic cascades yielding to digest extracellular matrix and facilitate metastatic cell spread) can be visualized by using "smart" enzyme-activable probes (Bremer *et al.*, 2001).

These new methods improve the technique that is OI and may lead to the use of *in vivo* fluorescence imaging for example in surgical biopsy. Real-time intraoperative imaging systems displaying both anatomy (color video image) and functional tissue behavior (with NIR fluorescence) imaging have been tested (Nakayama *et al.*, 2002). Moreover, a combination of endoscopic or laparoscopic devices with optical fibers for fluorochrome detection *in vivo* may be envisioned for gastroenterological clinical practice (Costamagna, Marchese, 2010, Wallace, Kiesslich, 2010). In addition, new imaging devices allow for the study of fluorescence lifetime in response to metabolic conditions, which may lead to early tumor detection since the metabolic parameters of tumor tissue differ from those of healthy tissue (Hassan, Klaunberg, 2004, Zhang *et al.*, 2010).

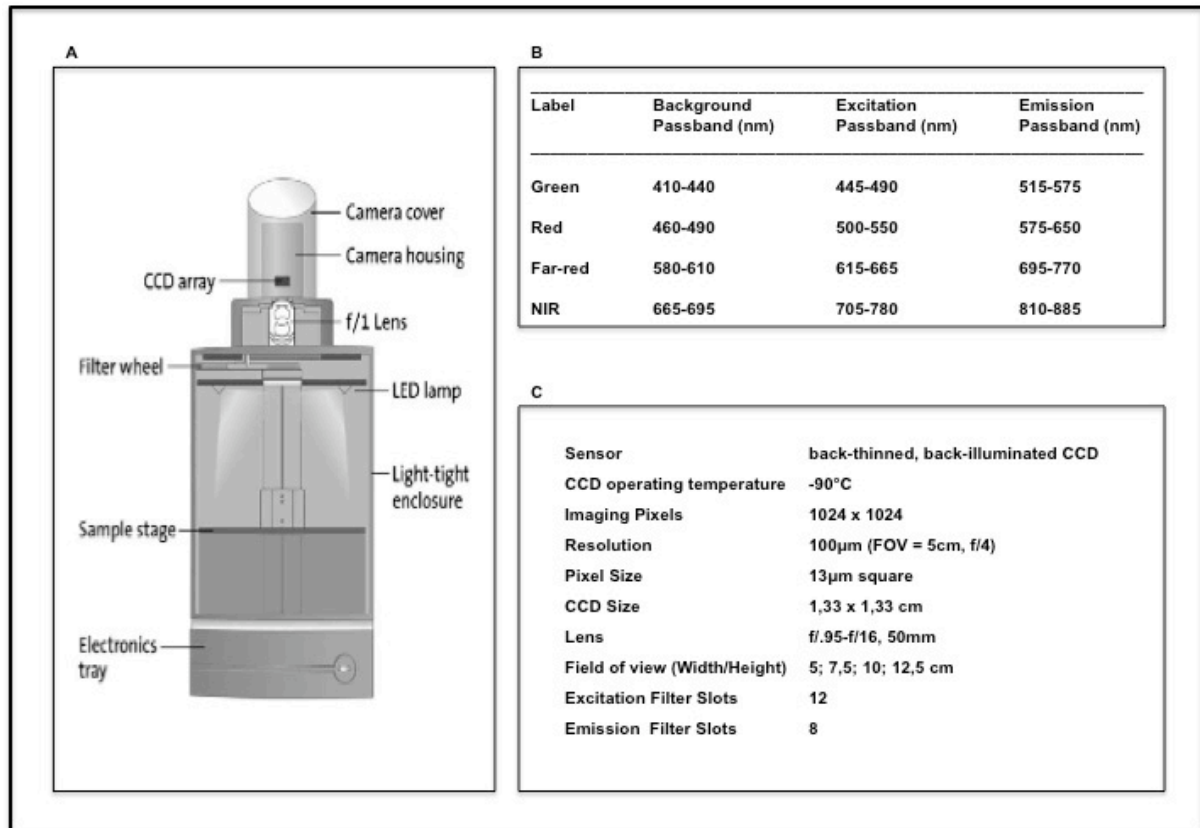## 2.5.4. Specifications for the IVIS^{TM} 50 (Lumina) imaging system

A

B

Label	Background Passband (nm)	Excitation Passband (nm)	Emission Passband (nm)
Green	410-440	445-490	515-575
Red	460-490	500-550	575-650
Far-red	580-610	615-665	695-770
NIR	665-695	705-780	810-885

C

Sensor	back-thinned, back-illuminated CCD
CCD operating temperature	-90°C
Imaging Pixels	1024 x 1024
Resolution	100µm (FOV = 5cm, f/4)
Pixel Size	13µm square
CCD Size	1,33 x 1,33 cm
Lens	f/.95-f/16, 50mm
Field of view (Width/Height)	5; 7,5; 10; 12,5 cm
Excitation Filter Slots	12
Emission Filter Slots	8

Figure 6: *(A) An illustration of the Xenogen IVIS^{TM} 50 (Lumina) Optical Imaging system used in the experimental setup; (B) Standard fluorescent filter sets; (C) Imaging system component specifications (all adapted from Xenogen Product Information, Alameda, CA, USA)*

The CCD camera, filter wheel and excitation light source are mounted to a light-tight chamber. Light is collected from the specimen and imaged onto the CCD. The sample stage may be moved to vary the field of view (FOV). The sample stage, lens focus, f/stop and filter wheel are motor controlled through Xenogen's Living Image® software. Light emitting diodes (LEDs) are located on the top plate to illuminate the specimen for photographic images. Additional features include a gas anesthesia system and a heat sample shelf to help maintain an animal's body heat during the imaging process (Rice *et al.*, 2001).

3. Materials and Methods

3.1. *In vitro* experiments

3.1.1. Spectrophotometry: data acquisition

3.1.1.1. Spectrophotometry of Doxorubicin and Doxil®

For the preliminary fluorescence characterizations of Doxorubicin, which has a well-documented intrinsic fluorescence (Cay *et al.*, 1997) and Doxil®, Spectrophotometry (Molecular Device Spectro Max Fluorescence Plate Reader and Spectro Pro 5.0.1 software) is used to confirm the excitation and emission profiles of the two cytotoxic drugs.

Doxorubicin, a standard FDA-approved cytotoxic agent is obtained as a stock solution with a concentration of 2mg/mL Doxorubicin hydrochloride diluted in 0,9% sodium chloride (Ben Venue Laboratories-Novation, Bedford, OH, USA). It has a molecular mass (Mm) of 543,52g/mol and a molarity (M) of $3,68 \times 10^{-3}$mol/L (~$3,70 \times 10^{-3}$mol/L). A dilution series is obtained starting at a molarity of 80µM and is subsequently diluted with 10% PBS to 40µM, 20µM, 10µM, 5µM, 2,5µM, 1,25µM and a control series of 0µM.

Pegylated liposomal Doxorubicin, a new, recently FDA-approved cytotoxic drug, is also obtained as a stock solution at a concentration of 2mg/mL (Doxil®, Ben Venue Laboratories, Bedford, OH). The stock solution of Doxil® has an approximate molarity of $3,70 \times 10^{-3}$mol/L as determined by Beer's law (Absorption(Abs) = extinction coefficient(ε) x concentration(c) x length(l)). Again, a dilution series is obtained starting at a molarity of 80µM and is subsequently diluted with 10% PBS to 40µM, 20µM, 10µM, 5µM, 2,5µM, 1,25µM and a control series of 0µM.

3.1.1.2. Spectrophotometry of ADS-Liposomal dyes

Three different near-infrared dyes (American Dye Source, Inc. Quebec, CA), namely ADS645WS (Mm 648,82g/mol), ADS780WS (Mm 667,12g/mol) and ADS780NH$_2$ (Mm 1089g/mol), which have been encapsulated to form a liposomal formulation (ADS645WS-Ls, ADS780WS-Ls and ADS780NH$_2$-Ls), are kindly provided by Hermes Biosciences Inc. (South San Francisco, CA). The liposomal dyes are analyzed by Spectrophotometry (U-2800 Spectrophotometer, Hitachi High Technologies America, San Jose, CA, USA). A wavelength scan with a starting wavelength of 900nm and an ending wavelength of 360nm is performed. The scan speed is determined at 100nm/min; the sampling interval is 1nm, the slit width 1,5nm and the path length (l) 10mm. These settings are kept throughout the entire experiments.

For ADS645WS-Ls, a 20µL solution is diluted in 1010µL of 10% Triton-X-100; a surfactant used to break up the liposomal formulation and release the dye's fluorescence for spectrophotometric analysis (Largueze *et al.*, 2010). 10µL of ADS780WS-Ls and 50µL of ADS780NH$_2$-Ls are diluted in 1000µL of 10% Triton-X-100 respectively.

3.1.2. Optical Imaging: data acquisition

The Optical Imager IVIS 50 (IVIS 50 Imaging system Xenogen, Alameda, CA, USA) is used throughout all the imaging procedures. The following steps have arbitrarily been chosen and need to be followed closely to guarantee accurate image acquisition for all experiments:

The *IVIS Living Image software* is started on the computer connected to the IVIS 50. The *initialize IVIS system* shows if the CCD has cooled down accurately and reached an adequate temperature for imaging purposes. The *sequential mode* (if a sequential image is wanted) is selected, as well as the camera settings for the image using the software's control panel, adjusting the following: the *exposure time* is determined confirming that the signal of interest is below the CCD saturation, the *binning* is set at medium (4), *f-stop* at 2, an *overlay* image (meaning that a photographic image is directly followed by a fluorescent image, creating an overlay of the two images) is

obtained, *FOV* is set at D=12cmx12cm and the approximate subject height determined. Then, the required filter sets are chosen for the acquisition of image one and two in the sequential mode.

For *in vitro* imaging, black polystyrene 96 well plates are used to reduce the autofluorescence of the material to a minimum amount. In the first step of the Optical Imaging of the various cytotoxic drugs or liposomal formulations, only the empty black polystyrene 96 well plate, centered exactly in the middle under the CCD camera, is imaged. This is needed for image correction later on in the experiments *(Xenogen, Living Image Software Manual, Version 2.50, 2004, p.127)*.

3.1.2.1.   Optical Imaging of Doxorubicin and Doxil®

To determine the fluorescence characteristics of Doxorubicin and Doxil® in the Optical Imager, a triplicate dilution series is obtained. For Doxorubicin, the initial concentration is ~3700µM (3680µM), followed by dilution steps to a concentration of 1000µM, 500µM, 100µM, 50µM, 25µM, 12,5µM and a control of 0µM using 10% PBS as diluting agent. The same procedure is used for the dilution series of Doxil®.

3x8 wells, containing 200µL of the different concentrations of Doxorubicin and Doxil® are pipetted on the plates. These dilution triplicates are imaged using different filter set combinations for data gathering. Five settings are chosen to analyze the characteristics of fluorescent imaging of Doxorubicin and Doxil® with Optical Imaging. For the first three combinations, single sequence images without background subtraction are obtained; the different filter sets being GFP as excitation and emission filter, DsRed as excitation and emission filter and GFP as excitation and DsRed as emission filter for the third imaging. The last two settings are sequential images, using the background filter (bkg) in addition to the excitation and emission filters for potential autofluorescence subtraction in further image analyses. The two sequential combinations used include the following filter set combinations: DsRed for excitation and emission- as well as DsRed bkg/DsRed as background filter. The second image is obtained with GFP as excitation filter, DsRed for the emission capture and GFP bkg/GFP as background filter. The exposure time is set at 1,5sec in

all five settings. Image analysis is performed as described under 3.4.1. Optical Imaging: *in vitro* data analysis.

3.1.2.2. Optical Imaging of ADS and ADS-Liposomal Near-Infrared-dyes

To determine the fluorescence characteristics of the NIR dyes and their liposomal formulations in the Optical Imager, triplicate dilution series (3x8 wells of 200µL of the respective dye) in black polystyrene 96 well plates are obtained. For ADS645WS, the initial concentration is 2500µM, followed by dilution steps to a concentration of 1000µM, 500µM, 100µM, 50µM, 25µM, 12,5µM and a control of 0µM using 10% PBS as diluting agent. For the ADS645WS-Ls solution, the initial dye based concentration is ~100µM (97,5µM), followed by dilution steps to concentrations of 50µM, 25µM, 12,5µM, 6,25µM, 3,125µM, 1,5625µM and a control concentration of 0µM. ADS780WS-Ls is at an initial concentration of ~1900µM (1942µM) and further diluted to concentrations of 1000µM, 500µM, 100µM, 50µM, 25µM, 12,5µM and a control of 0µM. The sample concentration for ADS780NH$_2$-Ls is ~100µM (175µM); it is diluted to concentrations of 50µM, 25µM, 12,5µM, 6,25µM, 3,125µM, 1,5625µM and a control of 0µM. For all the liposomal dyes dilution series', 10% PBS as well as 10% Triton-X-100 is used as diluting agent.

According to the excitation and emission wavelengths of the different dyes used, the corresponding filter sets are chosen. For ADS645WS and ADS645WS-Ls, the Cy5.5 filter set meets the imaging requirements whereas ICG is the filter set chosen for ADS780WS-Ls as well as for ADS780NH$_2$-Ls data acquisition.

For the experiments in the IVIS 50, different settings are tried out to determine the characteristics of the dye best suited for further imaging. In a first approach, an imaging series of the ADS645WS dye diluted in PBS is acquired. Cy5.5 is used as a filter set for excitation, emission and background filters. The exposure time is set at 0,5sec, 1sec and 2sec respectively. Another image is acquired with the Cy5.5 filter set, this time using only the excitation and emission set without the use of the background filter. The exposure time for this image is set at 2sec, according to the time for the *in vivo* experiments.

Continuing with the Cy5.5 filter set, using the excitation, emission and background filters; the liposomal formulation of ADS645WS, ADS645WS-Ls is imaged. Here, as described above, two different dilution series, one with PBS, the other one with Triton-X 100 are analyzed. For the PBS series, exposure times of 0,5sec and 2sec are obtained, for the Triton-X 100 series the exposure time is limited to 0,5sec since bleaching occurs at higher exposures due to high values of fluorescence and therefore image saturation *(Xenogen, Living Image Software Manual, Version 2.50, 2004, p.82)*.

The same sequence of imaging is obtained for ADS780WS-Ls and ADS780NH$_2$-Ls, using the ICG filter set for these dyes; including the excitation, emission and background filters. The dyes are divided into two dilution series each, one being PBS the other one Triton-X 100 as previously described. For the PBS series, an exposure time of 2sec is chosen, in contrary to this, a maximum exposure time of 0,5sec is tolerated for the dilution series containing Triton-X 100, again, due to image saturation. Image analysis is performed as described under 3.4.1. Optical Imaging: *in vitro* data analysis.

3.1.2.3.   Optical Imaging of co-loaded ADS-cytotoxic drug-Liposomal dyes

A dilution series with ADS645WS-Doxorubicin-Ls is obtained, basing the starting concentration of the dilution on the dye, which is at an initial concentration of 100µM for ADS645WS. Two triplicate dilution series, one with 10% PBS and the other one with 10% Triton-X 100, with a starting concentration of 100µM, and dilution steps to 50µM, 25µM, 12,5µM, 6,5µM, 3,125µM, 1,5625µM and including a control well, are placed onto a black polystyrene 96 well plate.

Three different filter sets are used to determine the fluorescent characteristics of the co-loaded drug-dye combination in the Optical Imager.

In a first approach, in order to catch the dye's fluorescence, the Cy5.5 filter set is used for excitation, emission and background filters. Then, for Doxorubicin's characteristics, two different settings are chosen; first, DsRed is used as single filter set, for excitation, emission as well as for background subtraction. In the third image,

the previously used combination of GFP as excitation and background filter with DsRed as emission filter is chosen.

Exposure times vary between 0,5sec, 1 sec and 2sec for the imaging series.
Image analysis is performed as described under 3.4.1. Optical Imaging: *in vitro* data analysis.

3.2. *In vivo* experiments

3.2.1. Animal models

The Institutional Animal Care and Use Committee (IACUC) at the University of San Francisco, California approved this study (permission number: AN076403-1A) and it was performed in accordance with the National Institutes of Health guidelines for the humane care and use of laboratory animals as described in the *Guide for the Care and Use of Laboratory Animals (National Institutes of Health, Vol 25, No. 28, revised 1996)*.

For the *in vivo* experiments, twelve (12) 4-6 week old female nude athymic rats with an approximate weight of 200g are used (Harlan Laboratories Inc., Indianapolis, IN, USA).

The animals are kept in makrolon-cages with a grid-device cover plate in groups of three. The cage straw consisting of scrap of paper is changed weekly. Water and food are available ad libitum. The cages are kept in windowless rooms where the day and night rhythm is generated through an automatic illumination program. The day and night phases are changed every 12 hours, a dawn period is absent. The keeping of animals takes place under sterile conditions in single-ventilated cages in an air-conditioned room at 22°C and a relative atmospheric humidity of 29%. All rats are transported to the Optical Imager in their normal cages covered with a white blanket to reduce stress exposure to the animals.

3.2.2. Anesthesiology

All animals are anesthetized with Isoflurane (Isofluo, Abbott Lab, IL, USA) for cell implantation procedures as well as for Optical Imaging studies. For anesthesia induction, the animals are put in an airtight transparent plastic box connected to the Isoflurane- and an Oxygen source. The anesthesia induction dose is 5%, the maintenance dose throughout the experiments 2% for all animals. After five to ten minutes, unconsciousness sets in. The animals are then transferred from the plastic box to the Optical Imager, which is also connected to the Isoflurane- and Oxygen source, and placed so that their mouth and nose fit in specially designed mouth pieces to maintain anesthesia during the imaging process. For tail vein injections, the rats are placed on a table provided with mouthpieces connected to Isoflurane and Oxygen reservoirs.

After the Isoflurane supply is turned off, the animals regain consciousness after approximately five minutes. They are then placed in their respective cages for full recovery and closely supervised. The anesthesia shows no behavioral alteration in the animals.

3.2.3. Tumor model

Twelve (12) 4-6 week old female athymic nude Harlan rats receive subcutaneous injections of $5X10^6$ IGROV-1 ovarian cancer cells in phosphate buffered saline into the upper right abdominal quadrant or right lower flank. The tumor growth is monitored by daily inspection and palpation. The tumors are allowed to grow for 4 weeks up to a size of 0,5-1cm^2. Approximately one week before the Optical Imaging studies, the animals are put on a special non-fluorescent diet (2014, Harlan Teklad, Indianapolis, IN, USA) free of alfalfa, the component which was determined to interfere in the NIR wavelength of the investigated dyes (Bouchard et al., 2007).

The IGROV-1 ovarian cancer cell line is obtained from the Cell culture facility at the UCSF and cells are cultured in RPMI medium (Cell culture facility, UCSF, CA, USA), supplemented with 5% FCS and 1% Penicillin-Streptomycin. The cells are maintained in a humidified area of 5% CO_2 at 37°C. The cells grow in T-220 flasks

until a confluent layer of approximately 95% is obtained. For imaging experiments, the cells undergo the following steps: the media is removed from the flask and the cells are washed with PBS. Then, 7,5mL of trypsin is added to the mono-layered cells for 7 minutes. To neutralize the trypsin, 7mL of media is added to the cells; the detached monolayer is removed from the flask and put into a vial. The cells are centrifuged for 5 min at 400 RCF. The supernatant is removed from the centrifuged vial and re-suspended in 20mL. The cells are counted using Neubauer's counting chamber. Then, they are centrifuged again for 5 min at 400 RCF, re-suspended in 6mL, centrifuged for 5 min at 400 RCF and re-suspended a last time in 3,5mL of media. In the last step, the cells are tested for viability with the trypan blue exclusion test *(Contrast Media Laboratory Protocol, China Basin, UCSF, CA, USA)*.

Figure 7: *Subcutaneous injection of 5X10^6 IGROV-1 ovarian cancer cells in phosphate buffered saline into the rat's right lower flank.*

3.2.4. Injection of fluorescent dyes

For the intravenous injections, calculated doses in relation to the rats' body weight are administered in the lateral tail veins. The rats are anesthetized as previously described and placed in lateral position while anesthesia is continued. The tail is disinfected with Cutasept$^®$ and the respective fluorescent dye is injected using medical syringes and hypodermic needles.

Figure 8*: Tail vein injection of the respective fluorescent dyes*

3.2.5. Optical Imaging: data acquisition

For the *in vivo* imaging procedures, the animals are anesthetized and well placed in the center of the stage in the imaging chamber. The image sequence may now be acquired and corrected according to the imaging protocol, as described earlier under 3.1.2. Optical Imaging: data acquisition.
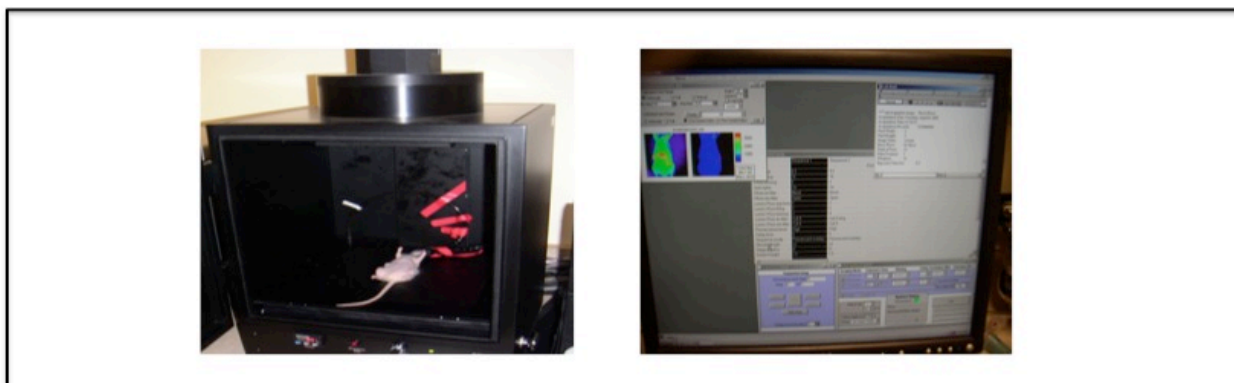
Figure 9*: Rat placement in the Optical Imager (IVIS 50) and data acquisition with Living Image 2.50 software (Xenogen, Alameda, CA, USA)*

3.2.5.1.   Optical Imaging of Doxorubicin and Doxil®

In the preliminary steps of *in vivo* imaging, a trial of three rats receiving an intravenous injection of Doxorubicin (n=2) and Doxil® (n=1) is performed. Doxorubicin and Doxil® are obtained as a stock solution with a concentration of 2mg/mL (Ben Venue Laboratories-Novation, Bedford, OH, USA). A loading dose of 10mg/kg is injected into 200g rats, leading to an injection volume of 1mL/rat. The three rats are

imaged with the IVIS 50 Optical Imager at various time points: pre-injection image, 30min post injection (pi), 1h pi, 2h pi, 4h pi, 6h pi, 24h pi and 48h pi.

Two filter set combinations are used for data acquisition: DsRed for excitation, emission as well as for background subtraction and in the second imaging series, GFP as excitation and background filter and DsRed for the emission capturing. The exposure time is set at 1,5sec. Data analysis is performed as described under 3.4.2. Optical Imaging: *in vivo* data analysis.

3.2.5.2. Optical Imaging of ADS645WS-Liposome

For the imaging of the *in vivo* fluorescent characteristics of ADS645WS-Ls, two (n=2) 200g rats receive an intravenous injection of 906µL of ADS645WS-Ls. The liposomal dye formulation provided by Hermes Biosciences Inc. (South San Francisco, CA, USA) contains a phospholipid amount of 11,01mM. When adjusting the concentration of phospholipid of the ADS645WS-Ls formulation to inject a 7,5mg/kg dose of Doxorubicin in the clinically used pegylated liposomal Doxorubicin, the amount of ADS645WS-Ls to be injected should be at a dose of 50µmol of phospholipid/kg, which amounts to 10µmol phospholipid and thus 906µL in a 200g rat.

Again, various imaging time points are chosen, starting with a pre-injection image and post injection imaging times of 30min, 1h, 2h, 4h, 6h, 8h, 24h, 48h, 72h and 96h. All the images are acquired using the Cy5.5 filter set (excitation-, emission- and background filter). Exposure times of 1sec and 2sec are obtained for every image. The animals are put on a special non-fluorescent diet approximately one week before the optical imaging studies due to the fluorescent interference as described above. Data analysis is performed as described under 3.4.2. Optical Imaging: *in vivo* data analysis.

3.2.5.3. Optical Imaging of ADS645WS-Doxorubicin-Liposome

Throughout all the imaging experiments using ADS645WS-Doxorubicin-Ls, the following parameters are kept constant: the Cy5.5 filter (excitation-, emission-, background filter) is the arbitrarily chosen filter set, the exposure time is put at 1,5sec.

Seven rats (n=7) are imaged in the ADS645WS-Doxorubicin-Ls cohort, receiving intravenous injections ranging from 0,8mL to 1mL according to their weight, of the co-loaded liposomal formulation, at a Doxorubicin dose of 7,5mg/kg, an ADS645WS concentration of 0,44mg/mL and a phospholipid amount of 50μmol/kg with liposome samples at 11,01mM.

A pre-injection image is obtained, as well as seven post injection images at 30min, 1h, 2h, 4h, 8h, 24h and 48h. Data analysis is performed as described under 3.4.2. Optical Imaging: *in vivo* data analysis.

3.3. Histology

3.3.1. Tumor specimen: data acquisition

The tumors of the animals used for preliminary data gathering of Doxorubicin's and ADS645WS-Ls's fluorescent and pharmacokinetic characteristics are not obtained and analyzed for histopathologic and fluorescent microscopic information acquisition.

As for the animals injected with ADS645WS-Doxorubicin-Ls, the extraction of the tumors is performed on all the animals after they have been sacrificed. First, the skin is removed until the subcutaneous tumor location is visible on the right lower abdomen. The vessel supply formation is documented after which the tumors are excised as a whole.
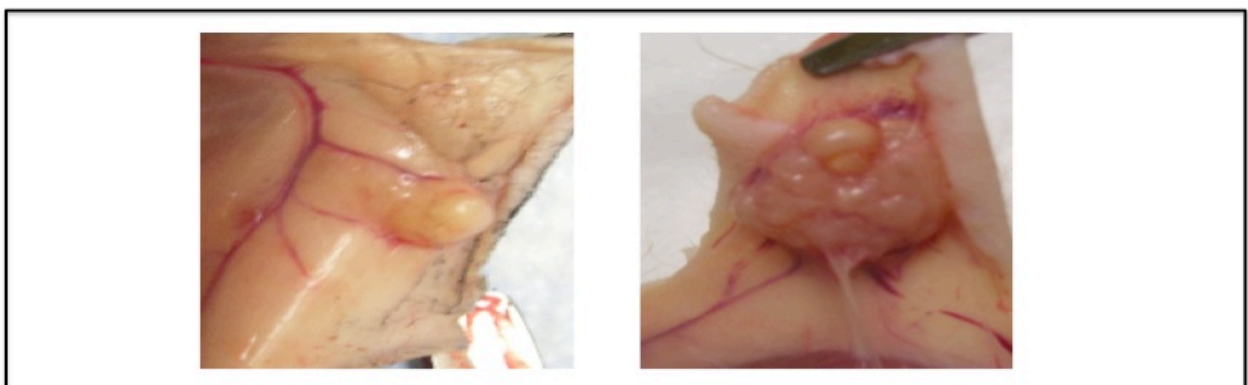
Figure 10: Macroscopic tumor visualization and demonstration of the vessel supply

They are then processed in order to obtain histopathological H&E staining (according to the H&E staining protocol of the AIDS and cancer specimen resource (ACSR) at the UCSF Mt. Zion Medical Center): The tumor specimens are kept in 24% buffered formalin for 24h, after which they are washed with PBS. The specimens are then put in 35% and 45% alcohol for 45 minutes respectively and eventually placed in 70% alcohol for conservation. The tumor specimens are cut into 10μm thick sections, placed on Superfrost/Plus slides and heated in a 50 to 55°C oven until they are dry. The obtained slides are deparaffinized for three times five minutes in Xylene, before they are rehydrated in graded alcohol series for two minutes each (100%, 100%, 95%, 95%, 70% and double distilled H_2O (ddH_2O). Then, they are stained in filtered modified Mayer's Hematoxylin diluted in 1:2 ddH_2O for three minutes. Afterwards, the slices are rinsed in a cool running water bath until the water clears (approx. 5 minutes). Lasting six minutes, the slides are stained in undiluted Harris Hematoxylin then briefly washed in warm running tap water. The excess stain is removed by a quick dip in acid alcohol (1% HCl in 70% Ethanol) and quickly rinsed again in tap water. In the next preparation step, the slides are washed in bluing reagent for 10-15 dips in ammonia water (several drops of ammonia in tap water) and subsequently rinsed in tap water. The Eosin stain is obtained exposing the slides to Y Phloxine B for thirty seconds followed by dipping them three times into 95% Ethanol. Finally, the slides are dehydrated in a graded alcohol series (95%, 95%, 100% and 100%) for two minutes each, and cleared in Xylene for five minutes.

3.4.   Data analysis

For quantitative analyses of OI data, the acquired images are analyzed with Xenogen's Living Image 2.50 software (Xenogen, Alameda, CA, USA) integrated with Igorpro (Wavemetrics, Lake Oswego, OR, USA). The images are corrected for background signal (if a sequential image is obtained) to subtract unwanted instrumental background fluorescence due to optics of the chamber or residual light leakage through the filter. They are then normalized to units of efficiency, meaning that the fluorescent emission image is normalized (divided) by a stored reference illumination image of the excitation light intensity (thus images are unitless). The value of each pixel in an efficiency image represents the fractional ratio of fluorescent emitted photons per incident excitation photons. Finally, the images are scaled for

data presentation and regions of interest (ROI), defined as 50% of the peak maximum signal intensity by the ROI software, are determined. Two separate observers analyze all the acquired images.

3.4.1. Optical Imaging: *in vitro* data analysis

For the *in vitro* experimental setup, all Optical Imaging data is scaled to identical values (maximum value: 600×10^{-6} units of efficiency, minimum value: 50×10^{-6} units of efficiency).

ROIs are determined as circular area of each plate well in the 96-well plates (0,75cm x 0,75cm), leading to 24 ROIs for every dilution series.
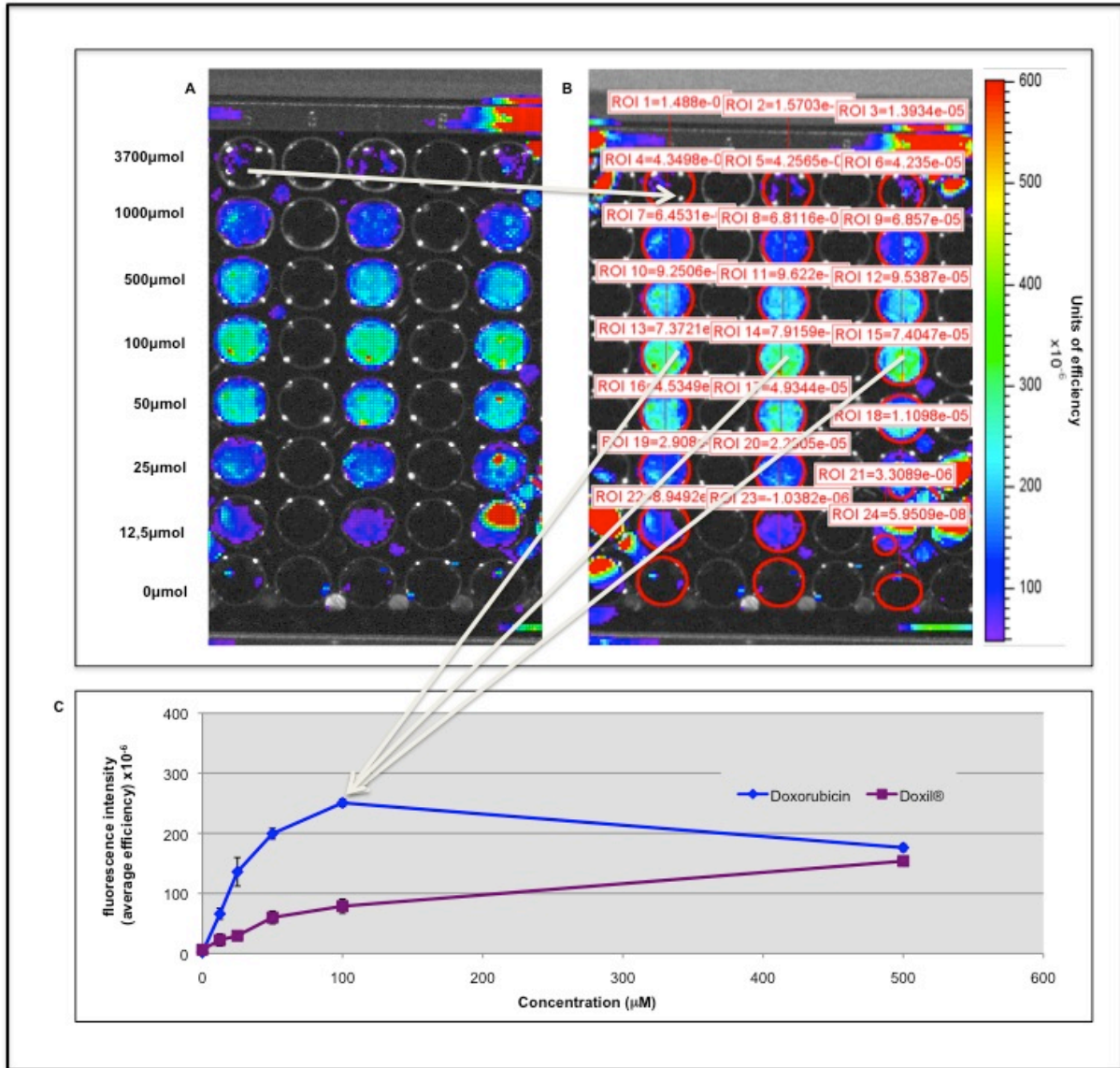
Figure 11: *Optical Imaging of Doxorubicin dilution series and determination of regions of interest - Example of in vitro data acquisition and data analysis: (A) Optical Imaging of Doxorubicin dilution series in PBS (from 0μM to 3700μM). The DsRed filter set is used for excitation, emission and background subtraction. (B) Regions of interest are drawn over each well plate and the fluorescence intensity is determined in units of average efficiency. (C) A graph according to the regions of interest is drawn for concentrations ranging from 0μM to 500μM. Fluorescence intensity (Y-axis) is determined at each concentration point (X-axis). Fluorescence intensity is measured in units of efficiency; error bars represent standard deviation of the mean.*

3.4.2. Optical Imaging: *in vivo* data analysis

For the images acquired in the *in vivo* part of the study, scaling varies for Doxorubicin

and Doxil$^{®}$ (maximum value: 100×10^{-6} units of efficiency, minimum value: 10×10^{-6} units of efficiency), ADS645WS-Ls (maximum value: 200×10^{-6} units of efficiency, minimum value: 50×10^{-6} units of efficiency) and for ADS645WS-Doxorubicin-Ls (maximum value: 150×10^{-6} units of efficiency, minimum value: 10×10^{-6} units of efficiency).

For the region of interest determination, a measurement ROI (1,20cm x 1,25cm) as well as a background ROI (1,71cm x 1,71cm) are defined. When this background ROI is linked to the measurement ROI, subtraction of the average signal in the background ROI from the average signal in the measurement ROI is performed (measurement ROI-background ROI) and helps to reduce fluorescence signal disturbance due to tissue autofluorescence *(Xenogen, Living Image Software Manual, Version 2.50, 2004, p.84)*.

For the determination of the fluorescent signal intensity at various time points in comparison to the pre-injection time point, the measurement region of interest is placed over the fluorescent signal region from the tumor tissue and the background ROI over a non-signal emitting tissue area are arbitrarily defined for every animal at every imaging time point *(shown in Figure 12)*.

For the comparison of fluorescence signal enhancement over ovarian cancer tissue region to fluorescence intensity over control animal tissue, two measurement- and one background ROI are defined. The first measurement and background couple is determined as described above, over tumor tissue for the measurement ROI and over a non-emitting region for the background ROI. For the second couple, a measurement ROI is placed over the left lower flank as well as a corresponding background ROI over the same non-emitting region as for the first couple (not shown).
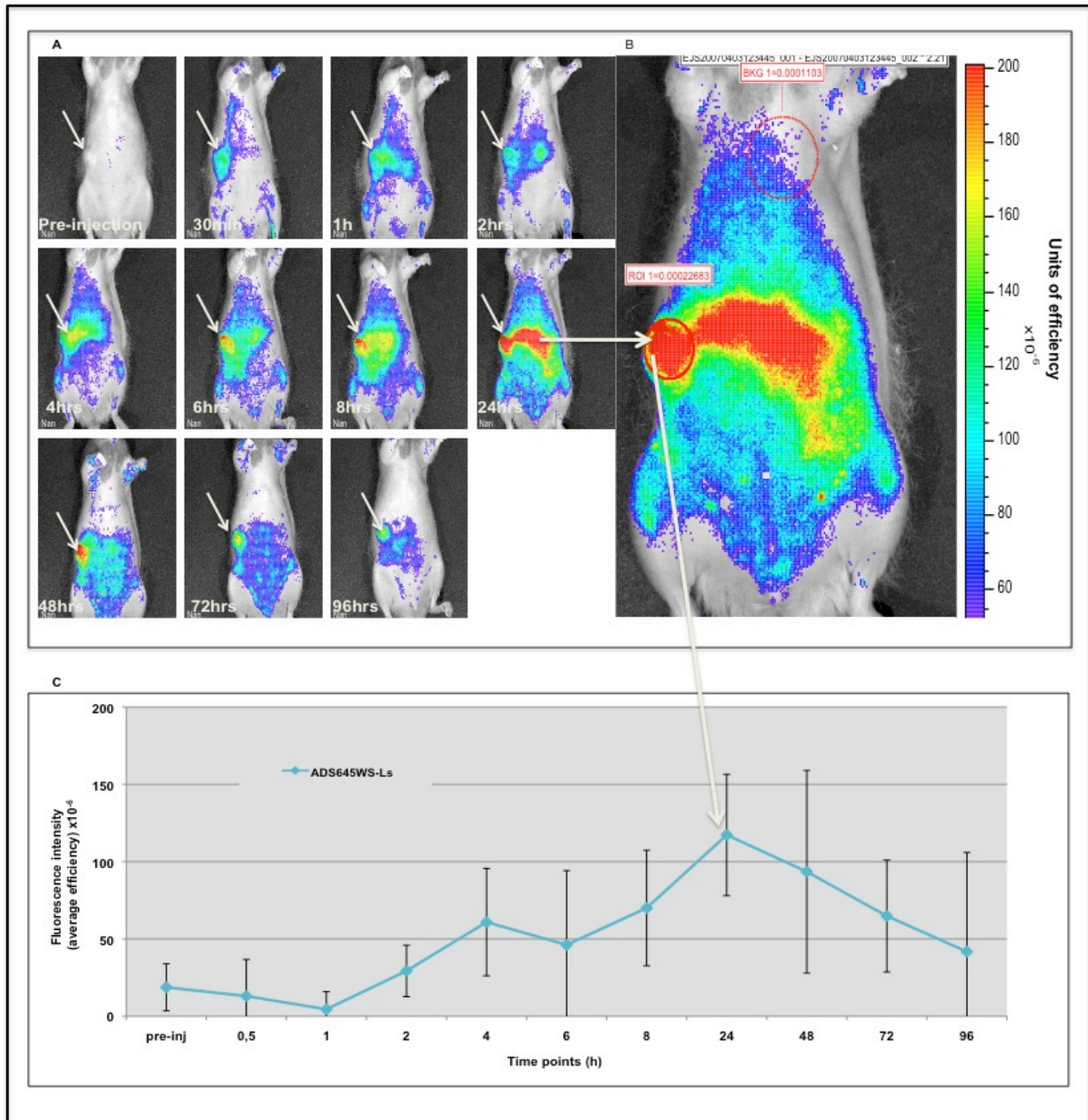
Figure 12: *Optical Imaging of fluorescent signal intensity after injection of a liposomal formulation and determination of regions of interest - Example of in vivo Optical Imaging data acquisition and data analysis: (A) Optical Imaging of an IGROV-1 injected rat after administration ADS645WS-Liposome. Arrow indicates approximate tumor location. The Cy5.5 filter set is used for excitation, emission and background subtraction. (B) A measurement region of interest is placed over the fluorescent signal area from the tumor tissue at each time point. Then a background region of interest is placed and can reduce the effect of the background emission on region of interest measurements. (C) A graph according to the regions of interest is drawn for each rat at each time point. Fluorescence intensity (representing the average post-injection-pre-injection fluorescence) (Y-axis) is determined at each time point (X-axis). The fluorescence intensity is determined in units of efficiency; error bars represent standard deviation of the mean.*

3.5. Statistical analysis

All *in vitro* experiments are performed in triplicates. All data is displayed as mean +/- standard deviation of the mean (SDM). Student t-tests are used to detect significant differences in fluorescence of the ADS645WS-Doxorubicin-Ls dilution series in comparison to control media (*in vitro* data) and in ovarian cancer tissue in comparison to control animal tissue for the whole ADS645WS-Doxorubicin-Ls group (n=7) and an arbitrarily defined sub-group (n=3). Moreover, the ratio of post-injection fluorescent signal enhancement in tumor tissue at various time points in comparison to the pre-injection fluorescent signal intensity (FSI post-injection/pre-injection), again for n=7 and n=3, is calculated (*in vivo* data). A p-value of less than 0,05 is considered to be statistically significant. All statistical calculations are obtained with Microsoft Office Excel (Microsoft Corporation, Redmond, WA, USA).

For the *in vitro* analysis, an unpaired two-tailed t-test is performed. The triplicate (n=3) of every concentration point is compared to the control triplicate (n=3).

For the *in vivo* analysis, two different setups are evaluated as described above. For the FSI post-injection/pre-injection ratio, a paired two-tailed t-test is used. In a second analysis, the ovarian cancer region (right lower flank, region of interest 1) is compared to control tissue of the same animal (left lower flank, region of interest 2) at every imaging time point (n=7 and n=3). For this data, a paired two-tailed t-test is performed as well.

Since the Doxorubicin, Doxil® and ADS-Ls studies only constitute preliminary data acquisition and lack subject quantity, no statistical analysis is obtained for these samples *in vitro* or *in vivo*.

4. Results

4.1. *In vitro* experiments

4.1.1. Spectrophotometry

4.1.1.1. Spectrophotometry of Doxorubicin and Doxil®

Even though Doxorubicin has a well-documented fluorescence, we determined its wavelength pattern with the excitation maximum at 485nm and the emission maximum at 592nm. For Doxil®, the wavelength profile ranges from 490nm to 610nm. All data is acquired with a plate reader and its software (Molecular device Spectro Max Fluorescence Plate Reader and Spectro Pro 5.0.1 software).
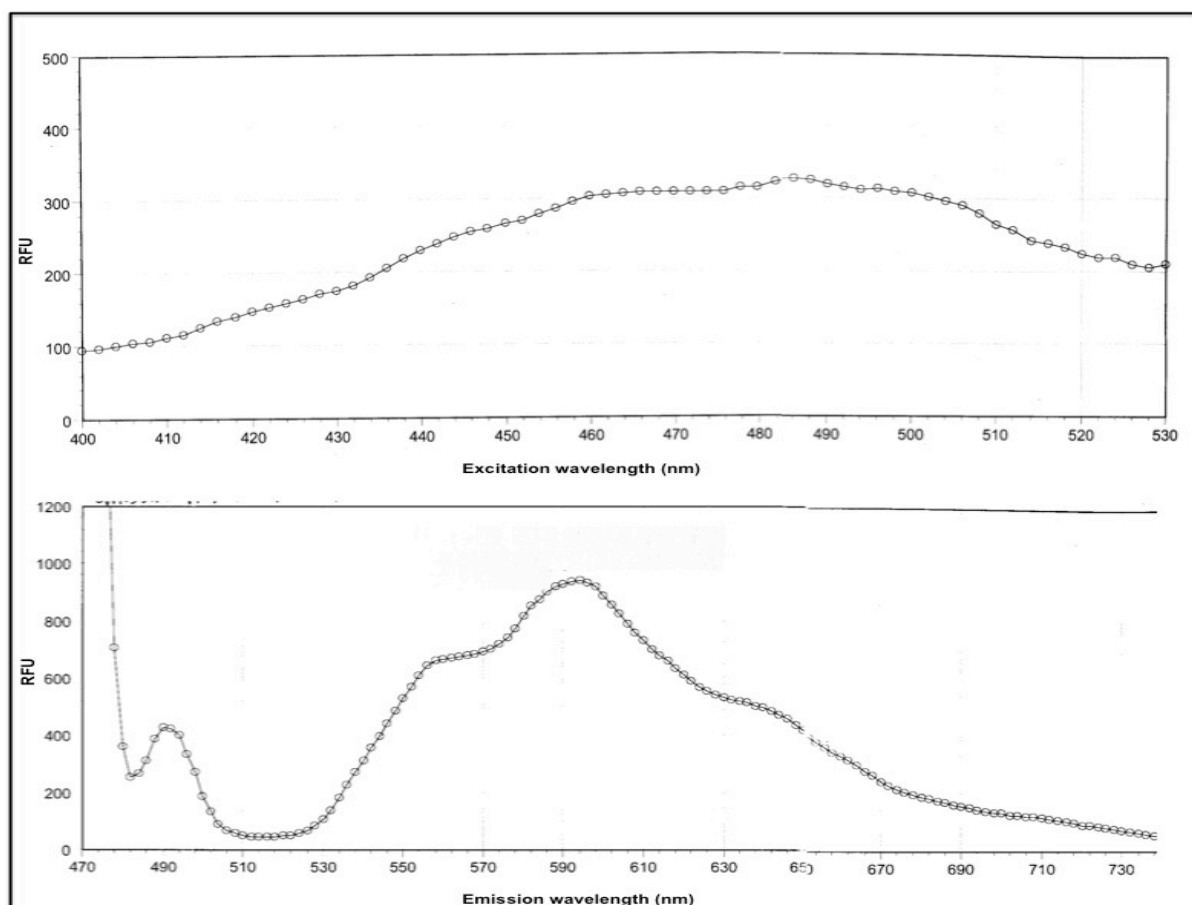
Figure 13*: Excitation and Emission profile of Doxorubicin (x-axis: wavelength (nm); y-axis: relative fluorescence units (RFU))*
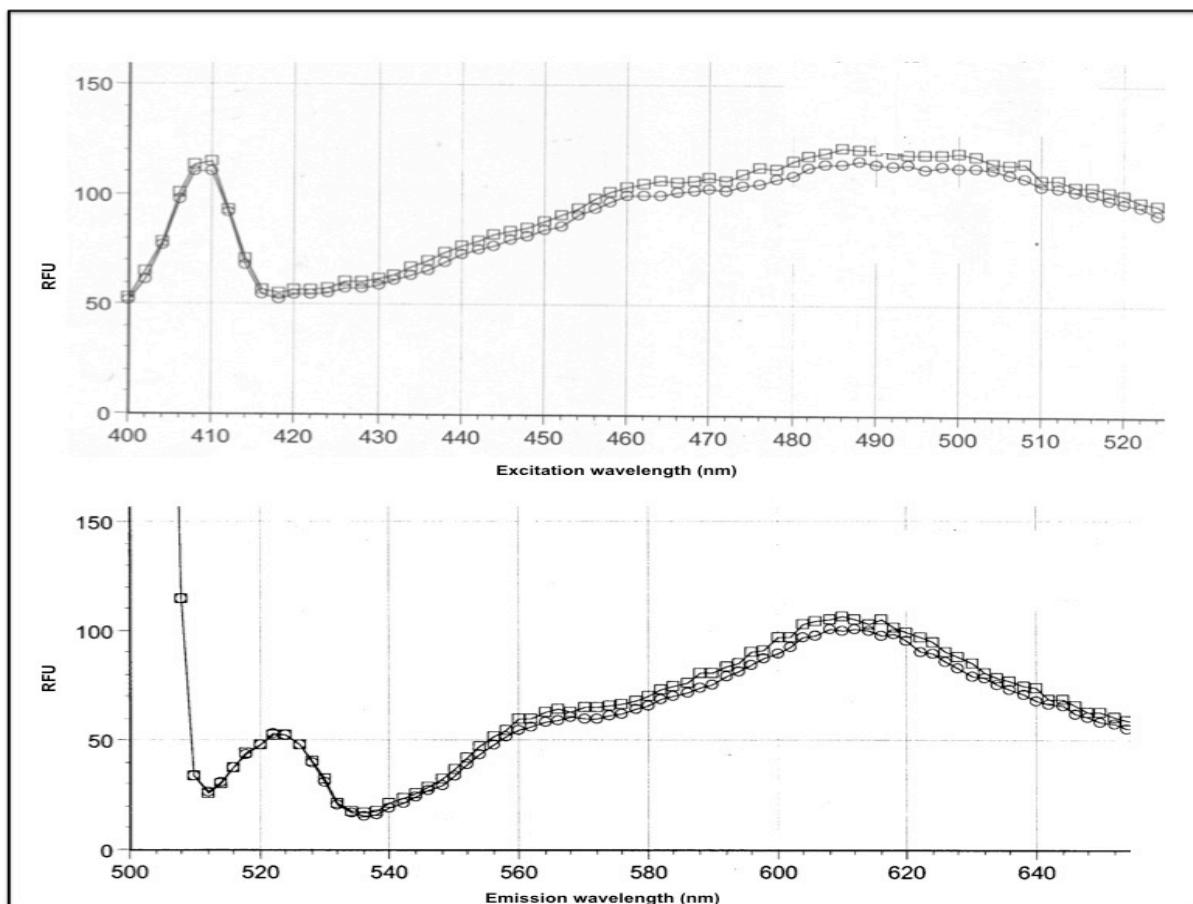
Figure 14*: Excitation and Emission profile of Doxil® (x-axis: wavelength (nm); y-axis: relative fluorescence units (RFU))*

4.1.1.2.   Spectrophotometry of ADS-Liposomal dyes

The U-2800 Spectrophotometer (Hitachi High Technologies America, San Jose, CA) is used throughout the whole experimental setup and the settings as described in "3.1.1.2. Spectrophotometry of ADS-Liposomal dyes" are kept constant.

For the ADS645WS-Ls dye, the scan result shows an absorption maximum (Abs) of 0,349 at 654nm with an extinction coefficient of $\varepsilon=1,80 \times 10^5$L/molxcm. The concentration of the sample in the Spectrophotometer's cuvette is determined by Beer's Law to a molarity of $1,93 \times 10^{-3}$mM; leading to an actual concentration of 97,5µM (~100µM).
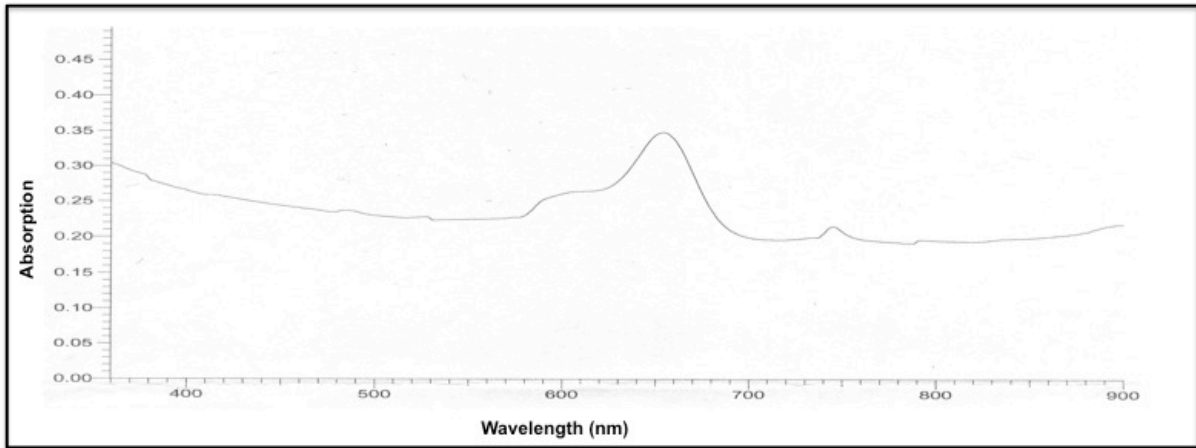
Figure 15: *Spectrophotometry of ADS645WS-Liposome (x-axis: wavelength (nm); y-axis: absorption)*

For ADS780WS-Ls, an absorption maximum of 1,65 at 796nm with an extinction coefficient of $\varepsilon=1,70 \times 10^5$L/molxcm is obtained. The concentration of the sample in the cuvette shows a molarity of $9,71 \times 10^{-3}$mM leading to an actual concentration of 1942µM (~1900µM).
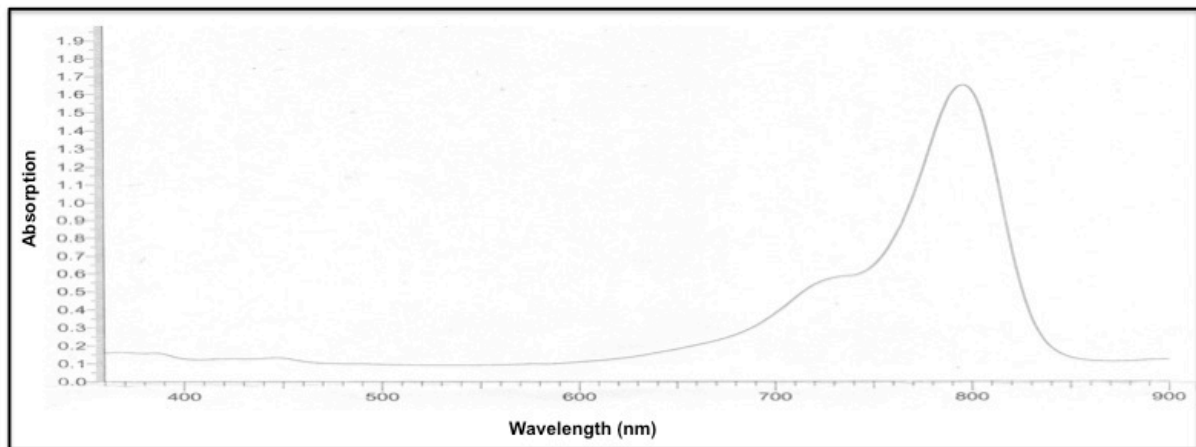
Figure 16: *Spectrophotometry of ADS780WS-Liposome (x-axis: wavelength (nm); y-axis: absorption)*

For ADS780NH$_2$-Ls the absorption maximum is at 1,328 at 794nm with an extinction coefficient of $\varepsilon=1,52 \times 10^5$L/molxcm. The sample's concentration in the cuvette having a molarity of $8,75 \times 10^{-3}$mM, leads to an actual concentration of 175µM (~100µM) once again determined by Beer's Law.
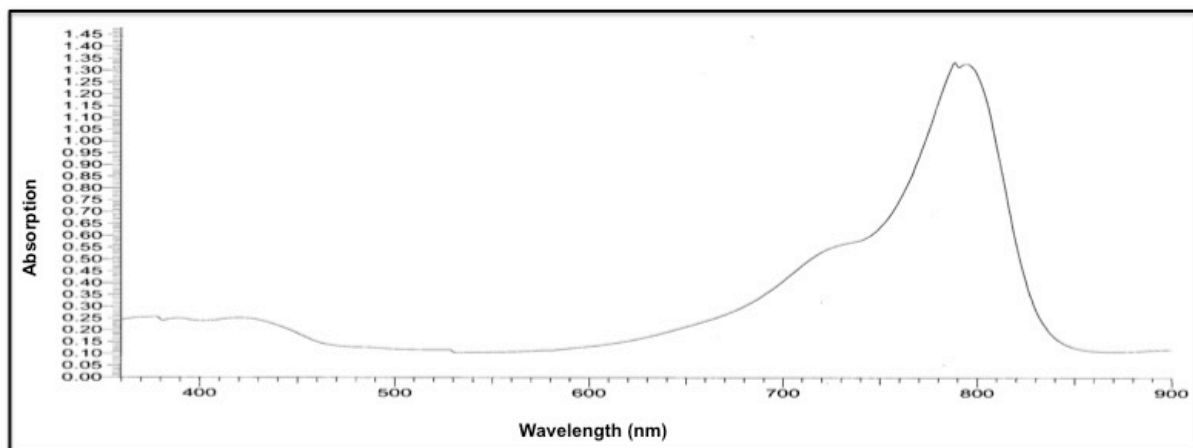
Figure 17: *Spectrophotometry of ADS780NH$_2$-Liposome (x-axis: wavelength (nm); y-axis: absorption)*

The emission (Em.) profiles of the three liposomal dyes used are kindly provided by Hermes Biosciences Inc. (South San Francisco, CA). For ADS645WS-Ls, an emission of 660nm is determined. For ADS780WS-Ls and ADS780NH$_2$-Ls the profiles are Ex.: 796nm/Em.: 820nm and Ex.: 794nm/Em.: 812nm respectively.

4.1.2. Optical Imaging: data analysis

After testing various filter set combinations in the preliminary data acquisition, the filter sets for the *in vitro* data analysis are chosen as follows: the DsRed filter set (excitation, emission as well as background subtraction) is used for all Doxorubicin and Doxil® images. The Cy5.5 filter set (excitation, emission, background subtraction) is used for all ADS645 images and the ICG filter set (excitation, emission, background subtraction) for all ADS780 data. All *in vitro* experiments are performed in triplicates. Data is displayed as means plus/minus the standard deviation of the mean (SDM).

4.1.2.1. Optical Imaging of Doxorubicin and Doxil®
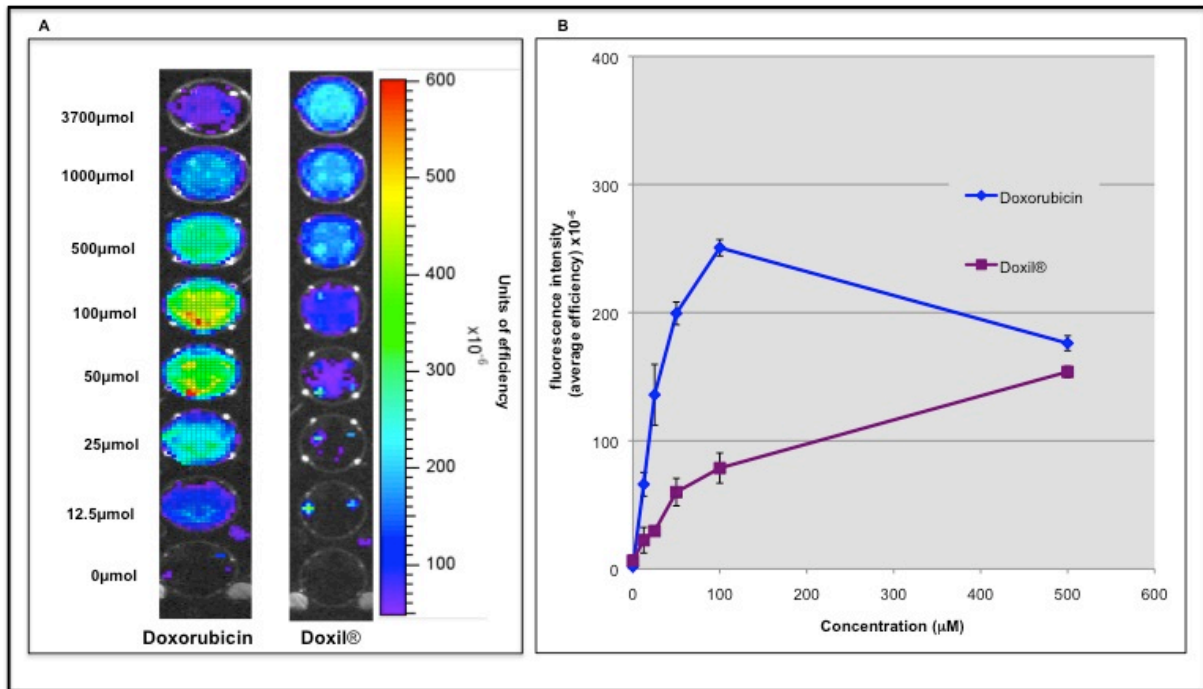
Figure 18: (A) Optical Imaging of dilution series of Doxorubicin and Doxil® in PBS (single row of triplicate shown). The DsRed filter set is used for excitation, emission and background subtraction. (B) A graph according to the regions of interest is drawn for both cytotoxic agents (concentration range from $0\mu M$ to $500\mu M$). Fluorescence intensity (Y-axis) is determined at each concentration point (X-axis). Fluorescence intensity is measured in units of efficiency; error bars represent standard deviation of the mean.

A triplicate dilution series is obtained for Doxorubicin and Doxil® as described above. For Doxorubicin, the highest intensity of fluorescence ($250,63 \times 10^{-6}$ +/- $6,37 \times 10^{-6}$) is determined at a concentration of $100\mu M$. For Doxil®, the fluorescence intensity shows a maximum value ($183,47 \times 10^{-6}$ +/- $2,40 \times 10^{-6}$) at the $3700\mu M$ concentration mark (not shown in the graph) and a linear decrease of fluorescence intensity with concentration can be observed.

4.1.2.2. Optical Imaging of ADS and ADS-Liposomal Near-Infrared-dyes
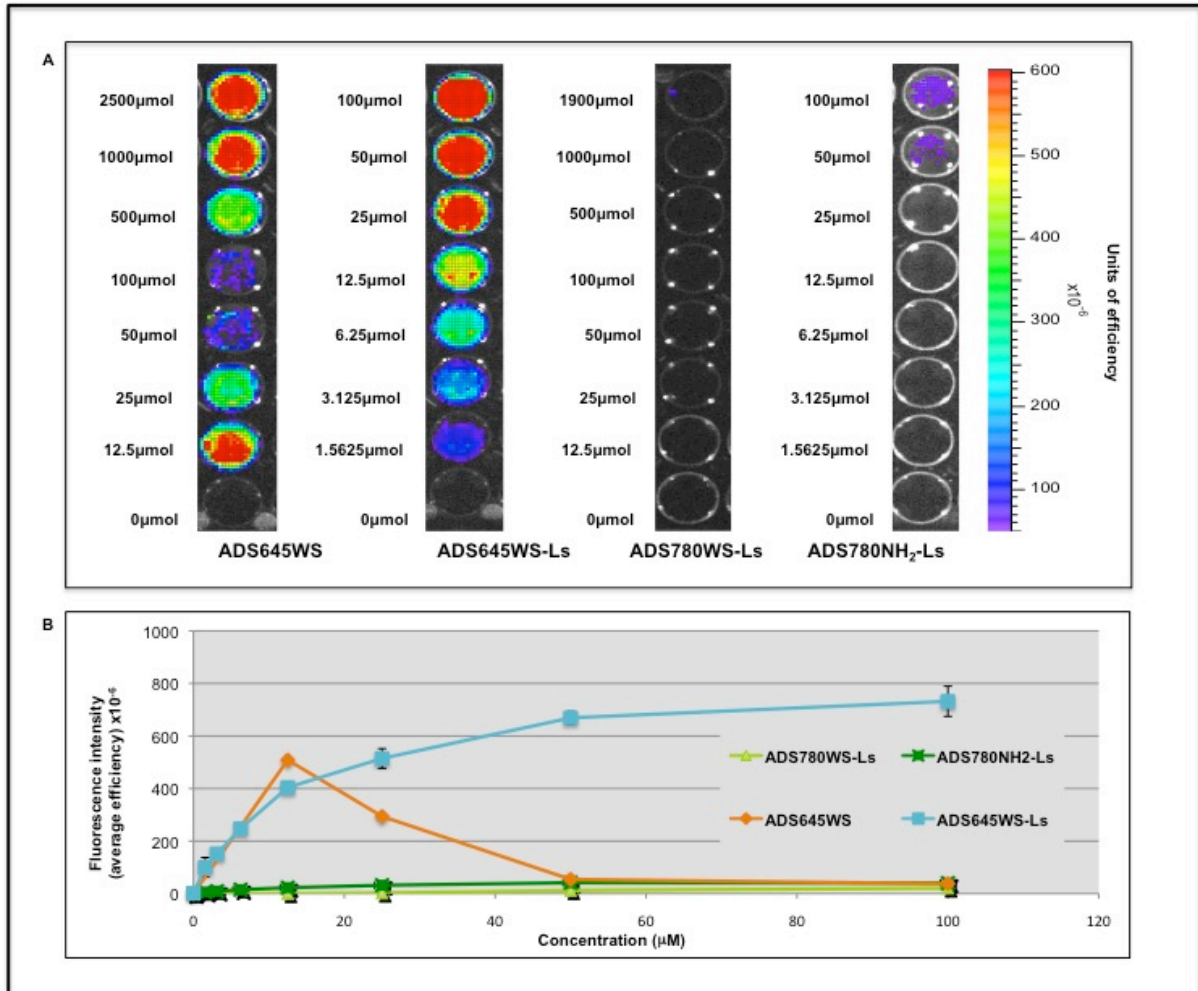
Figure 19: *(A) Optical Imaging of dilution series of ADS645WS, ADS645WS-Ls, ADS780WS-Ls and ADS780NH₂-Ls in PBS (single row of triplicate shown). The Cy5.5 (for the ADS645 group) and the ICG (for the ADS780 group) filter sets are used for excitation, emission and background subtraction. (B) A graph according to the regions of interest is drawn for all agents (concentration range from 0μM to 100μM). Fluorescence intensity (Y-axis) is determined at each concentration point (X-axis). Fluorescence intensity is measured in units of efficiency; error bars represent standard deviation of the mean.*

Triplicate dilution series are obtained for every agent and imaged with the Optical Imager. For ADS645WS, the fluorescence peak is at the highest concentration of 2500μM ($568{,}20 \times 10^{-6}$ +/- $7{,}55 \times 10^{-6}$) (not shown in the graph). A non-linear fluorescence can be observed, leading to a second fluorescent peak at 12,5μM ($508{,}57 \times 10^{-6}$ +/- $4{,}14 \times 10^{-6}$). ADS645WS-Ls has its fluorescent peak at a concentration of 100μM ($731{,}93 \times 10^{-6}$ +/- $5{,}74 \times 10^{-6}$), ADS780WS-Ls at 1000μM

$(25,57 \times 10^{-6}$ +/- $1,02 \times 10^{-6})$ (not shown in the graph) and ADS780NH$_2$-Ls also at 100μM $(40,05 \times 10^{-6}$ +/- $10,80 \times 10^{-6})$. There is a linear decrease in fluorescence intensity in these three agents.

4.1.2.3. Optical Imaging of co-loaded ADS-cytotoxic drug-Liposomal dye
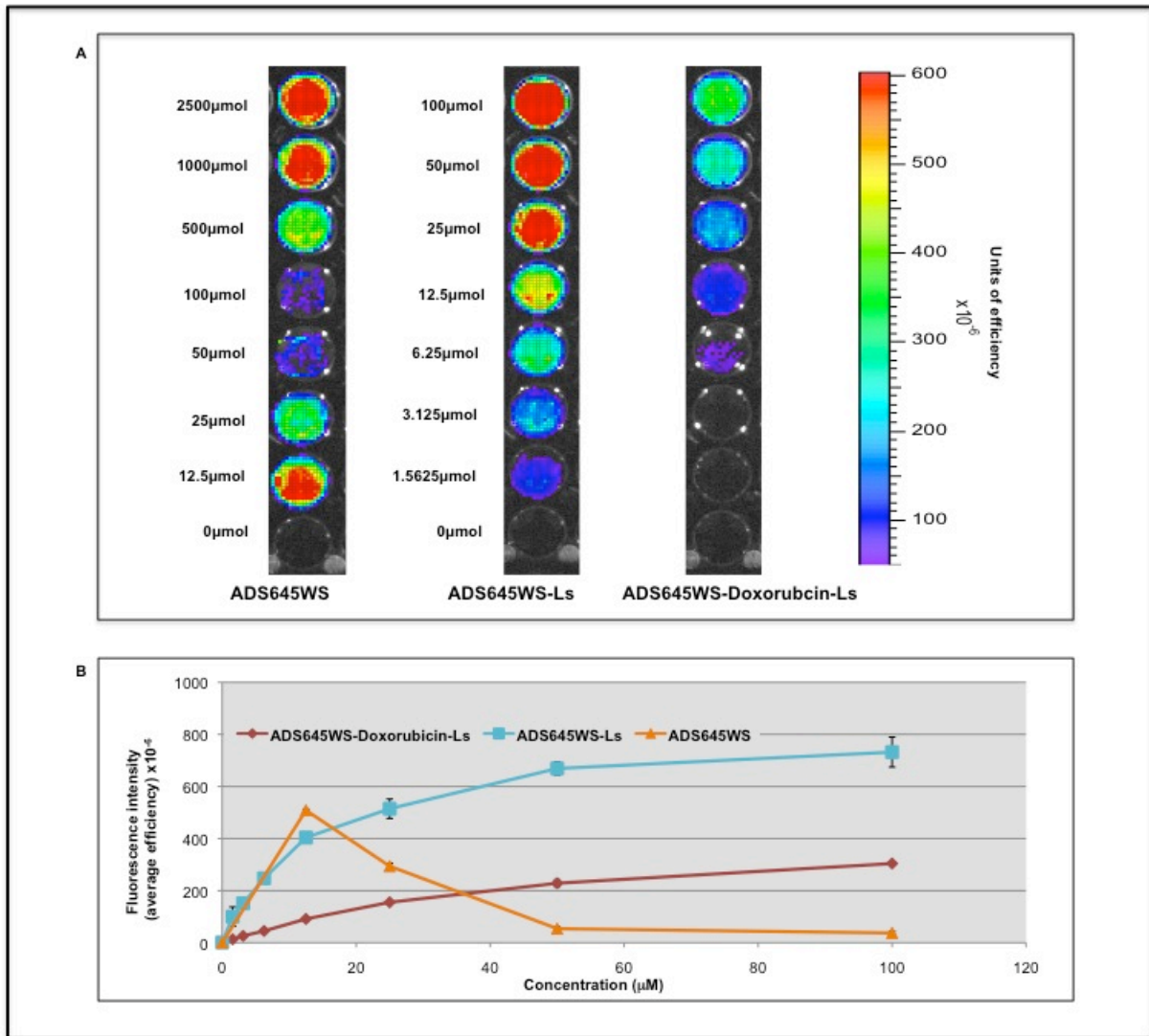
Figure 20: (A) Optical Imaging of dilution series of ADS645WS, ADS645WS-Ls and ADS645WS-Doxorubicin-Ls in PBS (single row of triplicate shown). The Cy5.5 filter set is used for excitation, emission and background subtraction. (B) A graph according to the regions of interest is drawn for all agents (concentration range from 0μM to 100μM). Fluorescence intensity (Y-axis) is determined at each concentration point (X-axis). Fluorescence intensity is measured in units of efficiency; error bars represent standard deviation of the mean.

The fluorescence pattern of ADS645WS as well as ADS645WS-Ls has been described previously. ADS645WS-Doxorubicin-Ls has similar fluorescence intensity than ADS645WS-Ls with peak intensity at a concentration of $100\mu M$ ($304,17 \times 10^{-6}$ +/- $4,14 \times 10^{-6}$) (p = $0,026 \times 10^{-6}$) and a linear intensity decrease. Starting at the first concentration point of $1,5625\mu M$ up to $100\mu M$, fluorescence is significantly higher in comparison to control media for ADS645WS-Doxorubicin-Ls (p = 0,0021).

4.2. *In vivo* experiments

4.2.1. Optical Imaging: data analysis

For the *in vivo* part of the study, the DsRed (excitation, emission, background subtraction) filter set is chosen for all experiments with Doxorubicin and Doxil®. The Cy5.5 filter set (excitation, emission, background subtraction) is taken for all the data acquisition of ADS645WS-Ls and ADS645WS-Doxorubicin-Ls. For all obtained fluorescent signals, the pre-injection time point fluorescence intensity is subtracted from each post-injection time point's image (post-injection(xh)-pre-injection). This subtraction is not performed for statistical analysis.

4.2.1.1. Optical Imaging of Doxorubicin and Doxil®
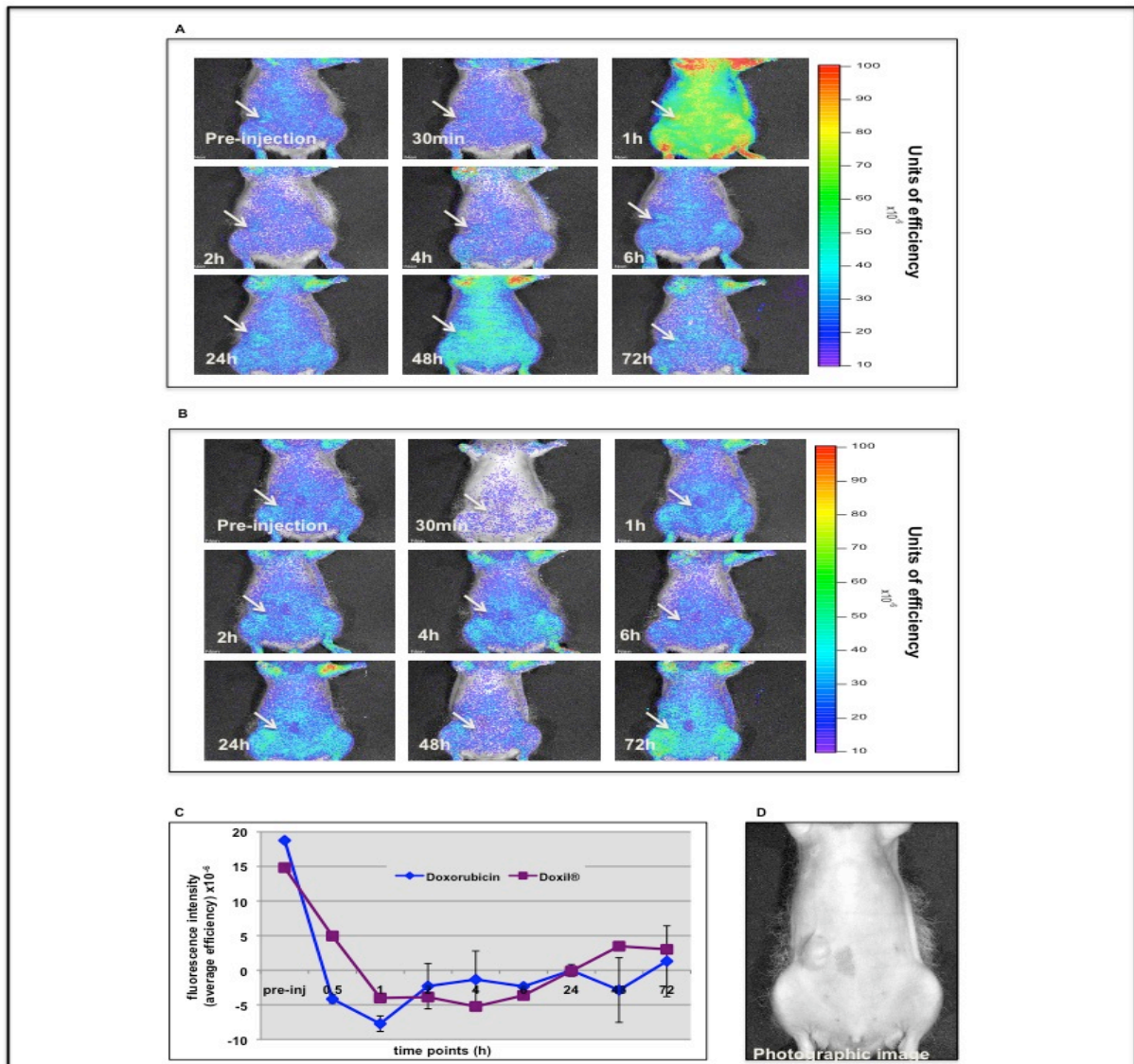
Figure 21*: Optical Imaging of the fluorescent signal intensity of an IGROV-1 injected rat after administration of (A) Doxorubicin or (B) Doxil®. Arrow indicates approximate tumor location. The DsRed filter set is used for excitation, emission and background subtraction. (C) A graph according to the regions of interest is drawn for each rat (n=2 for Doxorubicin, n=1 for Doxil®) at each time point. Fluorescence intensity (representing the average post-injection-pre-injection fluorescence) (Y-axis) is determined at each time point (X-axis). The fluorescence intensity is determined in units of efficiency; error bars represent standard deviation of the mean. (D) A photographic image is displayed to show tumor location.*

No fluorescence pattern can be defined throughout the entire time point span in the imaging process. In the images obtained, it is mostly the fur of the animals that shows a slight fluorescence, but no clear fluorescent accumulation can be seen over

the tumor region of the rats, neither for those injected with Doxorubicin nor for the rats which received a Doxil® injection.

4.2.1.2.   Optical Imaging of ADS645WS-Liposome
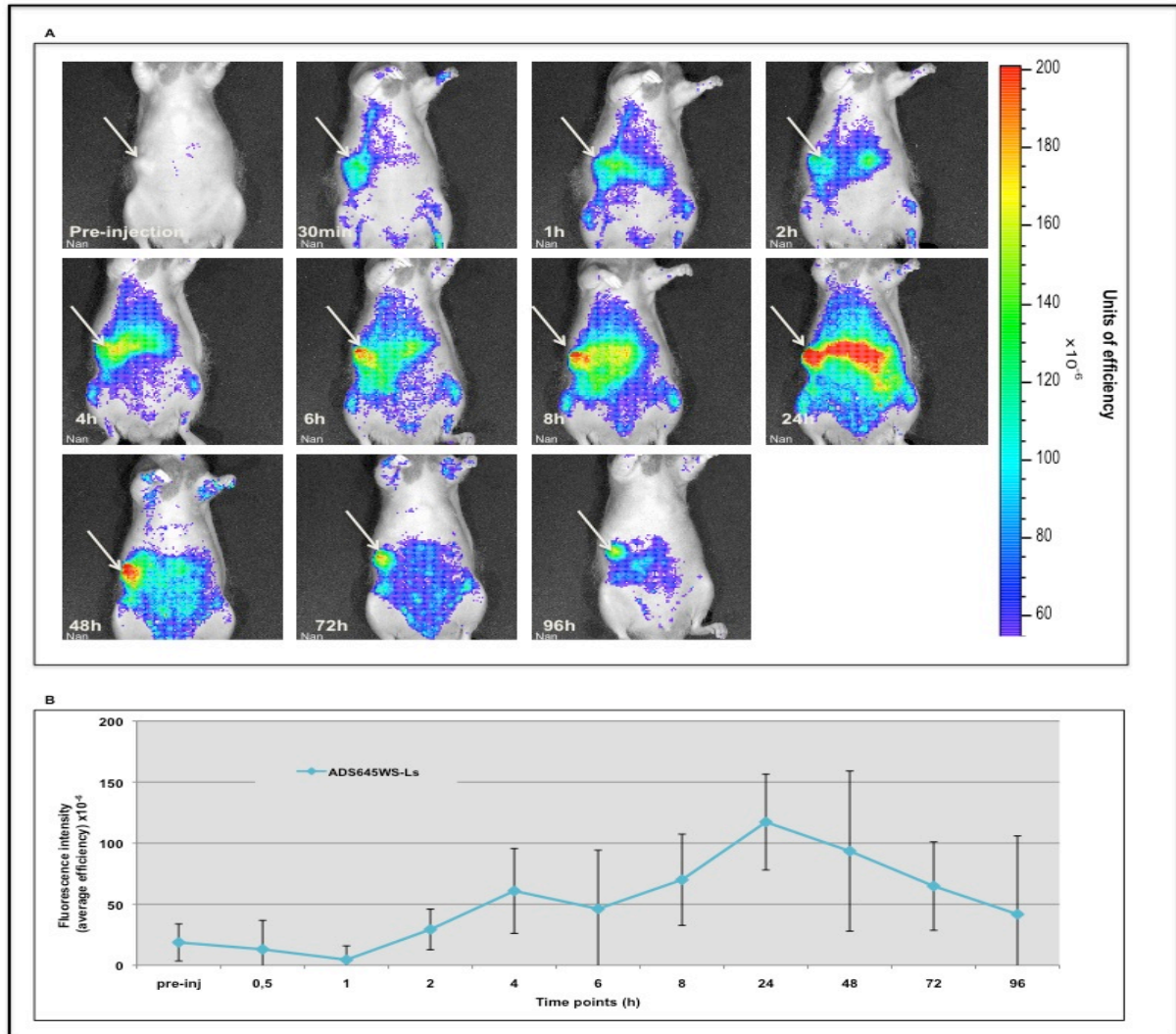
Figure 22: (A) Optical Imaging of the fluorescence signal intensity of an IGROV-1 injected rat after administration ADS645WS-Ls. Arrow indicates approximate tumor location. The Cy5.5 filter set is used for excitation, emission and background subtraction. (B) A graph according to the regions of interest is drawn for each rat (n=2) at each time point. Fluorescence intensity (representing the average post-injection-pre-injection fluorescence) (Y-axis) is determined at each time point (X-axis). The fluorescence intensity is determined in units of efficiency; error bars represent standard deviation of the mean.

For the analysis of the two rats receiving an intravenous ADS645WS-Ls injection, the gathered images show a clear fluorescence pattern. For the first animal imaged

(shown in graph), the fluorescence projected to the rat's surface increases in intensity with every imaging time point. A first fluorescence peak is observed at 24h ($145,03 \times 10^{-6}$ +/- $39,26 \times 10^{-6}$) mainly projected over the hepatic-, the intestinal- and subsequently moving to the tumor region, where a second, more delimited fluorescent peak is reached at the 48h post injection time point ($139,85 \times 10^{-6}$ +/- $65,57 \times 10^{-6}$), lasting until the last obtained time point of 96h ($87,12 \times 10^{-6}$ +/- $64,15 \times 10^{-6}$) post injection.

The second rat (not shown) shows a similar fluorescent pattern with a marked fluorescent peak over the tumor region at 24h post injection ($89,51 \times 10^{-6}$ +/- $39,26 \times 10^{-6}$). A slight fluorescence is already visible at the pre-injection image, but the major fluorescent enhancement develops over the course of the post-injection imaging time points. In contrary to the first liposomal dye imaging sequence, where the fluorescence stays over the tumor region throughout the entire imaging process, the fluorescence here shifts to the surrounding area of the tumor in further imaging points (48h and 72h) ($47,12 \times 10^{-6}$ +/- $65,57 \times 10^{-6}$ and $39,20 \times 10^{-6}$ +/- $36,22 \times 10^{-6}$). Of note is the relatively strong fluorescence projecting of the intestinal-and hepatic regions to the rat's surface.

4.2.1.3. Optical Imaging of ADS645WS-Doxorubicin-Liposome

In the ADS645WS-Doxorubicin-Ls cohort, the image analysis leads to the splitting of the acquired images into three sub-groups: Three (n=3) (arbitrarily rat 1-3) of the rats show a fluorescence pattern overlapping the tumor region at different time points, the images of two (n=2) (4&5) rats in the second group show fluorescence surrounding the tumor tissue and the third group consisting of two (n=2) (6&7) rats, shows no fluorescent pattern in the tumor region whatsoever.

For the FSI post-injection/pre-injection, the overall fluorescent analysis (n=7) shows a significant fluorescent signal enhancement in comparison to the pre-injection image for all acquired time points ($p < 0,02$).
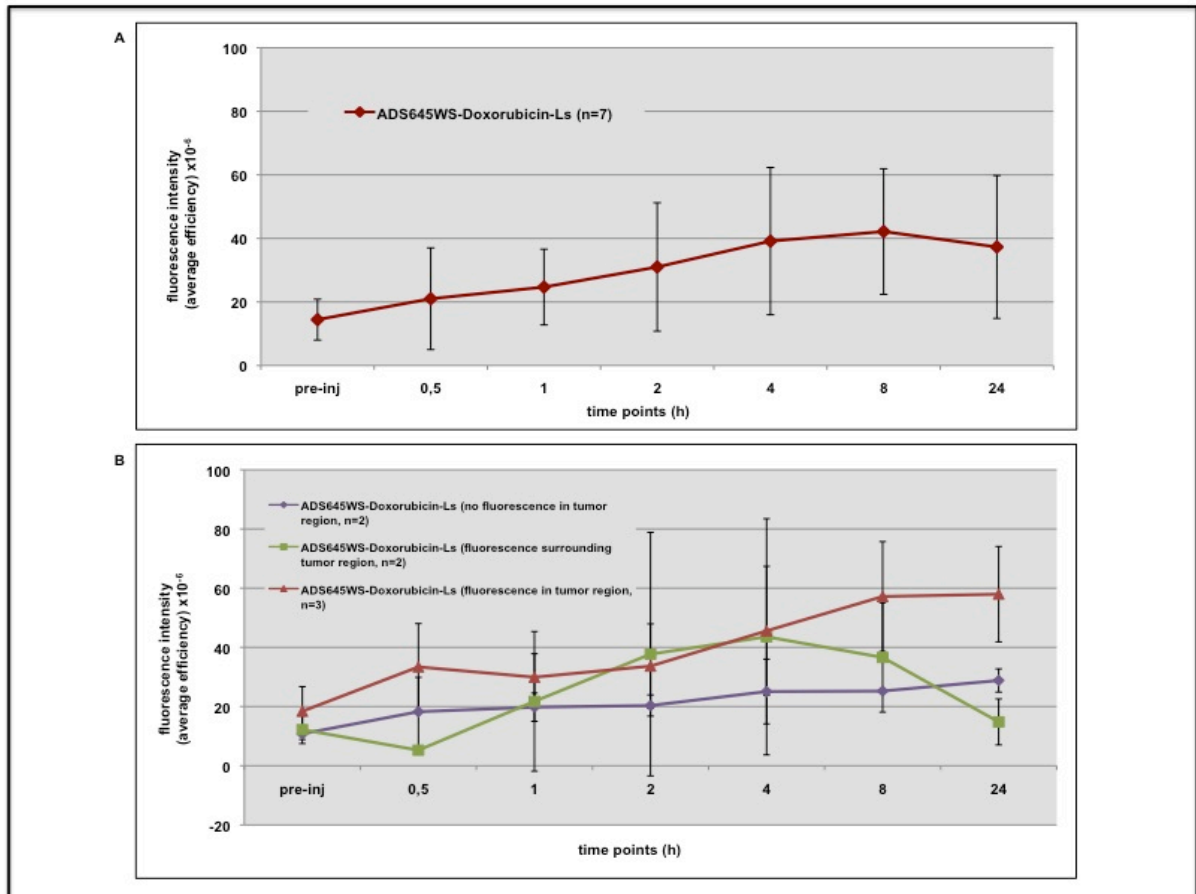
Figure 23*: Fluorescence signal intensity after the injection of ADS645WS-Doxorubicin-Liposome. (A) Graph according to the regions of interest drawn for every animal at each time point in the ADS645WS-Doxorubicin-Liposome group (n=7). (B) Splitting of the group into three sub-groups according to fluorescent pattern. The Cy5.5 filter set is used for excitation, emission and background subtraction. Fluorescence intensity (representing the average post-injection-pre-injection fluorescence) (Y-axis) is determined at each time point (X-axis). The fluorescence intensity is determined in units of efficiency; error bars represent standard deviation of the mean.*

In addition to the overall (n=7) fluorescence signal intensity determination, the three rats (n=3) of the first arbitrarily chosen sub-cohort are worked up for statistical analysis. For all three rats (only one rat shown), a beginning of marked tumor fluorescence enhancement is visible at 2h ($33,65 \times 10^{-6}$ +/- $14,28 \times 10^{-6}$) post injection, with a maximum intensity at the 8h and 12h time point images ($57,18 \times 10^{-6}$ +/- $18,54 \times 10^{-6}$ and $58,46 \times 10^{-6}$ +/- $17,16 \times 10^{-6}$). The tumor fluorescence is partly overlaid by intestinal fluorescence, but is still visible and delimitable to intestinal- and urinary signals until the last obtained time point at 28h ($59,22 \times 10^{-6}$ +/- $21,50 \times 10^{-6}$). A

significant fluorescent enhancement is visible over the tumor region at the 8h (p <0,03) and 12h (p < 0,02) time points.
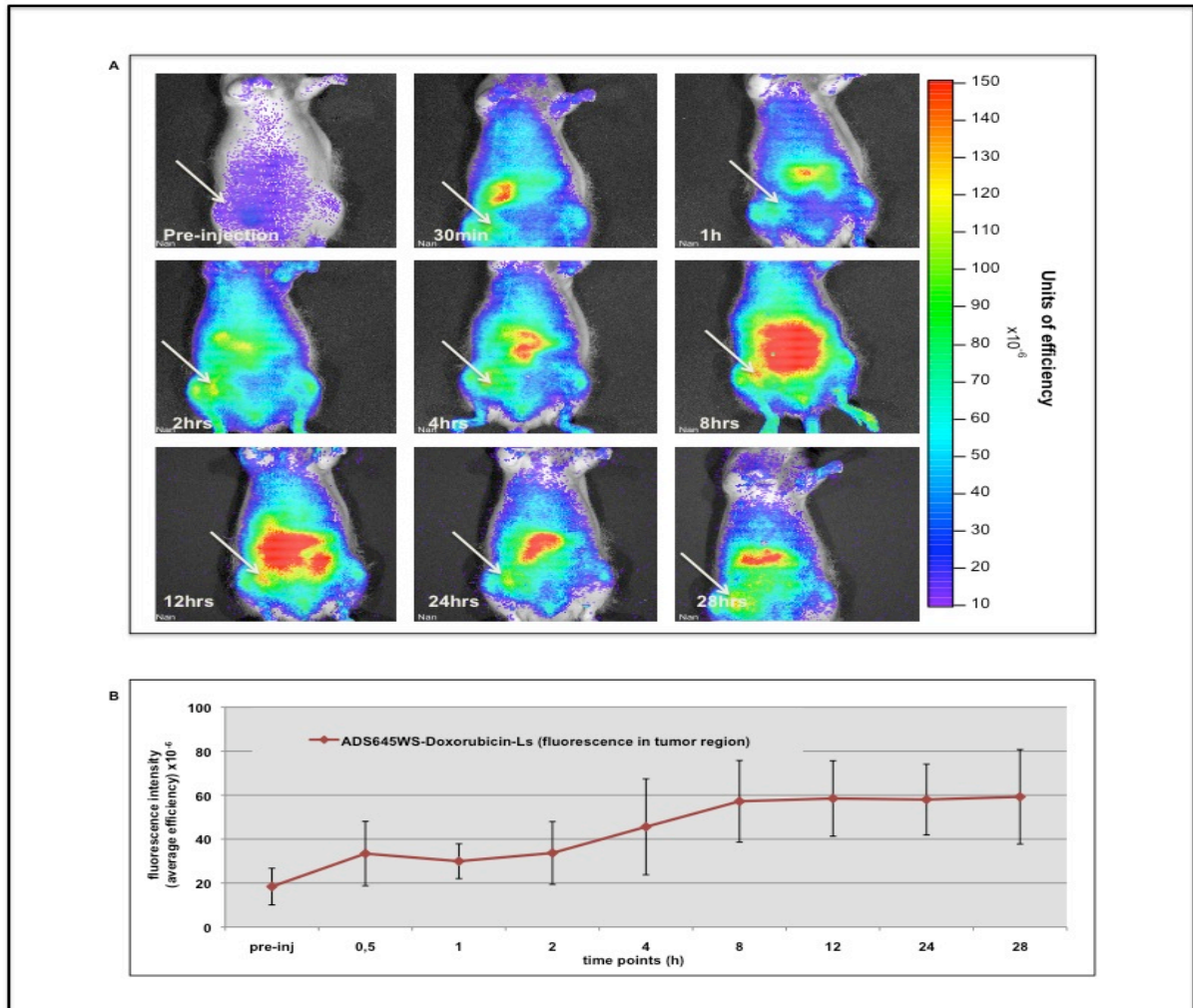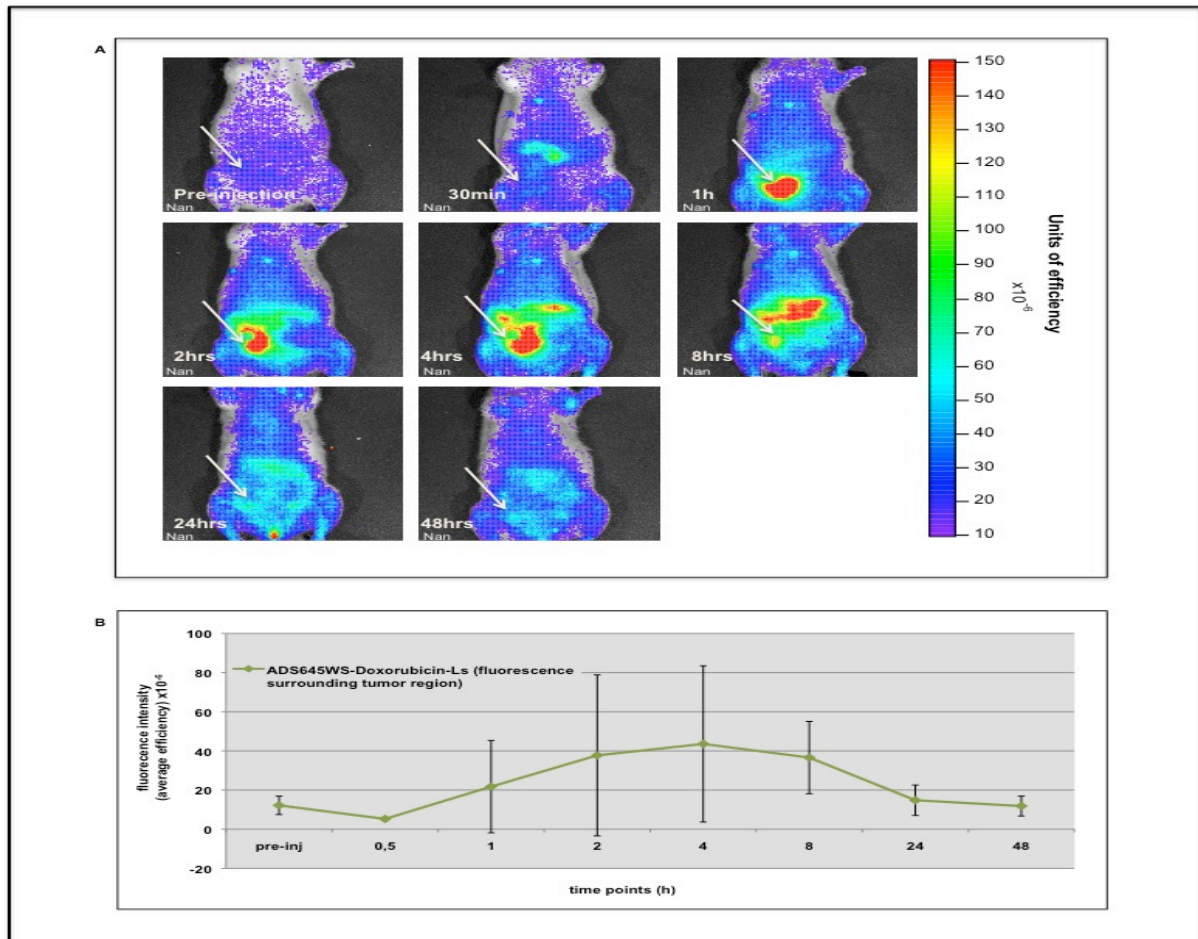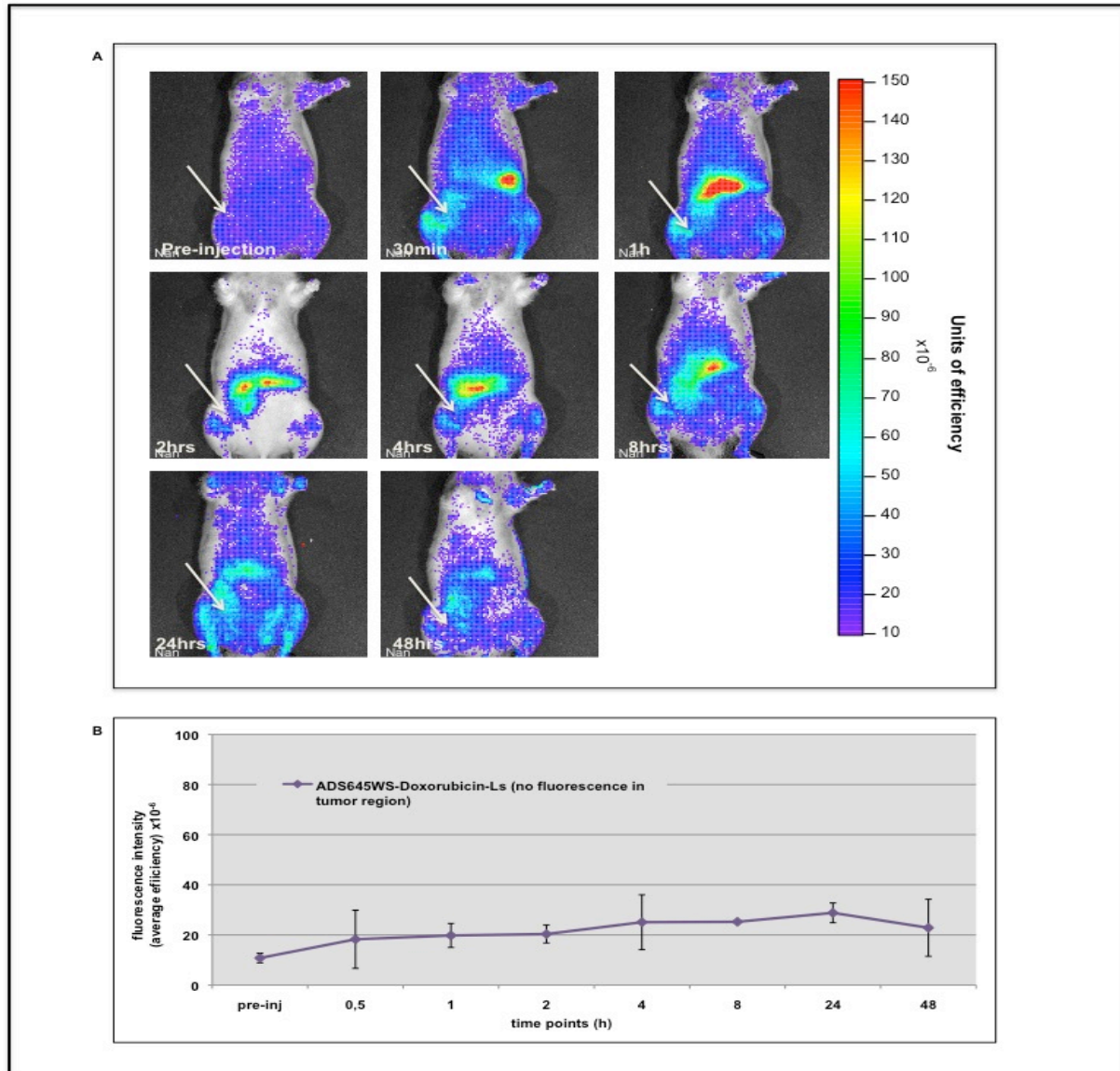

Figure 24: (A) Optical Imaging of the fluorescence signal intensity of an IGROV-1 injected rat after administration ADS645WS-Doxorubicin-Ls. Arrow indicates approximate tumor location (fluorescence in tumor region). The Cy5.5 filter set is used for excitation, emission and background subtraction. (B) A graph according to the regions of interest is drawn for each rat (n=3) at each time point. Fluorescence intensity (representing the average post-injection-pre-injection fluorescence) (Y-axis) is determined at each time point (X-axis). The fluorescence intensity is determined in units of efficiency; error bars represent standard deviation of the mean.

The second cohort, arbitrarily determined according to the fluorescent pattern projecting over the tumor region on the rats' right lower abdomen, concentrates on a fluorescent enhancement surrounding the tumor region of subcutaneously injected

IGROV-1 ovarian cancer cells. For rats 4 and 5, a fluorescent pattern begins to show at 1h post drug injection ($21,75 \times 10^{-6}$ +/- $23,59 \times 10^{-6}$). The fluorescent enhancement progressively changes in shape and intensity over a time span of 8 hours ($36,59 \times 10^{-6}$ +/- $18,47 \times 10^{-6}$) until no relevant signal is further traceable. Four hours post injection ($43,57 \times 10^{-6}$ +/- $39,90 \times 10^{-6}$) the fluorescence surrounding the tumor area is highest. No statistical data is acquired for this sub-cohort due to lack of subject quantity (n=2).

Figure 25: *(A) Optical Imaging of the fluorescence signal intensity of an IGROV-1 injected rat after administration ADS645WS-Doxorubicin-Ls. Arrow indicates approximate tumor location (fluorescence surrounding tumor region). The Cy5.5 filter set is used for excitation, emission and background subtraction. (B) A graph according to the regions of interest is drawn for each rat (n=2) at each time point. Fluorescence intensity (representing the average post-injection-pre-injection fluorescence) (Y-axis) is determined at each time point (X-axis). The fluorescence intensity is determined in units of efficiency; error bars represent standard deviation of the mean.*

For the third cohort, containing rats 6 and 7, imaging results show no coherent fluorescent enhancement, neither over the tumor region nor in the tissues surrounding the cancerous area. No statistical data is acquired for this sub-cohort due to lack of subject quantity (n=2).

Figure 26: *(A) Optical Imaging of fluorescence intensity of an IGROV-1 injected rat after administration ADS645WS-Doxorubicin-Ls. Arrow indicates approximate tumor location (no fluorescence in tumor region). The Cy5.5 filter set is used for excitation, emission and background subtraction. (B) A graph according to the regions of interest is drawn for each rat (n=2) at each time point. Fluorescence intensity (representing the average post-injection-pre-injection fluorescence) (Y-axis) is determined at each time point (X-axis). The fluorescence intensity is determined in units of efficiency; error bars represent standard deviation of the mean.*

4.3. Histology

4.3.1. Tumor specimen: data analysis

The three cohorts arbitrarily determined beforehand are kept identical for the analysis of the histopathological tumor slides.

The tumors of the rats injected with ADS645WS-Doxorubicin-Ls are explanted and processed for H&E stains.

The purpose is to correlate fluorescence intensity obtained with OI, with the vascularity pattern of these tumors. Based on the H&E stains and the OI images, a correlation scoring system is introduced using a fluorescence intensity score of the different OI images obtained as well as a vascularity score describing the vascularisation patterns of the tumor tissue.

The comparison of the data reveals the concordance of high fluorescence signal intensity and high microvessel density. According to the vascularity and fluorescence grading, the difference in the tumor fluorescence and tumor vascularity scores of the various animals is calculated and defined to a range of -2 to +2 where 0 is the correlation of the fluorescence signal intensity and the microvessel density. For n=4 animals a score of 0 is obtained, showing a concordance of high fluorescence signal intensity and high microvessel density as well as a low fluorescent signal in necrotic areas of tumor tissue.

Group	Fluorescence Score	Vascularity Score	Correlation Score
1	3	1	+2
	3	3	0
	3	3	0
2	2	1	+1
	2	1	+1
3	1	1	0
	1	1	0

Group 1- Fluorescence seen in tumor region
Group 2- Fluorescence seen in surrounding tumor region
Group 3- Minimal or no fluorescence in tumor or surrounding region

Fluorescence Score:
3= High tumor tissue fluorescence
2= Medium tumor/surrounding tissue fluorescence
1=Low tumor tissue fluorescence

Vascularity Score:
3= high microvessel density
2= Medium microvessel density, partly nectrotic areas
1=Low microvessel density, large necrotic areas

Table 3: Correlation of fluorescence intensity in Optical Imaging and histopathologically determined vascularisation of tumor tissue according to a scoring system.
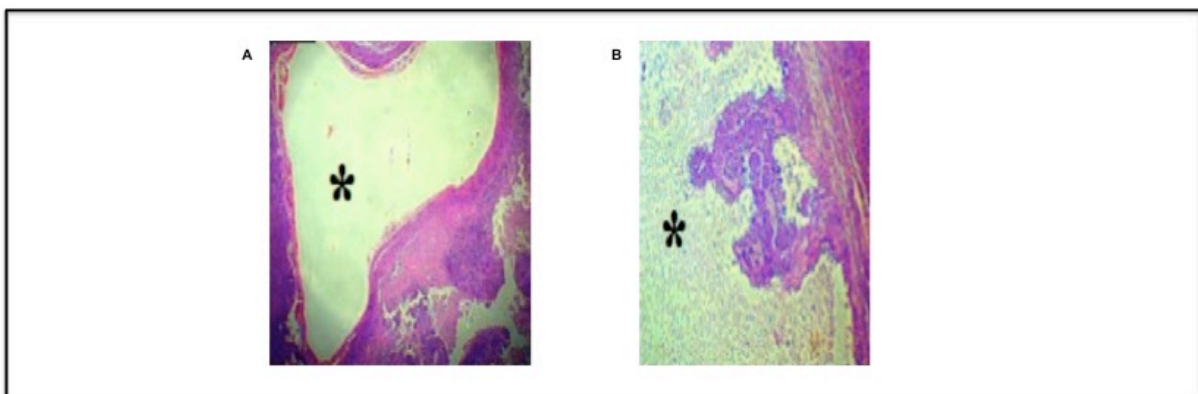
Figure 27: Addition to Table 3: Histologic slides of tumor tissue and its vascularity pattern.

(A)   H&E image of a single dominant central large vessel (*) in the tumor tissue.
(B)   H&E image of tumor tissue showing marked necrosis (*)

4.4. Statistical analysis

Statistical information is gathered for the ADS645WS-Doxorubicin-Lipsome group of the study. The results of the analysis are shown in *Table 4* for the *in vitro* dilution series and in *Table 5*, *Table 6* and *Table 7* for the *in vivo* experiments.

	control media (0µM)	1,562µM	3,125µM	6,2µM	12,5µM	25µM	50µM	100µM
Triplicate dilution series (ROIs)	$0,83 \times 10^{-6}$	$16,61 \times 10^{-6}$	$24,32 \times 10^{-6}$	$46,41 \times 10^{-6}$	$89,19 \times 10^{-6}$	$153,7 \times 10^{-6}$	$217,9 \times 10^{-6}$	$306,2 \times 10^{-6}$
	$0,52 \times 10^{-6}$	$11,86 \times 10^{-6}$	$23,67 \times 10^{-6}$	$44,61 \times 10^{-6}$	$91,38 \times 10^{-6}$	$159,2 \times 10^{-6}$	$224,5 \times 10^{-6}$	$306,9 \times 10^{-6}$
	$2,37 \times 10^{-6}$	$11,71 \times 10^{-6}$	$31,54 \times 10^{-6}$	$44,93 \times 10^{-6}$	$93,54 \times 10^{-6}$	$153,3 \times 10^{-6}$	$243,4 \times 10^{-6}$	$299,4 \times 10^{-6}$
p-value		0,0021	0,0006	$0,73 \times 10^{-6}$	$0,34 \times 10^{-6}$	$0,17 \times 10^{-6}$	$7,69 \times 10^{-6}$	$0,026 \times 10^{-6}$

Table 4*: In vitro statistical analysis: ADS645WS-Doxorubicin-Ls dilution series. The triplicate region of interest (n=3) of every concentration point is compared to the control triplicate region of interest (n=3).*

All the concentrations show a significantly higher fluorescent signal in comparison to the control wells.

ADS645WS-Doxorubicin-Liposome								
n=7								
Time points	Pre-injection	30min	1h	2h	4h	8h		24h
	$12,14 \times 10^{-6}$	$22,20 \times 10^{-6}$	$35,31 \times 10^{-6}$	$35,02 \times 10^{-6}$	$44,95 \times 10^{-6}$	$37,32 \times 10^{-6}$		$43,73 \times 10^{-6}$
	$9,42 \times 10^{-6}$	$35,88 \times 10^{-6}$	$25,83 \times 10^{-6}$	$27,24 \times 10^{-6}$	$26,77 \times 10^{-6}$	$34,71 \times 10^{-6}$		$35,46 \times 10^{-6}$
	$15,51 \times 10^{-6}$	$21,21 \times 10^{-6}$	$53,94 \times 10^{-6}$	$82,31 \times 10^{-6}$	$87,29 \times 10^{-6}$	$65,16 \times 10^{-6}$		$35,81 \times 10^{-6}$
	$8,86 \times 10^{-6}$	$13,64 \times 10^{-6}$	$13,93 \times 10^{-6}$	$17,48 \times 10^{-6}$	$24,21 \times 10^{-6}$	$32,39 \times 10^{-6}$		$18,18 \times 10^{-6}$
	$20,74 \times 10^{-6}$	$69,89 \times 10^{-6}$	$58,17 \times 10^{-6}$	$70,50 \times 10^{-6}$	$78,77 \times 10^{-6}$	$87,73 \times 10^{-6}$		$80,02 \times 10^{-6}$
	$25,30 \times 10^{-6}$	$56,14 \times 10^{-6}$	$55,97 \times 10^{-6}$	$53,94 \times 10^{-6}$	$83,58 \times 10^{-6}$	$94,06 \times 10^{-6}$		$98,67 \times 10^{-6}$
	$9,15 \times 10^{-6}$	$29,32 \times 10^{-6}$	$30,81 \times 10^{-6}$	$31,71 \times 0^{-6}$	$29,54 \times 10^{-6}$	$44,94 \times 10^{-6}$		$50,39 \times 10^{-6}$
p-value		0,0132	0,0015	0,0067	0,0042	0,0013		0,0046
n=3								
Time points	Pre-injection	30min	1h	2h	4h	8h	12h	24h
	$20,74 \times 10^{-6}$	$69,89 \times 10^{-6}$	$58,17 \times 10^{-6}$	$70,50 \times 10^{-6}$	$78,77 \times 10^{-6}$	$87,73 \times 10^{-6}$	$94,20 \times 10^{-6}$	$80,02 \times 10^{-6}$
	$25,30 \times 10^{-6}$	$56,14 \times 10^{-6}$	$55,97 \times 10^{-6}$	$53,94 \times 10^{-6}$	$83,58 \times 10^{-6}$	$94,06 \times 10^{-6}$	$87,46 \times 10^{-6}$	$98,67 \times 10^{-6}$
	$9,15 \times 10^{-6}$	$29,32 \times 10^{-6}$	$30,81 \times 10^{-6}$	$37,71 \times 10^{-6}$	$29,54 \times 10^{-6}$	$44,94 \times 10^{-6}$	$48,90 \times 10^{-6}$	$50,39 \times 10^{-6}$
p-value		0,0586	0,0225	0,0551	0,0686	0,0333	0,0275	0,0248

Table 5: *In vivo statistical analysis: the ratio of post-injection fluorescent signal intensity in tumor tissue at various time points in comparison to the pre-injection fluorescent signal intensity (FSI post-injection/pre-injection) is calculated for n=7 and n=3 animals.*

A significant fluorescent signal enhancement in comparison to the pre-injection image is delimitable for all acquired time points for n=7. For n=3, significant signal enhancements are found at the 1h (p < 0,03), 8h (p < 0,04), 12h (p < 0,03) and 24h (p < 0,03) image acquisitions.

ADS645WS-Doxorubicin-Liposome

n=7

Time points	Pre-injection	30min	1h	2h	4h	8h	24h
Tumor tissue (ROI 1)	$12,14 \times 10^{-6}$	$22,20 \times 10^{-6}$	$35,31 \times 10^{-6}$	$35,02 \times 10^{-6}$	$44,95 \times 10^{-6}$	$37,32 \times 10^{-6}$	$43,73 \times 10^{-6}$
	$9,42 \times 10^{-6}$	$35,88 \times 10^{-6}$	$25,83 \times 10^{-6}$	$27,24 \times 10^{-6}$	$26,77 \times 10^{-6}$	$34,71 \times 10^{-6}$	$35,46 \times 10^{-6}$
	$15,51 \times 10^{-6}$	$21,21 \times 10^{-6}$	$53,94 \times 10^{-6}$	$82,31 \times 10^{-6}$	$87,29 \times 10^{-6}$	$65,16 \times 10^{-6}$	$35,81 \times 10^{-6}$
	$8,86 \times 10^{-6}$	$13,64 \times 10^{-6}$	$13,93 \times 10^{-6}$	$17,48 \times 10^{-6}$	$24,21 \times 10^{-6}$	$32,39 \times 10^{-6}$	$18,18 \times 10^{-6}$
	$20,74 \times 10^{-6}$	$69,89 \times 10^{-6}$	$58,17 \times 10^{-6}$	$70,50 \times 10^{-6}$	$78,77 \times 10^{-6}$	$87,73 \times 10^{-6}$	$80,02 \times 10^{-6}$
	$25,30 \times 10^{-6}$	$56,14 \times 10^{-6}$	$55,97 \times 10^{-6}$	$53,94 \times 10^{-6}$	$83,58 \times 10^{-6}$	$94,06 \times 10^{-6}$	$98,67 \times 10^{-6}$
	$9,15 \times 10^{-6}$	$29,32 \times 10^{-6}$	$30,81 \times 10^{-6}$	$31,71 \times 0^{-6}$	$29,54 \times 10^{-6}$	$44,94 \times 10^{-6}$	$0,05038$
Control tissue (ROI 2)	$8,72 \times 10^{-6}$	$11,35 \times 10^{-6}$	$8,15 \times 10^{-6}$	$16,59 \times 10^{-6}$	$19,43 \times 10^{-6}$	$25,57 \times 10^{-6}$	$35,21 \times 10^{-6}$
	$10,43 \times 10^{-6}$	$15,10 \times 10^{-6}$	$14,92 \times 10^{-6}$	$18,70 \times 10^{-6}$	$20,81 \times 10^{-6}$	$26,43 \times 10^{-6}$	$31,97 \times 10^{-6}$
	$8,53 \times 10^{-6}$	$4,60 \times 10^{-6}$	$9,19 \times 10^{-6}$	$10,69 \times 10^{-6}$	$22,07 \times 10^{-6}$	$21,0 \times 10^{-6}$	$31,89 \times 10^{-6}$
	$7,85 \times 10^{-6}$	$5,69 \times 10^{-6}$	$4,71 \times 10^{-6}$	$8,22 \times 10^{-6}$	$8,85 \times 10^{-6}$	$3,51 \times 10^{-6}$	$4,68 \times 10^{-6}$
	$5,77 \times 10^{-6}$	$24,22 \times 10^{-6}$	$12,17 \times 10^{-6}$	$19,45 \times 10^{-6}$	$22,21 \times 10^{-6}$	$21,08 \times 10^{-6}$	$0,09 \times 10^{-6}$
	$10,78 \times 10^{-6}$	$19,29 \times 10^{-6}$	$18,47 \times 10^{-6}$	$29,0 \times 10^{-6}$	$17,42 \times 10^{-6}$	$4,12 \times 10^{-6}$	$29,3 \times 10^{-6}$
	$4,38 \times 10^{-6}$	$3,73 \times 10^{-6}$	$3,67 \times 10^{-6}$	$12,27 \times 10^{-6}$	$4,28 \times 10^{-6}$	$16,24 \times 10^{-6}$	$17,89 \times 10^{-6}$
p-value	0,0358	0,0040	0,0021	0,0167	0,0076	0,0121	0,0471

Table 6: *In vivo statistical analysis: comparison of ovarian tumor tissue (region of interest (ROI) 1) to control tissue (region of interest (ROI) 2) for the whole (n=7) ADS645WS-Doxorubicin-Lipsome group at various time points.*

ADS645WS-Doxorubicin-Liposome

n=3

Time points	Pre-injection	30min	1h	2h	4h	8h	12h	24h
Tumor tissue (ROI 1)	$20,74 \times 10^{-6}$	$69,89 \times 10^{-6}$	$58,17 \times 10^{-6}$	$70,50 \times 10^{-6}$	$78,77 \times 10^{-6}$	$87,73 \times 10^{-6}$	$94,20 \times 10^{-6}$	$80,02 \times 10^{-6}$
	$25,30 \times 10^{-6}$	$56,14 \times 10^{-6}$	$55,97 \times 10^{-6}$	$53,94 \times 10^{-6}$	$83,58 \times 10^{-6}$	$94,06 \times 10^{-6}$	$87,46 \times 10^{-6}$	$98,67 \times 10^{-6}$
	$9,15 \times 10^{-6}$	$29,32 \times 10^{-6}$	$30,81 \times 10^{-6}$	$37,71 \times 10^{-6}$	$29,54 \times 10^{-6}$	$44,94 \times 10^{-6}$	$48,90 \times 10^{-6}$	$50,39 \times 10^{-6}$
Control tissue (ROI 2)	$5,77 \times 10^{-6}$	$24,22 \times 10^{-6}$	$12,17 \times 10^{-6}$	$19,45 \times 10^{-6}$	$22,21 \times 10^{-6}$	$21,08 \times 10^{-6}$	$24,25 \times 10^{-6}$	$0,09 \times 10^{-6}$
	$10,78 \times 10^{-6}$	$19,29 \times 10^{-6}$	$18,47 \times 10^{-6}$	$29,0 \times 10^{-6}$	$17,42 \times 10^{-6}$	$4,12 \times 10^{-6}$	$7,02 \times 10^{-6}$	$29,3 \times 10^{-6}$
	$4,38 \times 10^{-6}$	$3,73 \times 10^{-6}$	$3,67 \times 10^{-6}$	$12,27 \times 10^{-6}$	$4,28 \times 10^{-6}$	$16,24 \times 10^{-6}$	$1,26 \times 10^{-6}$	$17,89 \times 10^{-6}$
p-value	0,0755	0,0250	0,0212	0,0780	0,0574	0,0743	0,0208	0,0519

Table 7: *In vivo statistical analysis: comparison of ovarian tumor tissue (region of interest (ROI) 1) to control tissue (region of interest (ROI) 2) for the arbitrarily determined ADS645WS-Doxorubicin-Lipsome sub-group at various time points.*

The comparison of ovarian cancer tissue (right flank) and control tissue (left flank) leads to significant differences in fluorescent behavior at each time point in the n=7 group (p < 0,05) (*Table 6*). For the n=3 sub-group, only the 30min, 1h and 12h (all p < 0,03) images show significant difference in fluorescent signal intensity in comparison to control tissue (*Table 7*).

5.   Discussion

In summary, this proof of principle study demonstrates that the accumulation of intravenously injected theranostic liposomes in tumor tissues can be evaluated *in vivo* with Optical Imaging (OI). Furthermore, our results show that the intensity of the fluorescence signal is dependent on the tumor's histopathologically evaluated vasculature pattern.

In recent years, nanoparticles have attracted significant interest in therapeutic cancer research because they offer an increased therapeutic efficacy and a reduced toxicity profile of the cytotoxic drugs due to a more selective drug delivery to its target structures (Bae *et al.*, 2011, Lopez-Davila *et al.*, 2012). One example of a successful nanocarrier design is a pegylated liposome encapsulating Doxorubicin. This FDA-approved liposomal formulation has been investigated in numerous studies (Gabizon *et al.*, 2003, Abraham *et al.*, 2005). It proved successful in clinical trials for several cancer types and showed significant improvements in pharmacokinetic profiles, tumor accumulation and reduction of toxicity when compared to free Doxorubicin (Lopez-Davila *et al.*, 2012). However, the efficacy of liposomal anthracyclines (like Doxorubicin) could not yet be reproduced by liposomal formulations containing other anticancer drug classes. Indeed, anthracyclines can easily be stably encapsulated in the liposome interior using remote-loading methodologies giving rise to stable liposomal formulations that have been difficult to replicate with other classes of drugs (Drummond *et al.*, 2006). Drummond et al. have designed a nanoliposomal Irinotecan using a new loading technique. An unprecedented drug loading efficiency has lead to a markedly superior efficacy in combination with a lower toxicity profile when compared with free Irinotecan in human breast and colon cancer xenograft models (Drummond *et al.*, 2006). The liposomal formulation investigated in this study is capable of encapsulating Doxorubicin and was designed according to the new loading technique used by Drummond et al. It enables a high drug-to-lipid ratio, thus having high and stable cytotoxic drug concentrations per nanoparticle. Moreover, its stability will not be guaranteed for anthracyclines only, but can be transferred to many different cytotoxic agents in future studies. We propose to use it as an approved carrier for cytotoxic drugs in cancer treatment.

Making use of the previously described enhanced permeability and retention effect, Serwer et al. designed a non-targeted liposomal Topotecan in a glioblastoma xenograft mouse model. Analysis of intracranial tumors demonstrated increased activation of cleaved caspase-3 and DNA fragmentation. Relying on the EPR effect, both are indicators of response to treatment (Serwer *et al.*, 2011). Other studies investigating non-targeted nanocarriers making use of the EPR effect consist mostly of pegylated liposomes; generally the FDA-approved Doxil® (Gabizon, 1994, Torchilin, 2005, Duggan, Keating, 2011). However, Muggia et al., as well as numerous other publications on Doxil® (Ranson *et al.*, 1997, Drummond *et al.*, 1999, Lopez-Davila *et al.*, 2012), mention the hand-foot syndrome as dose limiting in studies conducted with pegylated Doxorubicin in ovarian and breast cancer (Muggia, 1997). The nanoliposomal formulation used in this study relies on the EPR effect to deliver Doxorubicin at its target site. This is in accordance with current practice and clinical relevance (Lopez-Davila *et al.*, 2012). Moreover, the liposomal formulation used is not pegylated, thus circumventing the dose limitation caused by palmar-plantar erythrodysesthesia.

Other than relying on the EPR-induced passive accumulation of liposomes and release of drugs at tumor site, more specific, targeted nanoparticles are contributing to promising therapeutic approaches in cancer treatment (Bae *et al.*, 2011). These include molecules conjugated with folic acid (Lu, Low, 2002) or anti-HER2 liposomes (Park *et al.*, 2002, Kirpotin *et al.*, 2006). Moreover, the recent development of nanosized delivery vehicles for small interfering RNA (siRNA) has been used by Godin et al. to design a multistage vector system to effectively transport siRNA, targeted against EphA2 oncoprotein, to various tumor tissues including ovarian cancer (Godin *et al.*, 2011). The advantage of these molecules consists in their targeted approach to various oncogenic alterations, thus reaching tumor cells even more effectively. However, the above-mentioned chemotherapeutic agents are currently under investigation only in cases with *de novo* or acquired chemotherapy resistance (Chen *et al.*, 2010), and are as such currently not a routine treatment option for newly diagnosed or progressive ovarian cancer. In contrast to the above-mentioned investigations, this study aimed at supervising an already established chemotherapeutic regimen to treat ovarian cancer. For this, we designed a non-

pegylated liposomal nanovehicle able to (i) deliver Doxorubicin at tumor sites and (ii) to trace it with Optical Imaging.

Indeed, in addition to designing a mere drug delivering nanoparticle, we developed a carrier co-encapsulated with Doxorubicin as therapeutic agent as described above as well as a near-infrared fluorophore as diagnostic agent to monitor the effective accumulation of the nanocarrier and its content at the tumor site. The recent development of these multi-functional so-called theranostic nanosystems enables the efficient delivery of drugs to tumors while simultaneously monitoring their therapeutic response by visualizing tumor cells (Nie *et al.*, 2007, Salvador-Morales *et al.*, 2009). So far, only few publications have concentrated on a non-targeted experimental setup, evaluating the passive accumulation of the theranostic agent at the tumor site. Kim et al. have reported the development of multi-functional polymeric nanoparticles embedded with iron oxide nanoparticles and Doxorubicin, leading to an efficient delivery of drug to cancer cells and showing high MRI contrast (Kim *et al.*, 2008b). Similarly, Vigilanti et al. have demonstrated the feasibility of tracing nanocarriers which encapsulated both Doxorubicin and manganese sulfate ($MnSO_4$) with MRI (Viglianti *et al.*, 2006). However, different from our experimental setup, these studies rely solely on MRI to trace the designed nanoparticle. Although it allows high spatial resolution and radiation-free imaging, it gathers less sensitive images and requires more expensive and long-winded data acquisition in comparison to Optical Imaging. Moreover, a major issue with the current metallic or inorganic nanoparticles used in the above-described MRI studies is the high risk of toxicity associated with their long-term residence in body without degradation (Yu *et al.*, 2008). The theranostic nanoparticle designed in this study uses the NIR fluorophore ADS645WS as diagnostic component to enable the nanoparticle's tracking with Optical Imaging. In comparison to the above-mentioned MRI studies, the advantage of this diagnostic agent is its organic nature, minimizing intrinsic toxicity, unlike other theranostic nanocarriers as described previously (Lopez-Davila *et al.*, 2012).

ADS645WS is a water-soluble, organic particle that has been used by Kirpotin et al. to measure the extent of *in vivo* uptake of liposomes of a non-targeted control group in a study conducted to evaluate Anti-HER2 immunoliposomes designed to achieve targeted intracellular delivery to HER2-overexpressing tumor cells (Kirpotin *et al.*,

2006). However, to the best of our knowledge, ADS645WS has not yet been used as tracking agent for *in vivo* Optical Imaging in previous studies. Indeed, in the study conducted by Kirpotin et al, flow cytometry was used to quantitate the fluorophore in tumor tissue *ex vivo.* With its excitation and emission profiles in the NIR spectrum (Ex.: 654nm and Em.: 660nm), ADS645WS is well suited to enable tracing of nanocarriers with Optical Imaging. This is in accordance with various OI studies, where the aforementioned wavelength range enables a satisfying depth penetration as a result of the inherent low tissue absorption (Ntziachristos *et al.*, 2003, Sutton *et al.*, 2008).

As mentioned previously, the theranostic nanoparticle designed in this study was readily detectable with Optical Imaging, thus allowing for the use of an emerging imaging modality scoring with a very sensitive, relatively inexpensive, fast and radiation-free, longitudinal data acquisition (Sutton *et al.*, 2008). The use of Optical Imaging as a monitoring device for the efficient delivery of cells, drugs or nanoparticles in cancer therapy has been implemented successfully over the past years (Licha, Olbrich, 2005). For example, Tavri et al. were able to trace fluorophore labeled, tumor-targeted natural killer cells to human prostate cancer (Tavri *et al.*, 2009), Sutton et al. showed that labeling of hMSCs with DiD provides effective cell depiction with OI *in vitro* and *in vivo (*Sutton *et al.*, 2009*)*. Different to the above-mentioned studies, the traced agent used here was not targeted to any specific cells but consisted only of a liposomal Doxorubicin as first-line therapy for progressive ovarian cancer, relying on the passive accumulation in tumor tissue.

Up until now, only few studies have evaluated the potential of Optical Imaging for the detection and treatment monitoring of ovarian cancer. Martinez-Poveda et al. have used a bioluminescent reporter construct containing 9xHRE-luciferase to non-invasively monitor functional changes in HIF activity in response to antiangiogenic treatment in a xenograft model of human ovarian carcinoma (Martinez-Poveda *et al.*, 2011). This provides a higher sensitivity compared with fluorescence imaging but requires more extensive transduction methods. A model of disseminated peritoneal ovarian cancer has been designed to investigate the use of ICG as optical probe for the real-time endoscopic detection of tiny ovarian cancer peritoneal implants (Kosaka *et al.*), showing promising data on the combination of endoscopic diagnostics and

fluorescence imaging but requiring invasive methods such as laparoscopy to pursue information gathering. In comparison to the above-mentioned theranostic investigations, the nanovehicle used in this study has proven to be non-invasively effectively traceable with Optical Imaging in an *in vivo* ovarian cancer xenograft model.

The images gathered with Optical Imaging were compared with histopathology. The fluorescence enhancement correlated with the histopathologically obtained vasculature pattern. Indeed tumor blood supply and perfusion, which play an important role in its growth potential and survival, are also required to enable drug circulation into cancerous tissue (Bergers, Benjamin, 2003, Minchinton, Tannock, 2006). Moreover, solid tumors are often not readily accessible for therapeutic or imaging agents due to their distance from the supporting vasculature that provides the entrance point for the pool of available therapeutic agents (Drummond *et al.*, 2008). In accordance with this information, tumors, in our study, which showed no fluorescent signal, were histopathologically characterized by widespread necrotic tumor tissue and only a minimal vascular supply. ADS645WS-Doxorubicin-Ls, injected intravenously could probably not reach the cancerous area, thus explaining the low enhancement pattern. Another cohort showed marked fluorescence enhancement over the whole cancerous expanse as well as a histologically defined strong vascular structure, assuring the adequate blood supply and in turn ADS645WS-Doxorubicin-Ls delivery to target tissue. The fluorescent signal in this group was distinctly captured with Optical Imaging.

Interestingly, fluorescent signal intensity was already detectable at the pre-injection time point baseline image in a certain amount of animals, arising from autofluorescence of animal tissue. This observation was, at least in part, in conflict with accepted knowledge since OI in the NIR spectrum has the advantage of minimizing tissue autofluorescence (Sutton *et al.*, 2008). This might have been caused by a variation in fluorescent behavior due to tumor necrosis before dye injection. Indeed, strong fluorescent signal intensity over tumor tissue was obtained for the ADS645WS-Doxorubicin-Ls sub-group (n=3).

Several limitations of the study need to be considered. As this was a proof of principle study, it was only justifiable to use a small animal number leading to a reduced statistical significance.

Kirpotin et al. have demonstrated that antibody targeting does not increase accumulation of long-circulating nanoparticles in tumor tissue in comparison to non-targeted nanocarriers, but rather increases mediated intracellular drug delivery to cancer cells in animal models. This was confirmed with high-power magnification microscopy where immunoliposomes were distributed throughout tumor tissue in close association with tumor cells, whereas non-targeted liposomes showed a more uneven or patchy distribution, with high focal accumulation within tumor stroma and less association with tumor cells (Kirpotin *et al.*, 2006). The nanocarrier designed in our study uses a non-targeted approach relying solely on the EPR-effect. Hence, taking the insights of Kirpotin et al. into account, it is probable that Doxorubicin transported by our liposomal formulation, even though accumulating at tumor site, might not be taken up into tumor cells. However, the purpose of this study was primarily to show the feasibility of tracking the designed nanocarrier with Optical Imaging. This was demonstrated to be feasible, thus we developed a method allowing a non-invasive surveillance of tumor tissue with Optical Imaging. We acknowledge that long-term follow-up data about the therapeutic efficiency of the theranostic probe used here was not acquired for the above-described reasons making additional studies necessary.

Moreover, due to the realization of the above-mentioned correlation of histopathological samples with imaging data, long-term data concerning the therapeutic efficiency and pharmacokinetics of the new nanocarrier would have to be gathered in a future study setup.

In addition, due to the time and cost-intensive development of the theranostic agent, only few animals could be injected. A larger sample size could provide further information on the general pharmacokinetics and tumor delivery of this particular probe. In a preliminary study, where only the fluorophore was encapsulated into the nanocarrier, strong fluorescent signals were obtained with the Optical Imager. The consistent fluorescent signal traceable with Optical Imaging, even after co-

encapsulation of the fluorophore with Doxorubicin appears promising that we were able to design a stable theranostic nanocarrier, although additional studies are also required here. In addition, in some animals a strong fluorescent signal appears over the intestines and liver. This is probably due to the uptake of a significant part of the liposomal nanocarrier by the reticulo-endothelial system (RES). In other studies, one of the reasons for "pegylating" the nanocarriers is the reduced uptake by the reticulo-endothelial system through reduced opsonization. However, the release of the nanocarrier's contents at target site and consequently the cellular uptake are also decreased (Drummond *et al.*, 1999). As mentioned before, additional studies are required to optimize the pharmacokinetics of the here designed nanocarrier, also with regard to the RES uptake. However, in this study the subcutaneously localized ovarian tumors were clearly visible and thus statements about fluorescent signal with Optical Imaging could nevertheless be made.

Since the purpose of this study was to gather functional information about the newly designed theranostic agent, the Optical Imaging method we used, which has a relatively simple instrumentation to image fluorescence emission light from a surface (two-dimensional) was sufficient for this particular study design. Indeed, tissue reflectance imaging is high resolution and fast, but because of multiple light scattering, sensitivity is limited by light penetrance, and contrast is derived primarily from superficial structures, typically up to approximately 3 mm in depth. To create a more clinically relevant setting of existing established theranostic agents, the use of a Tomographic Optical Imager is being evaluated because it offers better resolution (Ntziachristos *et al.*, 2003). Moreover, newer studies combine Optical Imaging with MRI synergistically to overcome their respective disadvantages simultaneously. Thus, although magnetic resonance imaging has the advantage of three-dimensional resolution and visualization of overall anatomic background, it lacks sensitivity. Optical imaging methods provide high target sensitivity, although they lack three-dimensional resolution as mentioned above (Chen *et al.*, 2010). This was not necessary in our proof of principle study setup.

Finally, the fluorescent dye used in this study is not FDA-approved. Until now, the only clinically available NIR fluorophore is indocyanine green (ICG) (Ogawa *et al.*, 2009). Even though clinical translation is therefore not possible up until now, the

designed theranostic agent and especially its fluorophore component might be useful for further preclinical study developments.

In summary the results of this study show that accumulation of intravenously injected theranostic liposomes in tumor tissues can be evaluated *in vivo* with Optical Imaging (OI). Although technical advances have been achieved in many areas of diagnostic radiology, the detection of human cancer remains challenging. The technique of Optical Imaging is a very promising imaging modality since it enables the generation of highly sensitive images within seconds using relatively inexpensive equipment (Frangioni, 2008, Sutton *et al.*, 2008). Moreover, the emerging field of theranostic agents as the one used in this study might encourage further investigations of clinical theranostic probes. This may be used to develop improved tumor drug delivery strategies, accelerate the development of new therapeutics, facilitate drug dose optimization and ultimately, allow for individualized treatment selection and monitoring.

6.   Summary

Purpose: The purpose of the main branch of this study was to determine, whether tumor accumulation of intravenously injected theranostic liposomes (Ls), co-encapsulated with a near-infrared (NIR) dye and Doxorubicin (DOX), can be tracked *in vivo* with Optical Imaging (OI).

Materials & Methods: Nano-liposomes (size: 80-120nm) were loaded with a water-soluble NIR dye (ADS645WS, Excitation.:641nm/Emission.:661nm) and DOX, purified by gel filtration and evaluated *in vitro* with OI. Then, 7 athymic nude rats with implanted human IGROV ovarian cancers received intravenous injections of ADS645WS-DOX-Ls (11,01mM phospholipid (PL) and 7,5mg DOX/kg) and underwent OI before and at 30min, 1h, 2h, 4h, 8h and 24h post-injection. Tumor fluorescence on OI was compared for significant differences between pre- and postcontrast data and fluorescence enhancement was compared between tumor and normal muscle as an internal standard, using a t-test and a p<0,05. Results were correlated with histopathology.

Results: ADS645WS-DOX-Ls showed a strong *in vitro* fluorescence, which increased with ADS645WS concentration (p<0,05). *In vivo*, ADS645WS-DOX-Ls injection caused a significantly increased fluorescence of ovarian tumors on post-contrast scans compared to pre-contrast scans (p<0,05), with a peak at 8 hours post-injection. All tumors also showed significantly higher fluorescent signal intensity in comparison to control tissue. The degree of tumor enhancement on OI scans showed a large variability, which correlated with tumor vascularity on histopathology.

Conclusion: Tumor accumulation of intravenously injected theranostic liposomes can be evaluated *in vivo* with Optical Imaging (OI).

Clinical relevance/application: Optical Imaging can facilitate monitoring chemotherapeutic agent accumulation in tumor tissue and therapeutic response in oncologic treatment dose. Moreover, dose optimization in tumor models may be achieved, thus potentially accelerating the development process and potentially allowing for the optimization of individualized therapy.

7. List of References

Abraham, S. A., Waterhouse, D. N., Mayer, L. D., Cullis, P. R., Madden, T. D., Bally, M. B.
The liposomal formulation of doxorubicin
Methods Enzymol 391 (2005) 71-97

Allen, T. M., Cheng, W. W., Hare, J. I., Laginha, K. M.
Pharmacokinetics and pharmacodynamics of lipidic nano-particles in cancer
Anticancer Agents Med Chem 6 (2006) 513-523

Asadollahi, R., Hyde, C. A., Zhong, X. Y.
Epigenetics of ovarian cancer: From the lab to the clinic
Gynecol Oncol 118 (2010) 81-87

Aslam, N., Banerjee, S., Carr, J. V., Savvas, M., Hooper, R., Jurkovic, D.
Prospective evaluation of logistic regression models for the diagnosis of ovarian cancer
Obstet Gynecol 96 (2000) 75-80

Bae, K. H., Chung, H. J., Park, T. G.
Nanomaterials for cancer therapy and imaging
Mol. Cells 31 (2011) 295-302

Balch, C., Fang, F., Matei, D. E., Huang, T. H., Nephew, K. P.
Minireview: Epigenetic changes in ovarian cancer
Endocrinology 150 (2009) 4003-4011

Barentsz, J.
Mr in the evaluation of gynecologic tumor
J. Belge Radiol. 78 (1995) 305-307

Bast, R. C., Jr., Hennessy, B., Mills, G. B.
The biology of ovarian cancer: New opportunities for translation
Nat Rev Cancer 9 (2009) 415-428

Basu, S., Li, G., Alavi, A.
Pet and pet-ct imaging of gynecological malignancies: Present role and future promise
Expert Rev Anticancer Ther 9 (2009) 75-96

Bergers, G., Benjamin, L. E.
Tumorigenesis and the angiogenic switch
Nat Rev Cancer 3 (2003) 401-410

Berry, G., Billingham, M., Alderman, E., Richardson, P., Torti, F., Lum, B., Patek, A., Martin, F. J.
The use of cardiac biopsy to demonstrate reduced cardiotoxicity in aids kaposi's sarcoma patients treated with pegylated liposomal doxorubicin
Ann Oncol 9 (1998) 711-716

Bornhop, D. J., Contag, C. H., Licha, K., Murphy, C. J.
Advance in contrast agents, reporters, and detection
J Biomed Opt 6 (2001) 106-110

Bouchard, M. B., MacLaurin, S. A., Dwyer, P. J., Mansfield, J., Levenson, R., Krucker, T.
Technical considerations in longitudinal multispectral small animal molecular imaging
J Biomed Opt 12 (2007) 051601

Bouma, J., Beijnen, J. H., Bult, A., Underberg, W. J.
Anthracycline antitumour agents. A review of physicochemical, analytical and stability properties
Pharm Weekbl Sci 8 (1986) 109-133

Bremer, C., Ntziachristos, V., Weissleder, R.
Optical-based molecular imaging: Contrast agents and potential medical applications
Eur Radiol 13 (2003) 231-243

Bremer, C., Tung, C. H., Weissleder, R.
In vivo molecular target assessment of matrix metalloproteinase inhibition
Nat. Med. 7 (2001) 743-748

Bressolle, F., Jacquet, J. M., Galtier, M., Jourdan, J., Donadio, D., Rossi, J. F.
Doxorubicin and doxorubicinol plasma concentrations and excretion in parotid saliva
Cancer Chemother Pharmacol 30 (1992) 215-218

Budavari, S.
The merck index
In "The merck index", M. a. Co., Rahway, NJ, 2000, 541

Bulte, J. W., Ma, L. D., Magin, R. L., Kamman, R. L., Hulstaert, C. E., Go, K. G., The, T. H., de Leij, L.
Selective mr imaging of labeled human peripheral blood mononuclear cells by liposome mediated incorporation of dextran-magnetite particles
Magn Reson Med 29 (1993) 32-37

Campbell, R. B., Fukumura, D., Brown, E. B., Mazzola, L. M., Izumi, Y., Jain, R. K., Torchilin, V. P., Munn, L. L.
Cationic charge determines the distribution of liposomes between the vascular and extravascular compartments of tumors
Cancer Res 62 (2002) 6831-6836

Cannistra, S. A.
Is there a "Best" Choice of second-line agent in the treatment of recurrent, potentially platinum-sensitive ovarian cancer?
J Clin Oncol 20 (2002) 1158-1160

Cannistra, S. A.
Cancer of the ovary
N Engl J Med 351 (2004) 2519-2529

Carlson, K. J., Skates, S. J., Singer, D. E.
Screening for ovarian cancer
Ann Intern Med 121 (1994) 124-132

Cay, O., Kruskal, J. B., Nasser, I., Thomas, P., Clouse, M. E.
Liver metastases from colorectal cancer: Drug delivery with liposome-encapsulated doxorubicin
Radiology 205 (1997) 95-101

Chen, W., Bardhan, R., Bartels, M., Perez-Torres, C., Pautler, R. G., Halas, N. J., Joshi, A.
A molecularly targeted theranostic probe for ovarian cancer
Mol Cancer Ther 9 (2010) 1028-1038

Chobanian, J. V., Tall, A. R., Brecher, P. I.
Interaction between unilamellar egg yolk lecithin vesicles and human high density lipoprotein
Biochemistry 18 (1979) 180-187

Choy, G., Choyke, P., Libutti, S. K.
Current advances in molecular imaging: Noninvasive in vivo bioluminescent and fluorescent optical imaging in cancer research
Mol Imaging 2 (2003) 303-312

Chu, E., Sartorelli, A. C.
Cancer chemotherapy
In "Bertram g. Katzung: Basic and clinical pharmacology", L. M. B. M.-H. M. P. Division, Lange Medical Books/ McGraw-Hill, USA, 2003, 9, 913-914

Citrin, D., Camphausen, K.
Optical imaging of mice in oncologic research
Expert Rev Anticancer Ther 4 (2004) 857-864

Citrin, D., Lee, A. K., Scott, T., Sproull, M., Menard, C., Tofilon, P. J., Camphausen, K.
In vivo tumor imaging in mice with near-infrared labeled endostatin
Mol Cancer Ther 3 (2004) 481-488

Costamagna, G., Marchese, M.
Progress in endoscopic imaging of gastrointestinal tumors
Eur. Rev. Med. Pharmacol. Sci. 14 (2010) 272-276

Drummond, D. C., Meyer, O., Hong, K., Kirpotin, D. B., Papahadjopoulos, D.
Optimizing liposomes for delivery of chemotherapeutic agents to solid tumors
Pharmacol Rev 51 (1999) 691-743

Drummond, D. C., Noble, C. O., Guo, Z., Hong, K., Park, J. W., Kirpotin, D. B.
Development of a highly active nanoliposomal irinotecan using a novel intraliposomal
stabilization strategy
Cancer Res 66 (2006) 3271-3277

Drummond, D. C., Noble, C. O., Hayes, M. E., Park, J. W., Kirpotin, D. B.
Pharmacokinetics and in vivo drug release rates in liposomal nanocarrier
development
J Pharm Sci 97 (2008) 4696-4740

Duggan, S. T., Keating, G. M.
Pegylated liposomal doxorubicin: A review of its use in metastatic breast cancer,
ovarian cancer, multiple myeloma and aids-related kaposi's sarcoma
Drugs 71 (2011) 2531-2558

Edinger, M., Sweeney, T. J., Tucker, A. A., Olomu, A. B., Negrin, R. S., Contag, C. H.
Noninvasive assessment of tumor cell proliferation in animal models
Neoplasia 1 (1999) 303-310

Erdogan, S., Roby, A., Sawant, R., Hurley, J., Torchilin, V. P.
Gadolinium-loaded polychelating polymer-containing cancer cell-specific
immunoliposomes
J Liposome Res 16 (2006) 45-55

Fiallo, M. M., Garnier-Suillerot, A., Matzanke, B., Kozlowski, H.
How fe3+ binds anthracycline antitumour compounds. The myth and the reality of a
chemical sphinx
J Inorg Biochem 75 (1999) 105-115

Fiallo, M. M., Tayeb, H., Suarato, A., Garnier-Suillerot, A.
Circular dichroism studies on anthracycline antitumor compounds. Relationship
between the molecular structure and the spectroscopic data
J Pharm Sci 87 (1998) 967-975

Frangioni, J. V.
New technologies for human cancer imaging
J Clin Oncol 26 (2008) 4012-4021

Fung-Kee-Fung, M., Oliver, T., Elit, L., Oza, A., Hirte, H. W., Bryson, P.
Optimal chemotherapy treatment for women with recurrent ovarian cancer
Curr Oncol 14 (2007) 195-208

Gabizon, A., Shmeeda, H., Barenholz, Y.
Pharmacokinetics of pegylated liposomal doxorubicin: Review of animal and human
studies
Clin Pharmacokinet 42 (2003) 419-436

Gabizon, A. A.
Selective tumor localization and improved therapeutic index of anthracyclines encapsulated in long-circulating liposomes
Cancer Res 52 (1992) 891-896

Gabizon, A. A.
Liposomal anthracyclines
Hematol Oncol Clin North Am 8 (1994) 431-450

Gabizon, A. A.
Pegylated liposomal doxorubicin: Metamorphosis of an old drug into a new form of chemotherapy
Cancer Invest 19 (2001) 424-436

Godin, B., Tasciotti, E., Liu, X., Serda, R. E., Ferrari, M.
Multistage nanovectors: From concept to novel imaging contrast agents and therapeutics
Acc Chem Res 44 (2011) 979-989

Goff, B. A., Matthews, B. J., Larson, E. H., Andrilla, C. H., Wynn, M., Lishner, D. M., Baldwin, L. M.
Predictors of comprehensive surgical treatment in patients with ovarian cancer
Cancer 109 (2007) 2031-2042

Gotlieb, W. H., Baruch, G. B., Friedman, E.
Prophylactic oophorectomy: Clinical considerations
Semin Surg Oncol 19 (2000) 20-27

Grahek, D., Hassan-Sebbag, N.
[metabolic imaging with positron-emission tomography in the advanced-stage ovarian cancers]
Bull Cancer 96 (2009) 1163-1171

Graves, D. E., Krugh, T. R.
Adriamycin and daunorubicin bind in a cooperative manner to deoxyribonucleic acid
Biochemistry 22 (1983) 3941-3947

Gregoriadis, G.
Targeting of drugs: Implications in medicine
Lancet 2 (1981) 241-246

Gruber, B. M., Anuszewska, E. L., Bubko, I., Gozdzik, A., Priebe, W., Fokt, I.
Relationship between topoisomerase ii-DNA cleavable complexes, apoptosis and cytotoxic activity of anthracyclines in human cervix carcinoma cells
Anticancer Res 25 (2005) 2193-2198

Gustafson, D. L., Rastatter, J. C., Colombo, T., Long, M. E.
Doxorubicin pharmacokinetics: Macromolecule binding, metabolism, and excretion in the context of a physiologic model
J Pharm Sci 91 (2002) 1488-1501

Hashida, M., Nishikawa, M., Yamashita, F., Takakura, Y.
Cell-specific delivery of genes with glycosylated carriers
Adv Drug Deliv Rev 52 (2001) 187-196

Hashizume, H., Baluk, P., Morikawa, S., McLean, J. W., Thurston, G., Roberge, S., Jain, R. K., McDonald, D. M.
Openings between defective endothelial cells explain tumor vessel leakiness
Am J Pathol 156 (2000) 1363-1380

Hassan, M., Klaunberg, B. A.
Biomedical applications of fluorescence imaging in vivo
Comp Med 54 (2004) 635-644

Heeremans, J. L., Prevost, R., Bekkers, M. E., Los, P., Emeis, J. J., Kluft, C., Crommelin, D. J.
Thrombolytic treatment with tissue-type plasminogen activator (t-pa) containing liposomes in rabbits: A comparison with free t-pa
Thromb. Haemost. 73 (1995) 488-494

Hennessy, B. T., Murph, M., Nanjundan, M., Carey, M., Auersperg, N., Almeida, J., Coombes, K. R., Liu, J., Lu, Y., Gray, J. W., Mills, G. B.
Ovarian cancer: Linking genomics to new target discovery and molecular markers-- the way ahead
Adv Exp Med Biol 617 (2008) 23-40

Ilekis, J. V., Connor, J. P., Prins, G. S., Ferrer, K., Niederberger, C., Scoccia, B.
Expression of epidermal growth factor and androgen receptors in ovarian cancer
Gynecol Oncol 66 (1997) 250-254

Jain, R. K.
Barriers to drug delivery in solid tumors
Sci. Am. 271 (1994) 58-65

Jemal, A., Siegel, R., Ward, E., Hao, Y., Xu, J., Thun, M. J.
Cancer statistics, 2009
CA Cancer J Clin 59 (2009) 225-249

Johnston, M. J., Semple, S. C., Klimuk, S. K., Ansell, S., Maurer, N., Cullis, P. R.
Characterization of the drug retention and pharmacokinetic properties of liposomal nanoparticles containing dihydrosphingomyelin
Biochim Biophys Acta 1768 (2007) 1121-1127

Johnston, M. J., Semple, S. C., Klimuk, S. K., Edwards, K., Eisenhardt, M. L., Leng, E. C., Karlsson, G., Yanko, D., Cullis, P. R.
Therapeutically optimized rates of drug release can be achieved by varying the drug-to-lipid ratio in liposomal vincristine formulations
Biochim Biophys Acta 1758 (2006) 55-64

Katsumata, N., Yasuda, M., Takahashi, F., Isonishi, S., Jobo, T., Aoki, D., Tsuda, H., Sugiyama, T., Kodama, S., Kimura, E., Ochiai, K., Noda, K.
Dose-dense paclitaxel once a week in combination with carboplatin every 3 weeks for advanced ovarian cancer: A phase 3, open-label, randomised controlled trial
Lancet 374 (2009) 1331-1338

Kiechle, M.
Gynäkologie und Geburtshilfe
Elsevier, Munich, 2006, 1, 541-542

Kim, J., Lee, J., Lee, S., Yu, J., Lee, J., Park, T., Hyeon, T.
Designed fabrication of a multifunctional polymer nanomedical platform for simultaneous cancer- targeted imaging and magnetically guided drug delivery
Advanced Materials 20 (2008b) 478–483

Kirpotin, D. B., Drummond, D. C., Shao, Y., Shalaby, M. R., Hong, K., Nielsen, U. B., Marks, J. D., Benz, C. C., Park, J. W.
Antibody targeting of long-circulating lipidic nanoparticles does not increase tumor localization but does increase internalization in animal models
Cancer Res 66 (2006) 6732-6740

Kisel, M. A., Kulik, L. N., Tsybovsky, I. S., Vlasov, A. P., Vorob'yov, M. S., Kholodova, E. A., Zabarovskaya, Z. V.
Liposomes with phosphatidylethanol as a carrier for oral delivery of insulin: Studies in the rat
Int. J. Pharm. 216 (2001) 105-114

Kosaka, N., Mitsunaga, M., Longmire, M. R., Choyke, P. L., Kobayashi, H.
Near infrared fluorescence-guided real-time endoscopic detection of peritoneal ovarian cancer nodules using intravenously injected indocyanine green
Int. J. Cancer 129 1671-1677

Kumar, V., Abbas, A., Fausto, N., Aster, J.
Robbins and cotrane: Pathologic basis of disease
Elsevier, Philadelphia, 2010, 8, 1040

Lakowicz, J. R.
Principles of fluorescence
Springer Science & Business Media, New York, 2010, 4, 5

Largueze, J. B., Kirat, K. E., Morandat, S.
Preparation of an electrochemical biosensor based on lipid membranes in nanoporous alumina
Colloids Surf B Biointerfaces 79 (2010) 33-40

Lasic, D. D., Ceh, B., Stuart, M. C., Guo, L., Frederik, P. M., Barenholz, Y.
Transmembrane gradient driven phase transitions within vesicles: Lessons for drug delivery
Biochim Biophys Acta 1239 (1995) 145-156

Licha, K., Olbrich, C.
Optical imaging in drug discovery and diagnostic applications
Adv Drug Deliv Rev 57 (2005) 1087-1108

Licha, K., Riefke, B., Ntziachristos, V., Becker, A., Chance, B., Semmler, W.
Hydrophilic cyanine dyes as contrast agents for near-infrared tumor imaging:
Synthesis, photophysical properties and spectroscopic in vivo characterization
Photochem. Photobiol. 72 (2000) 392-398

Litzinger, D. C., Buiting, A. M., van Rooijen, N., Huang, L.
Effect of liposome size on the circulation time and intraorgan distribution of
amphipathic poly(ethylene glycol)-containing liposomes
Biochim Biophys Acta 1190 (1994) 99-107

Lopez-Davila, V., Seifalian, A. M., Loizidou, M.
Organic nanocarriers for cancer drug delivery
Curr Opin Pharmacol (2012)

Lu, Y., Low, P. S.
Folate-mediated delivery of macromolecular anticancer therapeutic agents
Adv Drug Deliv Rev 54 (2002) 675-693

Maeda, H., Wu, J., Sawa, T., Matsumura, Y., Hori, K.
Tumor vascular permeability and the epr effect in macromolecular therapeutics: A
review
J Control Release 65 (2000) 271-284

Mamot, C., Drummond, D. C., Noble, C. O., Kallab, V., Guo, Z., Hong, K., Kirpotin, D.
B., Park, J. W.
Epidermal growth factor receptor-targeted immunoliposomes significantly enhance
the efficacy of multiple anticancer drugs in vivo
Cancer Res 65 (2005) 11631-11638

Martinez-Poveda, B., Gomez, V., Alcaide-German, M., Perruca, S., Vazquez, S.,
Alba, L. E., Casanovas, O., Garcia-Bermejo, M. L., Peso, L., Jimenez, B.
Non-invasive monitoring of hypoxia-inducible factor activation by optical imaging
during antiangiogenic treatment in a xenograft model of ovarian carcinoma
Int. J. Oncol. 39 (2011) 543-552

Massoud, T. F., Gambhir, S. S.
Molecular imaging in living subjects: Seeing fundamental biological processes in a
new light
Genes Dev. 17 (2003) 545-580

Matsumura, Y., Maeda, H.
A new concept for macromolecular therapeutics in cancer chemotherapy: Mechanism
of tumoritropic accumulation of proteins and the antitumor agent smancs
Cancer Res 46 (1986) 6387-6392

McLean, J. W., Fox, E. A., Baluk, P., Bolton, P. B., Haskell, A., Pearlman, R., Thurston, G., Umemoto, E. Y., McDonald, D. M.
Organ-specific endothelial cell uptake of cationic liposome-DNA complexes in mice
Am. J. Physiol. 273 (1997) H387-404

Minchinton, A. I., Tannock, I. F.
Drug penetration in solid tumours
Nat Rev Cancer 6 (2006) 583-592

Mross, K., Niemann, B., Massing, U., Drevs, J., Unger, C., Bhamra, R., Swenson, C. E.
Pharmacokinetics of liposomal doxorubicin (tlc-d99; myocet) in patients with solid tumors: An open-label, single-dose study
Cancer Chemother Pharmacol 54 (2004) 514-524

Muggia, F. M.
Clinical efficacy and prospects for use of pegylated liposomal doxorubicin in the treatment of ovarian and breast cancers
Drugs 54 Suppl 4 (1997) 22-29

Mulder, W. J., Strijkers, G. J., van Tilborg, G. A., Griffioen, A. W., Nicolay, K.
Lipid-based nanoparticles for contrast-enhanced mri and molecular imaging
NMR Biomed. 19 (2006) 142-164

Nakayama, A., del Monte, F., Hajjar, R. J., Frangioni, J. V.
Functional near-infrared fluorescence imaging for cardiac surgery and targeted gene therapy
Mol Imaging 1 (2002) 365-377

Needham, D., Dewhirst, M. W.
The development and testing of a new temperature-sensitive drug delivery system for the treatment of solid tumors
Adv Drug Deliv Rev 53 (2001) 285-305

Ness, R. B., Cramer, D. W., Goodman, M. T., Kjaer, S. K., Mallin, K., Mosgaard, B. J., Purdie, D. M., Risch, H. A., Vergona, R., Wu, A. H.
Infertility, fertility drugs, and ovarian cancer: A pooled analysis of case-control studies
Am J Epidemiol 155 (2002) 217-224

Nie, S., Xing, Y., Kim, G. J., Simons, J. W.
Nanotechnology applications in cancer
Annu Rev Biomed Eng 9 (2007) 257-288

Noble, C. O., Kirpotin, D. B., Hayes, M. E., Mamot, C., Hong, K., Park, J. W., Benz, C. C., Marks, J. D., Drummond, D. C.
Development of ligand-targeted liposomes for cancer therapy
Expert Opin Ther Targets 8 (2004) 335-353

Ntziachristos, V., Bremer, C., Weissleder, R.
Fluorescence imaging with near-infrared light: New technological advances that enable in vivo molecular imaging
Eur Radiol 13 (2003) 195-208

Ntziachristos, V., Yodh, A. G., Schnall, M., Chance, B.
Concurrent mri and diffuse optical tomography of breast after indocyanine green enhancement
Proc Natl Acad Sci U S A 97 (2000) 2767-2772

Ogawa, M., Kosaka, N., Choyke, P. L., Kobayashi, H.
In vivo molecular imaging of cancer with a quenching near-infrared fluorescent probe using conjugates of monoclonal antibodies and indocyanine green
Cancer Res 69 (2009) 1268-1272

Ozols, R. F., Markman, M., Thigpen, J. T.
Icon3 and chemotherapy for ovarian cancer
Lancet 360 (2002) 2086-2087; author reply 2088

Papahadjopoulos, D., Allen, T. M., Gabizon, A., Mayhew, E., Matthay, K., Huang, S. K., Lee, K. D., Woodle, M. C., Lasic, D. D., Redemann, C., et al.
Sterically stabilized liposomes: Improvements in pharmacokinetics and antitumor therapeutic efficacy
Proc Natl Acad Sci U S A 88 (1991) 11460-11464

Park, J. W., Hong, K., Kirpotin, D. B., Colbern, G., Shalaby, R., Baselga, J., Shao, Y., Nielsen, U. B., Marks, J. D., Moore, D., Papahadjopoulos, D., Benz, C. C.
Anti-her2 immunoliposomes: Enhanced efficacy attributable to targeted delivery
Clin Cancer Res 8 (2002) 1172-1181

Ranson, M. R., Carmichael, J., O'Byrne, K., Stewart, S., Smith, D., Howell, A.
Treatment of advanced breast cancer with sterically stabilized liposomal doxorubicin: Results of a multicenter phase ii trial
J Clin Oncol 15 (1997) 3185-3191

Rice, B. W., Cable, M. D., Nelson, M. B.
In vivo imaging of light-emitting probes
J Biomed Opt 6 (2001) 432-440

Richardson, D. S., Johnson, S. A.
Anthracyclines in haematology: Preclinical studies, toxicity and delivery systems
Blood Rev 11 (1997) 201-223

Rubesova, E., Berger, F., Wendland, M. F., Hong, K., Stevens, K. J., Gooding, C. A., Lang, P.
Gd-labeled liposomes for monitoring liposome-encapsulated chemotherapy: Quantification of regional uptake in tumor and effect on drug delivery
Acad. Radiol. 9 Suppl 2 (2002) S525-527

Salvador-Morales, C., Gao, W., Ghatalia, P., Murshed, F., Aizu, W., Langer, R., Farokhzad, O. C.
Multifunctional nanoparticles for prostate cancer therapy
Expert Rev Anticancer Ther 9 (2009) 211-221

Sapra, P., Tyagi, P., Allen, T. M.
Ligand-targeted liposomes for cancer treatment
Curr Drug Deliv 2 (2005) 369-381

Schildkraut, J. M., Schwingl, P. J., Bastos, E., Evanoff, A., Hughes, C.
Epithelial ovarian cancer risk among women with polycystic ovary syndrome
Obstet Gynecol 88 (1996) 554-559

Scully, R. E.
Classification of human ovarian tumors
Environ Health Perspect 73 (1987) 15-25

Serwer, L. P., Noble, C. O., Michaud, K., Drummond, D. C., Kirpotin, D. B., Ozawa, T., Prados, M. D., Park, J. W., James, C. D.
Investigation of intravenous delivery of nanoliposomal topotecan for activity against orthotopic glioblastoma xenografts
Neuro Oncol 13 (2011) 1288-1295

Shaaban, A., Rezvani, M.
Ovarian cancer: Detection and radiologic staging
Clin. Obstet. Gynecol. 52 (2009) 73-93

Sharpe, M., Easthope, S. E., Keating, G. M., Lamb, H. M.
Polyethylene glycol-liposomal doxorubicin: A review of its use in the management of solid and haematological malignancies and aids-related kaposi's sarcoma
Drugs 62 (2002) 2089-2126

Skladanowski, A., Konopa, J.
Adriamycin and daunomycin induce programmed cell death (apoptosis) in tumour cells
Biochem Pharmacol 46 (1993) 375-382

Smith, R. E.
Risk for the development of treatment-related acute myelocytic leukemia and myelodysplastic syndrome among patients with breast cancer: Review of the literature and the national surgical adjuvant breast and bowel project experience
Clin Breast Cancer 4 (2003) 273-279

Straubinger, R. M., Arnold, R. D., Zhou, R., Mazurchuk, R., Slack, J. E.
Antivascular and antitumor activities of liposome-associated drugs
Anticancer Res 24 (2004) 397-404

Sutton, E. J., Boddington, S. E., Nedopil, A. J., Henning, T. D., Demos, S. G., Baehner, R., Sennino, B., Lu, Y., Daldrup-Link, H. E.
An optical imaging method to monitor stem cell migration in a model of immune-mediated arthritis
Opt Express 17 (2009) 24403-24413

Sutton, E. J., Henning, T. D., Pichler, B. J., Bremer, C., Daldrup-Link, H. E.
Cell tracking with optical imaging
Eur Radiol 18 (2008) 2021-2032

Sweeney, T. J., Mailander, V., Tucker, A. A., Olomu, A. B., Zhang, W., Cao, Y., Negrin, R. S., Contag, C. H.
Visualizing the kinetics of tumor-cell clearance in living animals
Proc Natl Acad Sci U S A 96 (1999) 12044-12049

Takemura, G., Fujiwara, H.
Doxorubicin-induced cardiomyopathy from the cardiotoxic mechanisms to management
Prog Cardiovasc Dis 49 (2007) 330-352

Tavri, S., Jha, P., Meier, R., Henning, T. D., Muller, T., Hostetter, D., Knopp, C., Johansson, M., Reinhart, V., Boddington, S., Sista, A., Wels, W. S., Daldrup-Link, H. E.
Optical imaging of cellular immunotherapy against prostate cancer
Mol Imaging 8 (2009) 15-26

Torchilin, V. P.
Recent advances with liposomes as pharmaceutical carriers
Nat Rev Drug Discov 4 (2005) 145-160

Torchilin, V. P.
Targeted pharmaceutical nanocarriers for cancer therapy and imaging
AAPS J 9 (2007) E128-147

Trimbos, J. B., Vergote, I., Bolis, G., Vermorken, J. B., Mangioni, C., Madronal, C., Franchi, M., Tateo, S., Zanetta, G., Scarfone, G., Giurgea, L., Timmers, P., Coens, C., Pecorelli, S.
Impact of adjuvant chemotherapy and surgical staging in early-stage ovarian carcinoma: European organisation for research and treatment of cancer-adjuvant chemotherapy in ovarian neoplasm trial
J Natl Cancer Inst 95 (2003) 113-125

Tung, C. H.
Fluorescent peptide probes for in vivo diagnostic imaging
Biopolymers 76 (2004) 391-403

Ulrich, A. S.
Biophysical aspects of using liposomes as delivery vehicles
Biosci. Rep. 22 (2002) 129-150

Unger, E., Needleman, P., Cullis, P., Tilcock, C.
Gadolinium-dtpa liposomes as a potential mri contrast agent. Work in progress
Invest Radiol 23 (1988) 928-932

Uziely, B., Jeffers, S., Isacson, R., Kutsch, K., Wei-Tsao, D., Yehoshua, Z., Libson, E., Muggia, F. M., Gabizon, A.
Liposomal doxorubicin: Antitumor activity and unique toxicities during two complementary phase i studies
J Clin Oncol 13 (1995) 1777-1785

Vermorken, J. B.
The role of anthracyclines in second-line therapy of ovarian cancer
Int J Gynecol Cancer 13 Suppl 2 (2003) 178-184

Viglianti, B. L., Ponce, A. M., Michelich, C. R., Yu, D., Abraham, S. A., Sanders, L., Yarmolenko, P. S., Schroeder, T., MacFall, J. R., Barboriak, D. P., Colvin, O. M., Bally, M. B., Dewhirst, M. W.
Chemodosimetry of in vivo tumor liposomal drug concentration using mri
Magn Reson Med 56 (2006) 1011-1018

Wallace, M. B., Kiesslich, R.
Advances in endoscopic imaging of colorectal neoplasia
Gastroenterology 138 (2010) 2140-2150

Waterhouse, D. N., Tardi, P. G., Mayer, L. D., Bally, M. B.
A comparison of liposomal formulations of doxorubicin with drug administered in free form: Changing toxicity profiles
Drug Saf 24 (2001) 903-920

Weiss, R. B.
The anthracyclines: Will we ever find a better doxorubicin?
Semin Oncol 19 (1992) 670-686

Weissig, V. V., Babich, J., Torchilin, V. V.
Long-circulating gadolinium-loaded liposomes: Potential use for magnetic resonance imaging of the blood pool
Colloids Surf B Biointerfaces 18 (2000) 293-299

Weissleder, R., Tung, C. H., Mahmood, U., Bogdanov, A., Jr.
In vivo imaging of tumors with protease-activated near-infrared fluorescent probes
Nat. Biotechnol. 17 (1999) 375-378

Whittemore, A. S., Harris, R., Itnyre, J.
Characteristics relating to ovarian cancer risk: Collaborative analysis of 12 us case-control studies. Iv. The pathogenesis of epithelial ovarian cancer. Collaborative ovarian cancer group
Am J Epidemiol 136 (1992) 1212-1220

Woodle, M. C., Lasic, D. D.
Sterically stabilized liposomes
Biochim Biophys Acta 1113 (1992) 171-199

Working, P. K., Dayan, A. D.
Pharmacological-toxicological expert report. Caelyx. (stealth liposomal doxorubicin hcl)
Hum Exp Toxicol 15 (1996) 751-785

Yatvin, M. B., Kreutz, W., Horwitz, B. A., Shinitzky, M.
Ph-sensitive liposomes: Possible clinical implications
Science 210 (1980) 1253-1255

Yu, M. K., Jeong, Y. Y., Park, J., Park, S., Kim, J. W., Min, J. J., Kim, K., Jon, S.
Drug-loaded superparamagnetic iron oxide nanoparticles for combined cancer imaging and therapy in vivo
Angew. Chem. Int. Ed. Engl. 47 (2008) 5362-5365

Zamboni, W. C., Gervais, A. C., Egorin, M. J., Schellens, J. H., Zuhowski, E. G., Pluim, D., Joseph, E., Hamburger, D. R., Working, P. K., Colbern, G., Tonda, M. E., Potter, D. M., Eiseman, J. L.
Systemic and tumor disposition of platinum after administration of cisplatin or stealth liposomal-cisplatin formulations (spi-077 and spi-077 b103) in a preclinical tumor model of melanoma
Cancer Chemother Pharmacol 53 (2004) 329-336

Zhang, X., Lin, Y., Gillies, R. J.
Tumor ph and its measurement
J. Nucl. Med. 51 (2010) 1167-1170

Zhigaltsev, I. V., Maurer, N., Akhong, Q. F., Leone, R., Leng, E., Wang, J., Semple, S. C., Cullis, P. R.
Liposome-encapsulated vincristine, vinblastine and vinorelbine: A comparative study of drug loading and retention
J Control Release 104 (2005) 103-111

8. List of Figures

9. List of Tables

10. List of Abbreviations

°C	degree Celsius
99mTc	Technetium 99m
Abs	Absorption
ACSR	AIDS and Cancer Specimen Resource
ADS	American Dye Society
AIDS	Acquired Immune Deficiency Syndrome
ALT	Alanine Transaminase
AML	Acute Myeloic Leukemia
AST	Aspartate Transaminase
ATP	Adenosine Triphosphate
AUC	Area Under the Curve
Bkg	Background
BRCA	BReast CAncer gene
c	Concentration (L)
CA-125	Cancer-Antigen 125
CCD	Charged Coupled Device
Chol	Cholesterol
CNP	Chitosan-based nanoparticle
CPT-11	Irinotecan
CT	Computed Tomography
Cy5.5	Cyanine dye 5.5
DAPI	4',6-diamidino-2-phenylindole
DCE-MRI	Dynamic Contrast Enhanced-MRI
ddH$_2$O	double distilled water
DiD	NIR Cyanine dye
DNA	Desoxyribonucleic acid
DOX	Doxorubicin
DsRed	Red Fluorescent Protein
e.g.	example given
Em	Emission
EphA2	ephrin type-A receptor 2

EPR	enhanced permeability and retention
Ex	Excitation
Fab	Fragment of Antibody
FAD	Flavine Adenine Dinucleotide
FCS	Fetal Bovine Serum
FDA	Food and Drug Andministration
FDG	Fludeoxyglucose
FIGO	Fédération Internationale de Gynécologie et d' Obstétrique
FOV	Field of View
FSI	Fluorescent Signal Intensity
Gd	Gadolinium
Gd-DTPA	Gadopentetat-Dimeglumin
GFP	Green Fluorescent Protein
GI	Gastrintestinal
h	hour(s)
H&E	Hematoxylin & Eosin
HER2	human epidermal growth factor receptor 2
HIF	hypoxia inducable factor
hMSCc	human Mesenchymal Stem Cell
HRE	hypoxia response element
HSPC	hydrogenated soy phosphatidylcholine
i.e.	id est
i.v.	intravenous
IACUC	Institutional Animal Care and Use Committee
ICG	Indocyanine Green
IGROV-1	ovarian cancer cell line
IVIS	*In vivo* Imaging System
l	length (mm)
LED	Light Emitting Diode
Ls	Liposome(s)
M	Molarity (mol/L)
MDS	Myelodysplastic Syndrome
Mm	Molecular Mass (g/mol)
Mn^{2+}	Manganese

MnSO$_4$	Manganese sulfate
MPEG-DSPE	N-(carbonyl-methoxypolyethylene glycol 2000)-1,2-distearoyl-sn-glycero3- phosphoethanolamine sodium salt
MRI	Magnetic Resonance Imaging
NADH	Nicotinamide Adenine Dinucleotide
NIR	Near-Infrared
nm	Nanometer
OI	Optical Imaging
OVCAR-3	ovarian cancer cell line
PBS	Phosphate Buffered Saline
PEG	polyethylene glycol
pi	post-injection
PL	Phospholipid
PPE	palmar-plantar erythrodysesthesia
RCF	Relative Centrifugal Force
RES	Reticuloendothelial System
RGD	Arginylglycylaspartic acid
RNA	Ribonucleic acid
ROIs	Region(s) of Interest
RPMI	Roswell Park Memorial Institute cell culture medium
s.c.	subcutaneous
SCC7	colon tumor susceptibility 7
scFv	single chain fragment variable
SDM	Standard Deviation of the Mean
siRNA	small interfering Ribonucleic acid
TNM	Tumor Node Metastasis Classification of malignant tumors
USP	United States Pharmacopoeia
ε	Extinction coefficient

11. Acknowledgments